**CONTRIBUTIONS OF GENETICALLY DEFINED INTERNEURON SUBTYPES
TO CONTRAST CODING IN MOUSE PRIMARY VISUAL CORTEX**

by

Jillian L. King

Submitted in partial fulfilment of the requirements
for the degree of Doctor of Philosophy

at

Dalhousie University
Halifax, Nova Scotia
December 2019

DEDICATION

This PhD thesis is the end product of a long road in post secondary education at Dalhousie University, but my time in Halifax has not just developed my academic abilities, it has also shaped me as a person. During this period of growth, the only two constants have been my uncle Paddy and my aunt Sharon, the best aunt and uncle anyone could ever be lucky enough to have. I have made most of the mistakes that a student has the opportunity to, and thanks to the unwavering support of Paddy and Sharon I always landed on my feet, often more stable than I was pre-mistake. The last 2.5 years of my life have been particularly trying and they have truly stepped up to help me keep my head afloat, going so far as to moving to a space that facilitated by ability to get to the lab and letting me live with them. I cannot express how much they have helped me, and I know I will never be able to even begin to repay them. Paddy and Sharon, I love you. This thesis became a reality because of you.

TABLE OF CONTENTS

LIST OF TABLES

LIST OF FIGURES

ABSTRACT

In the past decade the mouse primary visual cortex (V1) has become a popular brain region for investigating how neural circuits process information, largely because of the genetic tools available in this animal model. One of the most revolutionary genetic tools developed has been optogenetics, which refers to genetically-inserted light-sensitive proteins that are targeted to specific cell types. The ability to selectively activate individual cell types in specific brain regions provides scientists with a level of temporal and spatial resolution not previously available. This thesis contains two projects that take advantage of optogenetics to study an inhibitory circuit involved in visual processing in mouse V1. This inhibitory circuit is primarily composed of three interneuron (IN) subtypes: parvalbumin-expressing (PV+), somatostatin-expressing (Sst+) and vasoactive intestinal peptide -expressing (VIP+) INs. We individually activated these IN subtypes to investigate how they contribute to contrast coding. The first project examined how INs affect Pyramidal (Pyr) cell responses to varying levels of contrast, and our findings suggest that IN functionality is dependent on the state of the Pyr cell's local network. The second study examined whether individually activating INs affects how Pyr cells adapt to contrast, and our findings indicate that adaptation magnitude depends more on the overall activity level of V1 than which IN subtype is activated, although VIP+ INs appear to have a novel modulatory role. Overall, the findings from this thesis suggest that INs dynamically modulate contrast responses in mouse V1 as opposed to each subtype having an individual role as was previously thought.

LIST OF ABBREVIATIONS USED

AUC Area Under the Curve

c_{50} Contrast that Elicits Half the Maximum Response

cpd   Cycles per Degree

CRF Contrast Response Function

Hz   Hertz

IN   Interneuron

ISI   Interstimulus Interval

LGN   Lateral Geniculate Nucleus

PV+   Parvalbumin Expressing

Pyr   Pyramidal

RF   Receptive Field

RGC   Retinal Ganglion Cell

R_{Max} Maximum Response to Contrast

R_{Min} Minimum Response to Contrast

SF   Spatial Frequency

SS_{Res} Sum of Square Residuals

Sst+   Somatostatin Expressing

TF   Temporal Frequency

TTL Triggered Transistor-Transistor Logic

VIP+ Vasoactive Intestinal Peptide Expressing

V1   Primary Visual Cortex

ACKNOWLEDGEMENTS

CHAPTER 1: INTRODUCTION

1.1 GENERAL INTRODUCTION

We heavily rely on vision during our daily lives, and humans perceive most of their surroundings utilizing vision. As such, a primary goal within visual neuroscience is to determine how our visual systems process, interpret and integrate incoming information, which allow us to execute behaviors that are appropriate for a given environment. One of the most commonly studied parts of the mammalian visual system is the primary visual cortex (V1), the first cortical region that processes vision, and it has become one of the best understood areas in the cerebral cortex. However, even though V1 has been intensely investigated it is still not fully understood how it processes and transmits visual information. The two projects within this thesis were designed to add to our knowledge of V1 function by investigating how a local V1 circuit modulates visual input. This introduction chapter will outline the visual system using the classical non-human primate model, then draw comparisons to the highly utilized mouse model, and conclude with descriptions of the circuit that is subject and the two projects that were executed to probe its function within V1.

1.2 INTRODUCTION TO THE GENICULO-STRIATE PATHWAY OF PRIMATE MODELS OF VISION

This section briefly summarizes the anatomy and physiology of the geniculo-striate pathway, but more detailed reviews are available (e.g. Callaway, 2005; Prasad and Galetta, 2011)

1.2.1 <u>PRIMATE ANATOMY</u>

Primates have two forward facing eyes. The eye is a sphere-shaped organ filled with a gelatinous substance called the vitreous humor, allowing the eye to maintain its shape. At the front of the eye is the pupil, a hole that allows light to enter. Light that enters via the pupil is focused to the back of the eye by three primary components: (1) the cornea, a clear surface in front of the pupil that protects the eye; (2) the iris, a muscle that controls the diameter of the pupil; and (3) the crystalline lens, which is adjustable and lies

behind the pupil. The thickness of the lens is adjusted depending on the distance of the object being fixated and focuses light onto the retina where it forms a retinal image. All other eye anatomy is supportive of this optical function, which is referred to as accommodation. For review see Snell and Lemp, 1998.

Once light has reached the back of the eye it is processed by the retina, a thin layer of tissue organized into six layers that is a part of the central nervous system (Hildebrand and Fielder, 2011). The retina contains three types of light sensitive cells: rods, cones and melanopsin retinal ganglion cells. Overall, there are more rods than cones in the retina, but at the center of the primate retina is an area known as the fovea that has a peak density of ~210,000 cones/mm^2 (Packer et al., 1989). Rods and cones have different functions: cones are responsible for high spatial resolution and colour vision, whereas rods are fundamental for vision in dim light (Wikler and Rakic, 1990). Once light information has been transduced by rods and cones, it is further processed by bipolar, amacrine and horizontal cells and then exits the back of the eye through the axons of retinal ganglion cells that combine to form the optic nerve (for a more complete review, see Demb and Singer, 2015).

After light information has been processed by the retina and exits via the optic nerve, it is transmitted to the lateral geniculate nucleus (LGN) of the thalamus. The LGN is like a relay station, and its primary role is to regulate and organize information flow between the retina and V1 (Irvin et al., 1993; Wimbauer et al., 1997). The LGN receives feedforward input from the retina (e.g. Blitz and Regehr, 2005) feedback input from V1 (e.g. Ichida and Casagrande, 2002), and makes recurrent connections with other cells in the LGN (Bickford et al., 2008). It also provides feedforward and feedback output, with connections going back to the retina and forward to V1 and other cortical regions (for a thorough review on LGN circuitry, see Ghodrati et al., 2017). Primate LGN is divided into six layers, layer 1 being the most ventral and layer 6 the most dorsal (Walls, 1953). Contralateral retinal projections go to LGN layers 1, 4 and 6, and ipsilateral retinal projections go to layers 2, 3 and 5. In addition to layers being organized by ocular input, they are also organized based on cell size: layers 1 and 2 are composed of larger cells and are known as the magnocellular layers, whereas layers 3-6 are composed of smaller cells and known as the parvocellular layers (Jones, 1964). There are also thin koniocellular

layers between each LGN layer that consist of very small cells that receive input from the same eye as the layer below them (Hendry and Reid, 2000). The LGN is retinotopically organized, which refers to the mapping of visual information from the retina to neurons in the brain. Retinotopy provides organized 2D representations of the visual image in the thalamus, achieved by adjacent RGCs projecting to adjacent neurons in the LGN (Connolly and Van Essen, 1984).

The LGN sends feedforward projections to the primary visual cortex (V1), maintaining retinotopy (Tootell et al., 1988). V1 is located in the occipital lobe and is the first cortical region in the geniculo-striate pathway. The major role of V1 is to process incoming visual information and relay it to higher order visual areas. It is divided into six layers: I, II/III, VI/V and VI, where layer I is superficial. Layer IV, which receives most of the input from the LGN, is further subdivided into sub-laminae IVA, IVB, IVCα and IVCβ, which are collectively known as the granular layers (Callaway, 1998). Layer IVCα is the primary input layer for magno-cells of the LGN, layer IVCβ is the input layer for parvo-cells (Livingstone and Hubel, 1988). Layers V/VI provide output to subcortical feedback loops, whereas layer II/III is the primary output layer from V1 to other cortical regions (for review see Callaway, 2005), forming distal connections via long pyramidal cell axons; many of these axons terminate in extrastriate brain regions.

Extrastriate regions refer to any cortical areas that process visual information outside of V1 (Allman and Kaas, 1971). All extrastriate regions have a map of visual space and depend mostly on V1 for activation, and in primate it is estimated that there are roughly 30 of these extrastriate areas involved in processing vision (for review see Maunsell and Newsome, 1987). Based on cortical organization, connections and neural response properties, it has been established that there are two separate feedforward pathways from V1 to extrastriate areas: the dorsal and ventral streams, also referred to as the how and what processing streams, respectively. The dorsal stream is responsible for vision used for taking action, such as picking up an object, and feeds into the parietal lobe (Milner and Goodale, 1995). The ventral stream processes form vision for object recognition and terminates in the temporal lobe. Combined, these pathways allow us to perform visually guided actions and perceive objects in our surroundings (Maunsell and Newsome, 1987).

There are also many feedback connections to V1 from extrastriate areas (Perkel et al., 1986; Rockland and Van Hosen, 1994; Shipp and Zeki, 1989; Ungerleider and Desimone, 1986), and some of these connections even extend to subcortical regions (Fries, 1984; Gutierrez and Cusick, 1997). The plethora of connections within the geniculostriate pathway are still being unwound, and scientists are far from being able to describe its full complexity.

1.2.2 PRIMATE VISUAL PHYSIOLOGY

1.2.2.1 *Retina and LGN*

The first step in converting visual input into neural signals is phototransduction, which is performed by photoreceptors (for review see Yau, 1994). Photoreceptors then send this information to bipolar and horizontal cells, and bipolar and amacrine cells then connect to RGCs (for a more thorough review, see (Demb and Singer, 2015). A crucial feature of retinal neurons is that they respond to input from a particular region of visual space, which is known as a receptive field (RF; Kuffler, 1953). A key stimulus property that retinal neurons respond to is contrast.

Contrast is defined by the difference in luminance over space, and is often described using Michaelson contrast which binds contrast values between 0 (a uniform field of grey) and 1. A black and white checkerboard is an example of an object with high contrast because there is the maximum difference in luminance between adjacent squares on the board. Retinal contrast detection is achieved by what are known as center-surround RFs. Center-surround RFs have a circular center that is surrounded by an annulus, and they are distinguishable because they elicit opposite cellular responses to light. In the retina, center-surround RFs were first characterized by Kuffler (1953) in the cat, and he observed that there are two kinds: ON-center and OFF-center (Figure 1A-B). This RF organization results in neurons having both ON- and OFF-responses, which occur in ON- and OFF-regions of RFs, respectively. ON-responses are when a cell fires in response to a light increment, whereas OFF-responses are when a cell responds to a light decrement.

Spatial information from center-surround RFs in the retina are conserved by center-surround RFs in the LGN (Jacobs and Yolton, 1970).

1.2.2.2 *V1 Receptive Field Properties*
1.2.2.2.1 Orientation Selectivity

Neurons in V1 also respond to increments and decrements of light, but their RFs are more complicated than those found in the retina and LGN. V1 neurons are categorized as simple and complex cells (Dean and Tolhurst, 1983). Simple cells have RFs that are similar to retinal center-surround RFs in that there are clear demarcations between ON- and OFF- regions (Figure 1C). However, they are elongated as opposed to circular (DeAngelis et al., 1993). Complex cells also have elongated, oriented but they do not have clear demarcations of ON- and OFF-regions (Figure 1D; Dean and Tolhurst, 1983).

Orientation selectivity arises in V1 because LGN neurons are only weakly tuned for orientation (Xu et al., 2002). Within primate V1 50-80% of neurons are orientation selective (Zeki, 1983). A neuron is considered more orientation selective if it shows a strong preference for a specifically oriented stimulus; orientation selectivity can be quantified by a neuron's response to differently oriented lines or patterns to produce an orientation tuning curve. Hubel and Wiesel (1962) proposed that orientation selective cells in V1 are generated by simple cells summing input from LGN neurons with adjacent RFs to form elongated ON and OFF subregions within its RF that are most responsive to specifically oriented stimuli. Neurons within V1 are organized based on their orientation selectivity into functional columns known as iso-orientation domains that have a pinwheel center (Figure 2A; Bartfeld and Grinvald, 1992). Neurons in iso-orientation domains all have similar orientation preferences and are more narrowly tuned, whereas cells in pinwheel centers receive input from surrounding iso-orientation domains and therefore have broader, less specific tuning curves (Nauhaus et al., 2008). Figure 2 shows two orientation tuning curves - the neuron that generated the tuning curve in Figure 2B is an example of a well-tuned neuron, whereas the neuron that generated the tuning curve in Figure 2C is an example of a neuron that is more broadly tuned to orientation.
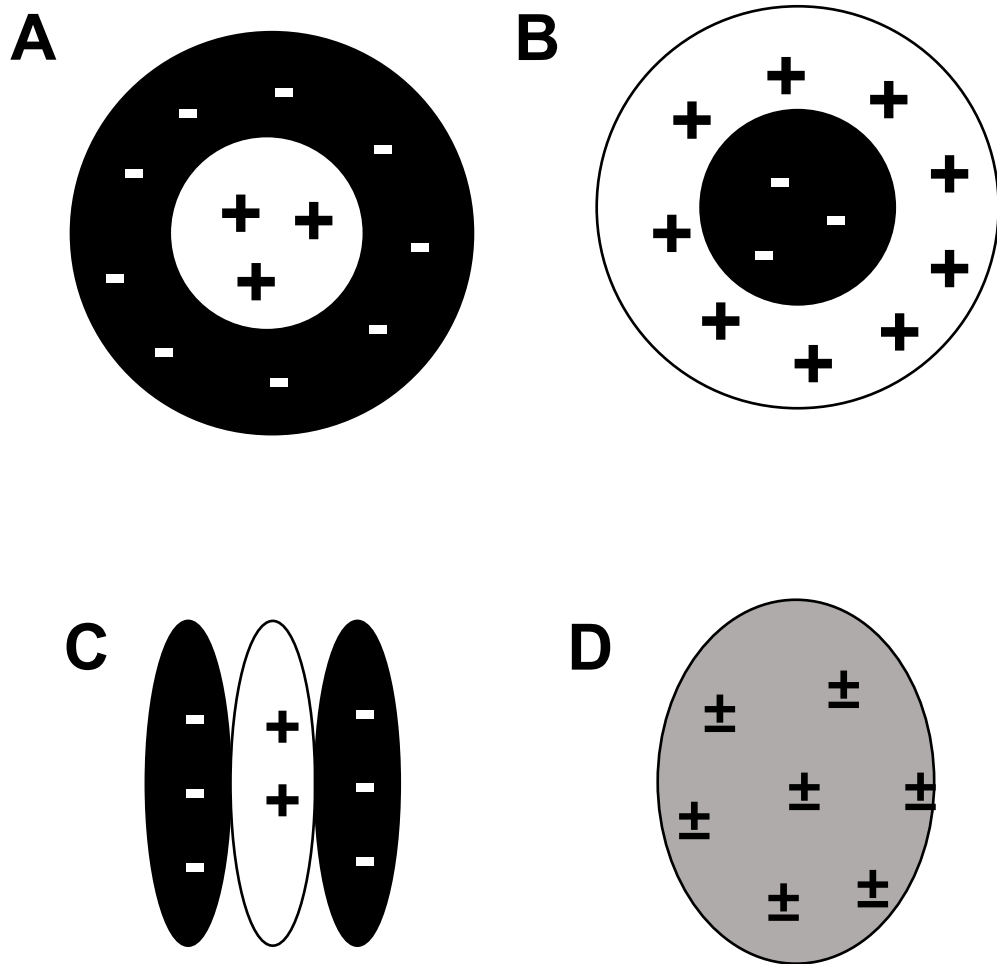
Figure 1: (A) A diagram depicting an ON-center RF and an (B) OFF-center RF. The black sections with minus signs represent a region that responds to decrements in luminance (OFF-response), whereas the white section with plus signs represents a region that responses to increases in luminance (ON-region). (C) A diagram outlining the organization of the RF of a simple cell in V1. The RF has elongated ON- and OFF-subregions which results in orientation preference, and it is clearly divided into ON- and OFF- response regions. (D) A diagram depicting a complex cell's RF.
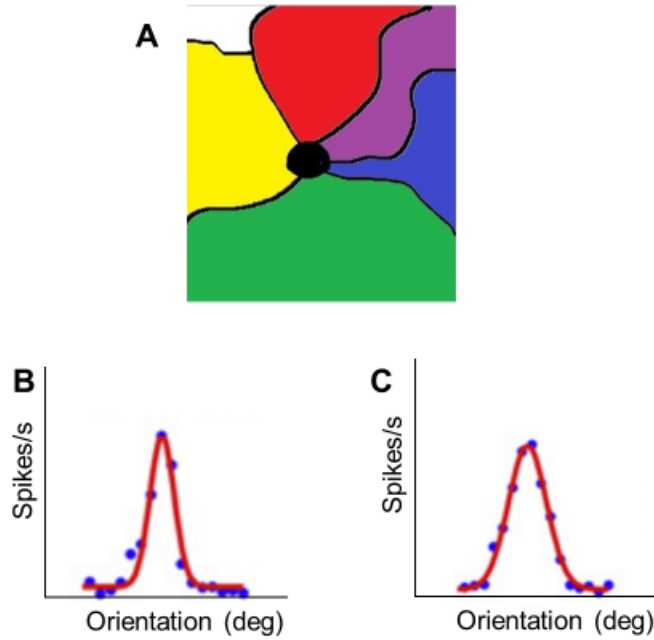
Figure 2: (A) A depiction of cortical iso-orientation domains and pinwheel centers. Solid colours indicate cortical columns where cells have similar orientation preference, and the black region in the middle is a pinwheel center, where neurons have broader tuning. (B) An orientation tuning curve from a neuron is highly selective to orientation. The orientation of the stimulus is on the x-axis, and the neuron's response in spikes/s is on the y-axis. (C) An orientation tuning curve from a neuron that is not as selective to orientation. Format is the same as in (A). Modified from Nauhaus et al., 2008.

1.2.2.2.2   Contrast Sensitivity

Neurons in primate V1 are also sensitive to varying levels of contrast, which is inherited from center-surround RFs antecedent to V1. Two types of gratings are commonly utilized by visual neuroscientists. Contrast gratings are composed of alternating light and dark bars, and are distinguished by their luminance profile. Square-wave contrast gratings have sharp edges between light and dark bars (Figure 3A). For sine-wave gratings, the luminance profile changes in a sinusoidal fashion across space (Figure 3B). Stationary sine-wave contrast gratings are defined by three parameters: (1) Contrast, (2) Orientation, and (3) Spatial Frequency, which is the number of cycles of the waveform per unit of distance (cycles/degree, cpd). Drifting sine-wave gratings, which are used in the current projects, have an additional fourth parameter: Temporal Frequency, which is time it takes to drift one complete cycle over a point in space in Hertz (Hz, cycles/second).

When plotted, the responses of a neuron to different levels of contrast form a neural contrast response function (CRF). CRFs have levels of contrast presented on the x-axis, and the neuron's response, in spikes per second, on the y-axis, and are often sigmoid-shaped (Figure 4). As can be seen in the CRF in Figure 4, neurons respond the most to high contrast, and the least to low contrast. Neurons in primate V1 are most sensitive to contrasts within a 3-30 % range, with contrasts above 30% achieving a plateaued response (Albrecht and Hamilton, 1982).

On a behavioural level, researchers quantify perception using psychophysics. Psychophysics refers to a group of experimental methods that examine the relationship between physical stimuli and a subject's perception of those stimuli. To measure contrast perception, researchers determine what is known as a contrast detection threshold, which is the lowest contrast that is reliably visible to a subject.

Figure 3: Square vs. Sine-wave contrast gratings. (A) An example of high contrast square-wave grating. (B) An example of a mid-level contrast sine-wave grating.
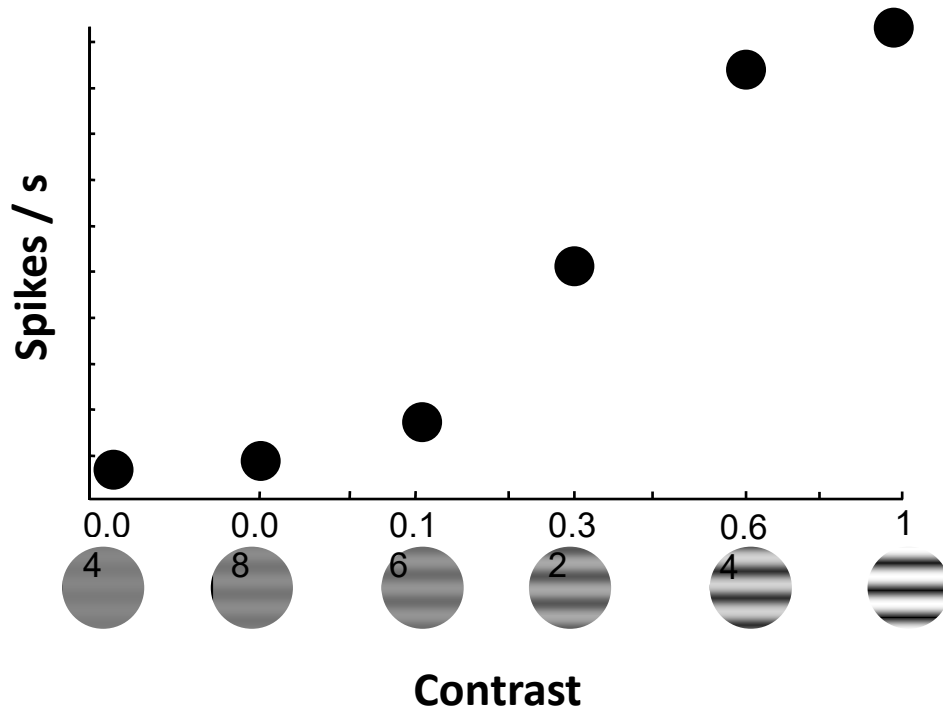
Figure 4: A characteristic neural contrast response function. Contrast of the stimulus is on the x-axis, and the neuron's response is on the y-axis. The response often takes the shape of a sigmoid function, with firing rate increasing with increasing contrast and the neuron responding most dynamically to mid-level contrasts.

1.2.2.2.3 Contrast Adaptation

Perceptual and neural adaptation is studied with the goal of better understanding how the brain modulates its responses to incoming sensory information. It allows us to investigate the immediate effects that perceptual stimuli have on sensory processing, which in turn allows us to also study how different brain regions process sensory information. Understanding how the brain changes its activity in response to perceptual stimuli is important because it is likely related to how we adjust our behaviour in response to our surroundings. Studies probing the underlying mechanisms behind sensory adaptation also provide insight into general plasticity questions because adaptation is a type of short-term neural plasticity. For a more thorough review on the benefits of studying neural adaptation, see Kohn (2007).

Perception of a visual stimulus, as well as the neural activity that encodes it, is affected by stimuli seen in the recent past. The after-effects produce following prolonged viewing of a single stimulus are called visual adaptation (for review, see Kohn, 2007). There are numerous types of visual stimuli that the primate visual system can adapt to, including, but not limited to, oriented stimuli (Coltheart, 1971), colored stimuli (Engel and Furmanski, 2001), and contrast gratings (Blakemore and Campbell, 1969; Sclar et al., 1989). Prolonged presentation of a contrast grating induces contrast adaptation, which is the type of adaptation that we investigate.

At the perceptual level, contrast adaptation causes a change in a subject's contrast detection threshold. This was first described by Blakemore and Campbell (1969) who reported that human participants experienced a five-fold increase in their contrast detection threshold after presentation of an adapt grating. Using EEG caps they also measured a significant decrease in brain activity in the occipital lobe, linking neural activity and visual adaptation.

Cellularly, CRFs are used to quantify how contrast adaptation affects neural responsivity. After presentation of a high contrast grating, CRFs shift rightwards and downwards (Sclar et al., 1989), indicating a change in their dynamic response range, decreased sensitivity to contrast, and an overall decrease in firing rate. The magnitude of CRF changes are often determined by the contrast level of the adapt grating; higher

contrasts elicit larger responses which cause a larger shift in the adapted CRF, suggesting that contrast adaptation is a firing rate dependent phenomenon (Sanchez-Vives et al., 2000). However, other influences beyond the recorded neuron must be involved because it has been shown that the similarity of adapting and test gratings also affects the magnitude of CRF shifts (Sclar et al., 1989).

1.2.2.2.4   Other V1 Receptive Field Properties

There are numerous other stimuli properties for which neurons in primate V1 show specificity for, including spatial and temporal frequencies, and color, and the cortex is functionally organized based on many of these properties (for review see Lund et al., 2003). As one moves along the visual pathway, beyond V1, RFs become more sensitive and specific (e.g. dorsal and ventral streams discussed in section 1.2.1).

1.3 MOUSE IN VISUAL NEUROSCIENCE

Mice are commonly used in neuroscience because of the genetic tools that are readily available in this species. This section outlines what a transgenic mouse is, covers similarities and differences between mouse and primate vision, and then goes into more detail on the specific type of transgenic mouse we utilized.

1.3.1   <u>TRANSGENIC MICE</u>

The prefix trans- refers to changing form or position (Merriam-Webster Dictionary, 2019), and therefore a transgene is a gene that is taken from one species' genome and inserted into another's. The first living transgenic organism was developed in 1974 (*E. Coli,* Cohen et al., 1973) and the first transgenic mouse was developed in 1981 (Costantini and Lacy, 1981). Since then transgenic mice have become one of the most important tools in the life sciences, particularly in health and neuroscience research.

Transgenic mice have revolutionized how scientists can investigate the brain. By being able to insert genes into the mouse genome at specific locations, we can target many aspects of neuronal structure and function. A common goal in neuroscience is to

determine neuronal roles, and the most accurate way to target a specific cell type is to genetically target a protein that is unique to that cell. By targeting these unique proteins, we can target neural populations at an unprecedented resolution. The attractiveness of the transgenic mouse is compounded by the fact that of all research mammals, mice are the cheapest, easiest to house, have the shortest gestation period, and additionally, they share roughly 95% of genes with humans (Bryda, 2013; International Human Genome Sequencing Consortium, 2001; Mouse Genome Sequencing Consortium, 2002). Combined, these reasons motivated vision neuroscientists to investigate whether the mouse could be an appropriate model for vision research.

1.3.2 COMPARING MOUSE ANATOMY TO PRIMATE ANATOMY

1.3.2.1 *Eye and Retina Comparison*

Perhaps the most obvious difference between the mouse and more traditional animal model visual systems is that mice have laterally positioned eyes, giving them a binocular visual field of only ~40° (Scholl et al., 2013). The retina has overall fewer cells than primate retina, but they do have the same proportion of rods:cones (Packer et al., 1989; Wikler and Rakic, 1990). However, instead of a fovea mice have an area centralis with a peak density of 12,4000 cones/mm2 (Jeon et al., 1998). Mice have similar retinal cell types, although they have only two cone pigments (Applebury et al., 2000) compared to primates' three pigments (Marks et al., 1964). They also have similar cell layers and retinal circuits (Jeon et al., 1998), however a majority of the output from mouse RGCs goes to the superior colliculus (Ellis et al., 2016)

1.3.2.2 *V1 Comparison*

Mouse V1 is also the first cortical region to process visual information, and it conserves retinotopy from the LGN (Wagor et al., 1980). Its six layers are organized identically to that in primate V1, with the same layers providing the major inputs and outputs. The largest difference between mouse and primate V1 are that overall mouse V1 is smaller, comprising ~200,000 neurons compared to the macaques' 300 million (Baker, 2013). Also, mouse LGN is not layered, therefore input to V1 is not dependent on LGN

layering (however, mouse LGN does have ipsilateral and contralateral areas (Howarth et al., 2014)).

1.3.2.3 *Extrastriate comparison*

Mice have eleven extrastriate areas that receive input from V1 (Garrett et al., 2014), which is about a third of the number of regions in the primate cortex. Overall, primates utilize roughly 50% of their cortex to process visual information whereas mice only use about 10% (Baker, 2013). There is evidence that there are ventral and dorsal processing streams in the mouse visual system (Wang et al., 2012), but this is an area of research that requires more work (Marshel et al., 2011).

1.3.3   COMPARING MOUSE PHYSIOLOGY TO PRIMATE PHYSIOLOGY

As with anatomy, mouse V1 physiology shares many properties with primate V1 physiology: they have simple and complex cells (Niell and Stryker, 2008), their neurons are tuned for spatial and temporal frequencies (Niel and Stryker, 2008; Gao et al., 2010), are sensitive to color (Jacobs et al., 2007), and their V1 is retinotopically organized (Wagor et al., 1980). However, neurons in mouse V1 are overall much less selective to visual stimulus properties. This section will outline similarities and differences between orientation selectivity, contrast selectivity and contrast adaptation in mouse V1 because these properties are the most pertinent to the current studies.

1.3.3.1 *Orientation Selectivity*

Neurons in mouse V1 are much less selective to orientation (Niel and Stryker, 2008; Gao et al., 2010; King and Crowder, 2018). It has been estimated that roughly 30% of mouse V1 neurons are tuned to orientation, determined by quantifying how tuned orientation curves are from mouse V1 Pyr cells (Gao et al., 2010; King and Crowder 2018). A small proportion of mouse V1 neurons give robust responses to their preferred orientations and fire near the spontaneous rate to orthogonal orientations, like V1 neurons recorded in cat or macaques (Nauhaus et al., 2008). However, the orientation tuning functions of many mouse V1 neurons have a non-selective component (a robust response

to any orientation) that appears to be added on to a weak orientation-tuned response (Niel and Stryker, 2008; King and Crowder 2018). One potential reason that there are fewer highly orientation tuned tuned mouse V1 neurons is that they still contain symmetrical dendritic fields but are organized in what is described as a "salt and pepper" distribution (Van Hooser et al., 2005; Ohki et al., 2005) as compared to orientation columns. This dendritic tree shape and salt and pepper distribution means that most, if not all, cells in mouse V1 receive input from cells that respond to many different orientations, similar to cells in pinwheel centers as in higher order mammals (Nahaus et al., 2008). However, Ringach et al. (2016) provided evidence that mouse V1 does possess a "degraded version" of orientation topography suggesting that perhaps there are similar mechanisms between species.

1.3.3.2 *Contrast*

Neurons in mouse V1 also proportionally respond to contrast (Niell and Stryker, 2008; Gao et al., 2010), and their responses can be quantified using a CRF. However, they are less sensitive to low levels of contrast, with the steepest regions of their CRFs appearing to be between ~25-65% (King et al., 2015, 2016; LeDue et al., 2013).

1.3.3.3 *Contrast Adaptation*

Neurons in mouse V1 also change their responses after a prolonged presentation of a high contrast grating. Numerous studies have demonstrated that CRFs from mouse V1 neurons exhibit the same rightward and downward shifts after adaptation as measured in primate V1 (e.g. Stroud et al., 2012; LeDue et al., 2013). Additionally, we have also shown that contrast adaptation is firing rate dependent, but the magnitude of adaptation is affected by the similarity of the adapting and test gratings which suggests the involvement of processes beyond firing rate (King et al., 2015).

1.4 <u>OPTOGENETICS</u>

1.4.1   *What is Optogenetics?*

In 1979 Francis Crick acknowledged that one of the greatest obstacles for neuroscientists was the inability to control single cell types in an intact circuit and suggested that light sensitive cells may be the answer (Deisseroth, 2010). Unbeknownst to Crick, microbiologists were already studying a family of proteins that did respond to light; these light-sensitive proteins are coded by group of genes referred to as "opsins", and directly control the flow of electric charge across cell membranes in response to light. However, it took until the summer of 2005 for these light-sensitive proteins to be utilized by neuroscientists. Two graduate students in Dr. Karl Diesseroth's lab at Stanford University used transgenic methodology to insert an opsin into mouse hippocampal tissue (Boyden et al., 2005), to develop a new technology they coined optogenetics - the ability to control mammalian cellular activity with light.

Since the development of optogenetics, scientists have engineered countless optogenetic proteins, including ion channels, ion pumps and G-protein coupled receptors (for review see Guru et al., 2015). All these genetically engineered cells work in a similar fashion: when light of the correct wavelength is shone on cells expressing optogenetic proteins, the protein undergoes a conformational change that opens the ion channel or activates the ion pump, causing either depolarization or hyperpolarization. An example of a common excitatory opsin is Channelrhosopsin2 (ChR2), which is a light-gated nonspecific cation channel (this opsin is the one first expressed by Boyden et al. (2005) and remains among the most commonly used today). Halorhodopsins are an example of inhibitory opsins, and one such halorhodopsin, NpHR, pumps chloride into the cell upon light stimulation causing hyperpolarization.

Optogenetics has revolutionized neuroscience because of its temporal and spatial resolution. Before this technology, we primarily relied on drugs and electric stimulation to study neural circuits. However, drugs are often not sufficiently specific to affect only one cell type, and they lack temporal precision; electrical stimulation, although more temporally accurate than drug application, has even less cellular specificity. Optogenetics

addressed both of these issues with its cell-type specific genetic targeting and millisecond response time to light presentation.

1.4.2   Cre-Lox Optogenetic Mice

There are two common methods used to create an optogenetic mouse: injecting a viral vector with the opsin transgene into the brain region of interest, or as the foregoing research does, breeding transgenic animals. Transgenic animals used for breeding optogenetic mice are now commercially available and employ what is known as the Cre-Lox system. The Cre- refers to Cre recombinase, which is an enzyme that catalyzes the recombination of two loxP sites that flank a STOP-cassette; this STOP-cassette prevents the expression of a given protein. The Cre-lox system can be utilized to inactivate genes of interest; this is done by flanking the promoter of the gene of interest with loxP, which then causes the gene of interest to not be expressed when bred with a Cre mouse. It can also be used to activate genes of interest, as our lab did to express optogenetic proteins. To breed a mouse to express optogenetic proteins (e.g. ChR2) two kinds of transgenic animals are required: one mouse that has a gene for ChR2 preceded by a floxed STOP cassette, and a second mouse that expresses Cre recombinase in the specific cell type targeted for optogenetic proteins. When these mice are bred, the gene for ChR2 will be present in all cells, but the loxP sites will only be recombined in the cell-type that expresses Cre recombinase (for a thorough explanation, see Jackson Laboratories description of their Ai32 mouse). By using this method, any lab has access to transgenic animals with the most up-to-date technology available. In recent years, many have utilized optogenetic mice to study how inhibitory interneurons (INs) mediate cortical activity.

1.5 INTERNEURONS IN MOUSE V1
1.5.1   <u>INTERNEURON POPULATIONS</u>

There are two broad categories of neurons that make up the cortex: pyramidal cells (Pyr cells) and GABAergic INs. Pyr cells are excitatory neurons that transmit information

both within and between brain regions. Inhibition from INs shape and modulate Pyr cell activity to alter response specificity, local and brain-wide network dynamics, and they control the excitation-inhibition balance that is crucial for healthy brain function (for review see Tremblay et al., 2016). INs represent ~10-15% of cortical neurons in rodents (Meyer et al., 2011), and until recently it was nearly impossible to study them due to this overall low proportion of such cells. The advances in genetics (described in section 1.3.1) have allowed scientists to accurately target and manipulate these neurons, and over the past 20 years understanding of INs has grown tremendously.

A single type of IN is not sufficient to manage all of the roles necessary to control Pyr cell function, therefore a broad array of these "short axon" neurons have evolved in the cortex (DeFelipe and Jones, 1988). INs subtypes differ in their gross anatomy (Kawaguchi and Kubota, 1997; Kubota, 2014; Markram et al., 2004; Somogyi et al., 1998), connectivity (Beierlein et al., 2003; Gibson et al., 1999; Jiang et al., 2015; Pfeffer et al., 2013), and physiology (Kawaguchi and Kubota, 1997; Markram et al., 2004). These differences affect how INs respond to input and how they impact their postsynaptic targets, allowing them to modulate Pyr cell activity in all the ways necessary to maintain proper brain function.

Even though we know the overall proportion of INs in the cortex, there is still not a firm grasp on how many subtypes of INs exist (Group, 2008; Tremblay et al., 2016). Originally it was thought that INs in the cortex could be classified based on anatomical features, but which features are important for classification is still a matter of debate (for review, see Tremblay et al., 2016). After a meeting in 2008, the Petilla Interneuron Nomenclature Group agreed that molecular markers are a better feature to use as the first level of IN classification in rodent cortex and this has since been standard practice (Group, 2008). However, there is still concern that other IN subtypes exist (Tremblay et al., 2016), and it is understood that there are potentially other IN subpopulations that have yet to be defined but may play crucial roles in modulating Pyr cell activity. Perhaps a more accurate categorization will arise from the discovery of new markers that allow us to further divide current IN subtypes.

Nevertheless, by using molecular markers to characterize IN subtypes, there is strong evidence that cortical INs within mouse V1 can be divided into three groups: Parvalbumin expressing (PV+, ~40%), Somatostatin expressing (Sst+, ~30%) and 5HT3aR expressing (~30%) INs (Lee et al., 2010; Tasic, Bosiljka Menon, Vilas Nguyen, Thuc Nghi Kim, Tae Kyung Jarsky, Tim Yao, Zizhen Levi, Boaz Gray, Lucas T Sorensen, Staci A Dolbeare, Tim Bertagnolli, Darren Goldy et al., 2016; Zeisel et al., 2015). These three groups do not overlap and have different functional properties, suggesting that they play different roles in modulating brain activity. 5HT3aR expressing INs can further divided into two clear groups: those that express Vasoactive Intestinal Peptide (VIP) and those that do not; VIP+ INs make up 40% of this group (Lee et al., 2010). The studies in this thesis examine the roles of PV+, Sst+ and VIP+ INs in visual processing.

1.5.1.1 *PV+ INs*

PV+ INs correlate well with two anatomical groups: fast-spiking basket cells, and chandelier cells. Basket cells make up a majority of PV+ INs, and are named as such because they form perisomatic "basket" terminals on the cell bodies and proximal dendrites of Pyr cells and INs (Fino and Yuste, 2011; Karnani et al., 2014; Packer and Yuste, 2011; Pfeffer et al., 2013). Chandelier neurons (also known as axo-axonic neurons) compose the smaller portion of the population and make connections to the axon initial segments of Pyr cells. PV+ INs cell bodies are mostly found in layers IV through VIb (Pfeffer et al., 2013; Xu et al., 2010), and receive strong feedforward excitatory input from pyramidal cells in their layer as well as from recurrent connections in layers 2/3 (Adesnik et al., 2012; Dantzker and Callaway, 2000; Xu and Callaway, 2009). Their activity is proportional to the activity of the local network, suggesting that PV+ INs keep activity levels under control by becoming progressively more active with their local network (Adesnik et al., 2012). Both types of PV+ cells hyperpolarize target neurons on their somata, where action potentials are produced, thereby having a large effect on postsynaptic output (Fishell and Rudy, 2011).

1.5.1.2 *Sst+ INs*

There are two major anatomical classes of INs that express Sst: Martinotti and non-Martinotti cells. The cell bodies for both Sst+ IN subtypes are predominantly in layer 5 (Xu et al., 2010). Martinotti cells have a dense network of axons in layer 1 where they specifically target the tuft dendrites of Pyr cells; non-Martinotti have local axonal networks and target both Pyr cells and other INs (Chiu et al., 2013; Kawaguchi and Kubota, 1997; Wang et al., 2004), providing constant inhibition to the cells around them. The distinction between these two classes is important because of where they primarily target postsynaptic cells, although both cell types are dendritic-targeting (Kawaguchi and Kubota 1996; Wang et al 2004). For the purposes of this thesis we are not separating these two classes and will collectively refer to them as Sst+ INs.

1.5.1.3 *VIP+ INs*

VIP+ IN make up only 1-2% of cortical neurons (Jackson et al., 2016; Pfeffer et al., 2013) and their cell bodies are found primarily near the cortical surface in layers 1 and 2/3 (Xu et al., 2010). A majority of VIP+ INs have vertically oriented dendrites (Bayraktar et al., 2000; Pronneke et al., 2015) which allows them to receive input from multiple superficial layers. They also have vertical axons that travel downward, reaching L4-L5/6, in addition to their local axonal arbors (Bayraktar et al., 2000; Porter et al., 1998; Pronneke et al., 2015). Because VIP+ IN activity is positively correlated with activity levels of proximal excitatory cells (Karnani et al., 2016), it is hypothesized that these INs play a large role in propagating excitatory information within a neural circuit.

1.5.2   <u>INTERNEURON CIRCUIT</u>

Recent work utilizing anatomical, electrophysiological and optogenetic methodologies has been able to piece together some of the underlying connections and functions of different IN subtypes. The following two sections will briefly cover the current model of cortical IN circuitry, and then discuss what is known about IN roles in visual processing.

1.5.2.1 *Circuit described in in vitro*

The blueprint of cortical IN connectivity was initially outlined in mouse V1 by Massimo Scanziani's lab (Pfeffer et al., 2013), and this blueprint has been widely utilized as the model circuit in visual neuroscience studies investigating INs. Pfeffer's (2013) circuit was expanded on by Karnani et al. (2016), and Figure 5 shows the proposed IN circuit by combining findings from these two important studies: PV+ INs inhibit all cell types including themselves; Sst+ INs inhibit all cell types except for themselves; and VIP+ INs primarily inhibit Sst+ INs, but can also mildly inhibit or excite other VIP+ INs (Pfeffer et al., 2013; Karnani et al., 2016). PV+ and Sst+ INs inhibit Pyr cells, but VIP+ INs cause disinhibition because they preferentially inhibit Sst+ INs.
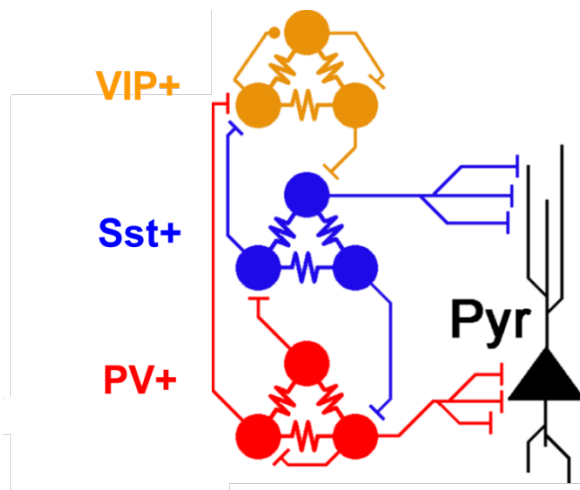
Figure 5: A current model of IN circuitry from in vitro findings (Pfeffer et al., 2013; Karnani et al., 2016). PV+ INs are shown in red, Sst+ shown in cyan and VIP+ in purple, and a Pyr cell is shown in black. Inhibitory GABAergic synapses are represented with capped lines, cholingeric synapses are capped with dots, and electrical gap junctions are depicted between INs as jagged lines. Figure modified from Ingram et al. (2019).

In addition to inhibitory chemical synapses, INs in the same subgroup within 100-150um of one another have a high probability of connecting via excitatory gap junctions (Amitai et al., 2002; Galarreta and Hestrin, 1999; Karnani et al., 2016). Modeling and paired recording in slice has determined that these electrical connections cause IN networks to fire synchronously, however the gap junctions mediating these connections and their functions are still not understood.

1.5.2.2 *Roles for individual interneuron types*

In addition to untangling portions of IN circuitry, researchers have also begun to determine how INs are involved in sensory processing. As described above, one of the primary roles of INs is to control overall activity levels to ensure that the cortex does not become overactive, which is also referred to as gain control. Optogenetics has revolutionized how to investigate gain control within the cortex by allowing scientists to selectively activate one IN subtype and determine how it affects visually driven activity. Gain control is often described as arithmetic operations: changes in neural responses can be either divisive or subtractive (divisive: Carandini and Heeger, 2012; subtractive: Lee et al., 2012; Wilson et al., 2012). The terms divisive and subtractive refer to changes in relation to control responses – if a neuron is experiencing divisive changes, its responses are being scaled proportionally meaning that larger changes occur at higher spike rates. In contrast, if a neuron is undergoing subtractive changes, its responses are being shifted equally across all spike rate levels. Examples of gain control of are shown in Figure 6 using a CRF; the curve that was divisively scaled shows a large change in spike rate at the highest contrast, whether it underwent facilitation or inhibition, and very little change at the lowest contrast (Figure 6A). The curve that was shifted subtractively shows consistent facilitation or inhibition at all contrast levels, with inhibition at low contrasts being rectified because a negative spike rate is not possible (Figure 6B). For the purposes of this thesis, the terms divisive scaling and subtractive shifting will be used for both facilitation and inhibition of responses.
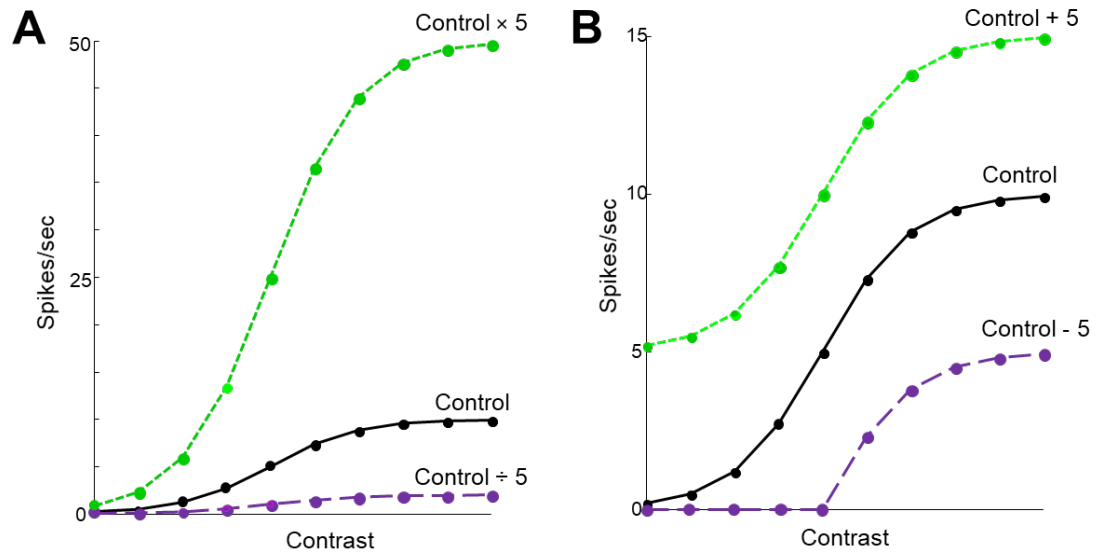
Figure 6: Examples of neural gain control on two identical CRFs with a maximum firing rate of 10 spikes/s. Control curves are black, responses that were facilitated are green, and inhibited responses are purple. The mathematical manipulation that was performed on control responses is labeled by each curve. (A) Examples of divisive scaling. (B) Examples of rectified subtractive shifts.

It was previously thought that PV+ INs caused divisive scaling and Sst+ INs caused subtractive shifts (Atallah et al., 2012; Wilson et al., 2012), but recent evidence suggests that this is more complicated than originally thought. Most studies investigating gain control in mouse V1 have examined the effects of optogenetically activating PV+ and Sst+ INs on orientation tuning curves (Atallah et al., 2012; El-Boustani and Sur, 2014; Ingram et al., 2019; Lee et al., 2012; Wilson et al., 2012), and most have found that activating PV+ INs scales response magnitude without narrowing tuning width by inducing divisive inhibition (Atallah et al., 2012; El-Boustani and Sur, 2014; Wilson et al., 2012; Ingram et al., 2019), whereas activating Sst+ INs narrows orientation selectivity by subtractively shifting neural responses so that responses to non-preferred orientations fall below the spiking threshold (Wilson et al., 2012). However, Lee et al. (2012) found that PV+ INs sharpened orientation tuning, whereas activating Sst+ INs did not. These varied findings led to three follow-up studies, and it was agreed that differing optogenetic photostimulation protocols between labs likely caused the differences in results (Atallah et al., 2014; El-Boustani et al., 2014; Lee et al., 2014). This suggests that the type of inhibition induced by an IN subtype depends on the state of the network. Indeed, a study by El-Boustani and Sur (2014) suggest that the type of inhibition caused by Sst+ INs is dynamic and depends on when they are activated; when Sst+ INs are activated after Pyr cells, they provide subtractive inhibition (Wilson et al., 2012; El-Boustani and Sur, 2014), but when Sst+ are activated simultaneously with Pyr cells they induce divisive inhibition (El-Boustani and Sur, 2014). This timing rule also appears to apply when multiple IN subtypes are activated in aggregate; when Ingram et al. (2019) simultaneously activated all INs coincident with visual stimulus onset, Pyr responses were divisively scaled.

The role of INs has also been examined in more specific visual processes, such as surround suppression and contrast detection. Adesnik et al. (2012) demonstrated that as a visual stimulus increases in size, Sst+ INs respond more robustly and recruit one another. Therefore, as the stimulus size increases, Sst+ INs increasingly inhibit Pyr cells, which causes the responses of Pyr cells to decrease as stimulus size increases. INs also play a role in mediating contrast detection. Using a contrast detection threshold task, Cone et al.

(2019) demonstrated that activating PV+ or Sst+ INs impaired contrast detection, whereas activating VIP+ INs caused an improvement.

Finally, IN activity in mouse V1 has been linked to locomotion. The relationship between locomotion and V1 activity has been intensely studied, and it has been repeatedly reported that mouse locomotion activates V1 pyramidal cells (Dadarlat and Stryker, 2017). Therefore, it is fitting that INs have been found to have a regulatory role in V1 during locomotion. Fu et al., (2014) demonstrated that VIP+ activity is correlated with locomotion, and that application of a nicotinic antagonist decorrelated activity. This suggests that VIP+ INs are being activated by the basal forebrain cholinergic system during locomotion. Because VIP+ INs selectively inhibit Sst+ INs they release nearby INs and Pyr cells from inhibition, suggesting that locomotion involves an orchestrated effort from the entire circuit.

Overall, these somewhat disparate findings suggest that IN subtypes may not have single individual roles, but instead their jobs within local networks may be dynamic with different behavior under the multitude of contexts experienced by an animal. Therefore, in order to completely untangle their circuits and functionality, researchers must investigate how INs impact neural responses under a multitude of paradigms and be careful not to over-extrapolate their findings.

1.6 CURRENT PROJECTS

1.6.1   <u>THE ROLE OF INERNEURONS IN CONTRAST RESPONSES</u>

1.6.1.1 *Previous work*

In section 1.5.2.2 the differences between divisive and subtractive inhibition were outlined, and it is clear that a particular IN subtype can induce different types of inhibition depending on the experimental conditions. As discussed, El-Boustani and Sur (2014) determined that these differences likely arose from network temporal dynamics, but Lee et al. (2014) emphasized that differences in photostimulation intensities can cause differing results within an IN subtype.

1.6.1.2 *Using contrast response functions to investigate unresolved circuit issues*

Based on discrepancies reported in previous work, we believe there are three strategies that can help disentangle the type of inhibition caused by each IN subtype: (1) examining varying photo-intensities, (2) varying the timing of normal feed-forward neural activation with visual stimulation and artificial optogenetic photostimulation, and (3) using a visual stimulus that ensures large modulation in the neural responses. We utilized two of these strategies in our first study by examining the effects of different levels of photostimulation intensity on V1 neurons' CRFs. Many of the studies examining divisive/subtractive inhibition in mouse V1 have utilized orientation tuning curves (e.g. Atallah et al., 2012; Ingram et al., 2019), but given past observations that the majority of neurons in mouse V1 are not strongly orientation tuned (e.g. Gao et al., 2010; Niell and Stryker, 2008; King and Crowder 2018), the pattern of optogenetically induced inhibition is challenging to discern within the limited visually evoked firing rates. Conversely, different levels of stimulus contrast evoke visual responses over the full dynamic range of firing rates for most V1 neurons (e.g. Stroud et al., 2012). We reasoned that measuring optogenetic modulation using CRFs instead of orientation tuning curves could reveal more subtle differences between divisive and subtractive inhibition because of the larger difference between the minimum and maximum neural responses. Additionally, the role of VIP+ INs in Pyr cell contrast responses has not been previously investigated.

1.6.2   THE ROLE OF INTERNEURONS IN CONTRAST ADAPTATION

1.6.2.1 *Previous work*

In 2016 we published a study that demonstrated that contrast adaptation is locally modulated via a firing rate dependent mechanism within mouse V1 (King et al., 2016; Appendix 1). By characterizing changes in V1 CRFs following optogenetically silencing V1 during the adaptation period, and measuring adaptation in mouse LGN, we found that 99% of the adaptation normally measured in V1 could be explained as divisive scaling of the adapted LGN input. However, because we were optogentically activating all IN subtypes, we were unable to determine how individual IN subtypes contributed.

1.6.2.2 *Role of INs in Contrast Adaptation*

Intuitively, the two primary IN candidates for modulating inherited adapted input to V1 are PV+ and Sst+ INs because they directly synapse onto Pyr cells. But, these two IN subtypes also interested us because they modulate Pyr cell activity differently based on both the type of inhibition they induce, and where they synapse on Pyr cells (PV+ INs: divisive scaling, somatic synapses; Sst+ INs: subtractive shifts, dendritic synapses). To investigate how these two subtypes contributed to the effects observed in King et al. (2016), and whether their differing network connections affect their contributions, we ran the identical adaptation and photostimulation protocol. However, instead of completely silencing V1 by strongly activating all IN subtypes, we only partially suppressed activity by activating PV+ or Sst+ INs individually. We felt it was important to partially suppress neural activity as opposed to silencing it because of the secondary effects of IN photoactivation. For example, the primary effect of activating Sst+ INs is inhibition of all other cell types (Pfeffer et al., 2013), whereas a secondary effect is a decrease in Sst+ IN activity because they receive less excitation from inhibited Pyr cells. We reasoned that in a normally functioning circuit activating a specific IN subtype will allow both primary and secondary effects (see example above), but if the circuit is pushed too far below its normal physiological levels (i.e. silenced), these secondary effects, which are crucial to determining the differences in modulatory roles between IN subtypes, may be absent or distorted. Additionally, if we were to totally suppress V1 activity during the adaptation period we would not be inducing divisive (PV+ activation, Atallah et al., 2012) or subtractive (Sst+ IN activation, Wilson et al., 2012) inhibition, but rather cause the spike rate to completely flatten.

We also optogenetically perturbed VIP+ INs. VIP+ INs are known to facilitate activity, so we hypothesized that their activation would cause increased adaptation based on our previous findings that contrast adaptation in mouse V1 is an activity driven phenomenon.

Overall, the work presented in this thesis aims to aid clarity to how INs impact Pyr cell responses. Chapter 3 examines how INs modulate Pyr cell responses when they

are simultaneously active, whereas Chapter 4 investigates how IN modulation impacts "future" Pyr cell responses by utilizing a contrast adaptation paradigm.

CHAPTER 2: MATERIALS AND METHODS

2.1 ANIMALS

All experimental procedures were performed in accordance with the guidelines of the Canadian Council on Animal Care and were approved by the Dalhousie University Committee on Laboratory Animals.

Experiments were performed on the offspring of three mouse Cre lines to drive expression of channelrhodopsin 2 (ChR2) in the IN of choice. We used the commercially available mice with the Cre-LOX system to achieve ChR2 expression (outlined in section 1.4.2). Our Cre and Ai32 mice were purchased from The Jackson Laboratory (Bar Harbor, ME, USA), and two F_1 generations were used for experiments. We bred these mice in-house and used the following mouse lines: Ai32 (Jax Stock #012569); Pvalb-IRES-Cre (Jax Stock #008069) for PV+ mice; Sst-IRES-Cre (Jax Stock #013044) for Sst+ mice; and Vip-IRES-Cre (Jax Stock #010908) for VIP+ mice. Mice had *ad libitum* access to rodent chow (Purina #5001) and tap water, and were housed in a colony room (22 °C ± 2 °C) on 12hr:12hr light:dark cycle.

Breeders were genotyped by The Jackson Laboratory Transgenic Genotyping service using standard polymerase chain reaction (PCR) on either tail snips or pieces of cortex, and results confirmed that we used proper breeders to generate our experimental animals.

2.2 PHYSIOLOGICAL PREPARATION

Animals were pre-medicated with an injection of chlorprothixene (5mg/kg, intraperitoneal injection; Sigma Aldrich) and then placed in a face mask and anaesthetized with isoflurane in oxygen for the remainder of the experiment (2.5% isoflurane during induction, 1.5% during surgery, and 0.5% during recording; Pharmaceutical Partners of Canada). The face mask occluded part of the central visual field (central 30-45 degrees azimuth and up to 10 degrees elevation), but still allowed for a clear view of the laterally placed computer monitor. Chlorprothixene injections were given every four hours to maintain a level of sedation that allowed us to record extracellular electrophysiological signals (i.e. neural spikes) at 0.5% isoflurane. Once the mouse was anesthetized their body temperature was maintained at 37.5 °C with a heating

pad, and optically neutral silicone oil (30,000 cSt, Sigma Aldrich) was applied roughly once/hour to protect the cornea. To prepare for electrophysiological recordings, the scalp was removed and a head post was attached to the skull using dental epoxy. Next, a small craniotomy (~1 mm^2) was made over V1 (0.8 mm medial and 2.3 mm lateral from lambda, Paxinos and Franklin, 2001). To prevent dehydration of the cortex, the craniotomy was surrounded by a wall of petroleum jelly and filled with physiological saline. We did not dilate the pupils to maintain a large depth of focus, and the eyes were not immobilized because eye movements under anesthesia have been demonstrated to be negligible in mice (Gao et al., 2010; Niell and Stryker, 2008; Wang and Burkhalter, 2007).

In-vivo extracellular recordings were made with either glass micropipettes (tip diameter of 2-5 µm and contained 2 M NaCl), or with tetrodes (Teflon coated NiCr wire, with gold electroplating on the tips to bring impedance to ~300kΩ). Signals were isolated, amplified, filtered, and acquired with a CED 1401 interface and Spike2 software (Cambridge Electronic Designs, Cambridge, UK) sampled at 40kHz. Online response curves were generated in Spike2 from triggered transistor-transistor logic (TTL) pulses from a window discriminator (Cornerstone by Dagan). Template-based offline spike sorting was also done with Spike2. We applied a high-pass filter (270 Hz) to each recording, and then utilized a principal components analysis and interspike interval histogram to check isolation of individual units. Data was exported to MATLAB (Mathworks, Natick, MA, USA) and neuronal responses were represented as spike density functions with 1kHz resolution, generated by convolving a delta function at each spike arrival time with a Gaussian window. Example spikes are shown in Figure 7.

2.3 LED PHOTOSTIMULATION

The tip of the fiberoptic cannula was positioned ~0.2-0.5mm above the surface of V1, and a 470nm fiber-coupled LED was used for optogenetic photostimulation (0.4mm diameter; 0.39 NA; Thor Labs). LED activation was coordinated with visual stimuli by the CED 1401. Neurons expressing ChR2 pass measurable photocurrent at a light intensity of ~0.02mW/mm^2, which saturates at ~1mW/mm^2 (Asrican et al., 2013). Our fiber power output of 0.089 - 1.16mW (median: 0.092mW) was estimated to yield 0.14 –

1.8mW/mm^2 (median: 0.15mW/mm^2) at 0.8mm cortical depth (Stujenske et al., 2015), which is sufficient light intensity to induce photocurrents in ChR2(H134R)-EYFP expressing INs even in layer 6. However, because photostimulation intensity was always strongest near the cortical surface it was important to consider the layer distribution of INS in V1. No GABAergic INs in layer 1 express PV, and few express Sst (~2%) or VIP (~5%). In layers 2/3 a similar proportion of INs express VIP (~20%) and PV (~20%), with fewer expressing Sst (8%). In deeper layers ~50% of INs express PV, 20-30% express Sst, and ~7% express VIP (Xu et al., 2010; Pfeffer et al., 2013). Our range of surface LED intensity was 0.002 – 0.39 mW/mm^2, which is consistent with previous work (Ingram et al., 2019).

2.4 VISUAL STIMULI

Stimuli were presented on a calibrated CRT monitor (LG Flatron 915 FT Plus 19" display, 100 Hz refresh, 1024 · 768 pixels, mean luminance = 30cd/m^2) at a viewing distance of 25-30 cm, and presented for eight repetitions. Visually responsive neurons were isolated using a flashing black and white stimulus and receptive fields (RF) were mapped by hand using an ophthalmoscope. Quantitative stimuli were programmed in MATLAB using the Psychophysics Toolbox extension (Brainard, 1997; Pelli, 1997). Orientation/direction tuning was tested with square-wave gratings drifting in 16 directions. Square wave gratings are composed of many spatial frequencies so this broadband stimulus was used to evoke responses from as broad a sample of neurons as possible. Preferred size was tested with sine-wave gratings in six different sized circular apertures drifting in the neuron's preferred direction. Preferred orientation and RF size were analyzed online to ensure neurons responded robustly to the experimental stimuli. All stimuli had a SF of 0.03 cpd, and a TF of 2 Hz. Sine-wave contrast is defined as:

$$Michelson\ contrast = \frac{Luminance_{max} - Luminance_{min}}{Luminance_{max} + Luminance_{min}} \tag{1}$$

Where Luminance$_{max}$ and Luminance$_{min}$ are the maximum and minimum luminance, respectively
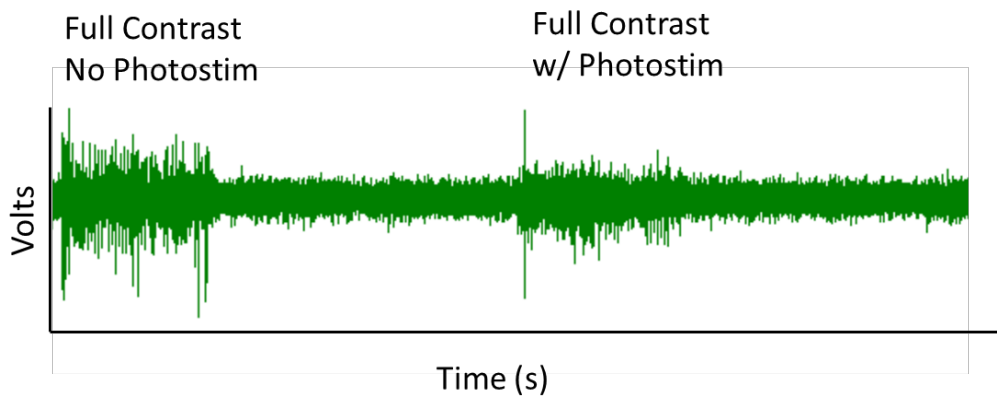
Figure 7: Examples of a raw extracellular recording for roughly 6s showing a Pyr cell's response to 1s of full contrast with and without LED photostimulation.

2.4.1 *Contrast Response Functions with LED Photostimulation*

Neural responses to contrast were measured using a fully randomized protocol where drifting sine wave gratings of five contrasts (0.06, 0.12, 0.16, 0.5 and 1) were presented for 1s each. A grey uniform field of the same of mean luminance was presented for 2s between grating presentations. Trials where LED photostimulation was paired with visual stimuli were shuffled randomly with non-photostimulated trials, generating two contrast response functions for each recording. A diagram describing this stimulus is shown in Figure 8A.

2.4.2 *Contrast Adaptation with LED Photostimulation*

Contrast adaptation was also measured using a fully randomized protocol, where drifting sine wave gratings of ten contrasts (0.04, 0.08, 0.12, 0.16, 0.24, 0.32, 0.48, 0.64, 0.82 and 1) were presented for 1s each. Trials when the neuron was adapted were preceded by an adapt grating of 0.5 contrast for 2s, and nonadapt trials were preceded by 2s of a grey of mean luminance. Trials with LED photostimulation were again interleaved with non-photostimulated trials, and photostimulation was applied during the adapt period at the LED intensity that caused ~40-60% suppression during the stimulus described in section 2.4.1. Between trials there was a 6s presentation of a grey of mean luminance. A diagram describing this stimulus is shown in Figure 8B. This adaptation protocol generated four contrast response functions: (1) Control Nonadapted; (2) Control Adapt; (3) Optogenetic photostimulation in the nonadapted condition (Opto Nonadapt); and (4) Optogenetic photostimulation in the adapted condition (Opto Adapt).
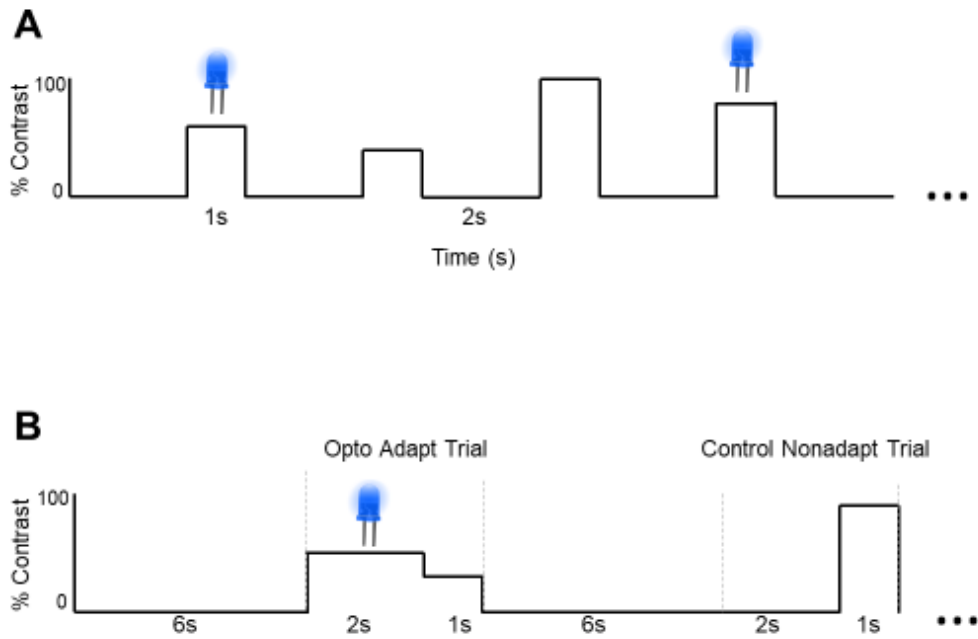
Figure 8. Visual stimuli and photostimulation protocols (A) Line plot depicting the timing and levels of contrast presented for the stimulus described in section 2.4.1. The length of the line along the x-axis represents how long that part of the stimulus was presented, and the length along the y-axis represents the level of contrast of that grating. Blue LEDs on top of contrast presentations represent LED stimulation. This stimulus had 1s presentation of a contrast grating with a 2s ISI, and 1s LED photostimulation occurred during the stimulus presentation for photostimulated (Opto) trials. Opto trials were interleaved with Control trials. (B) Line plot depicting the timing and levels of contrast presented for the stimulus described in section 2.4.2. Figure format is identical to A. This adaptation protocol had a 2s adapt period with a 1s test period and a 6s ISI, with Nonadapt trials having an 8s ISI. LED photostimulation was presented during the adapt period for Opto Adapt trials, and the last 2s of the 8s ISI for Nonadapt Opto trials. Control and Opto trials were interleaved.

2.5 DATA ANALYSIS

2.5.1 *Contrast Response Functions*

CRFs were fit to sigmoid curves using the least squares method (Albrecht and Hamilton, 1982):

$$R(c) = \frac{R_{max} \cdot c^n}{c^n + c_{50}{}^n} + R_{min} \tag{2}$$

where R(c) is the amplitude of the response at contrast c, R_{Min} is the response to the lowest contrast, n is the exponent that determines the steepness of the sigmoid curve, R_{max} is the maximum elevation in response above the R_{Min}, and c_{50} is the contrast that elicits half that of R_{max}. Area under the curve (AUC) was calculated for CRFs by converting Michaelson contrast to percent contrast, then to log contrast, and then trapezoidal integration was performed on the log-CRF (Wissing and Kohn, 2012; King et al., 2015). In previous studies we have not always reported changes in CRFs AUC, but because it is a more holistic measure of CRF change we reasoned it would be ideal for these studies due to the small shifts caused by our optogenetic stimulation, particularly for our adaptation investigation. All parameters are shown on an example CRF in Figure 9. We used r^2 to quantify the goodness of fit of the sigmoid curve to our raw data points. We did not subtract spontaneous activity from Pyr cell responses to contrast.

2.5.2 *Calculating Photostimulation Effects*

All spike rates were normalized to the control response at 100% contrast. To quantify changes in Pyr cell CRF parameters, we calculated percent change for AUC, R_{max}, and R_{Min}:

$$\% \ change = \frac{(P_{Opto} - P_{Ctrl})}{(P_{Opto} + P_{Ctrl})} \times 100 \tag{3}$$
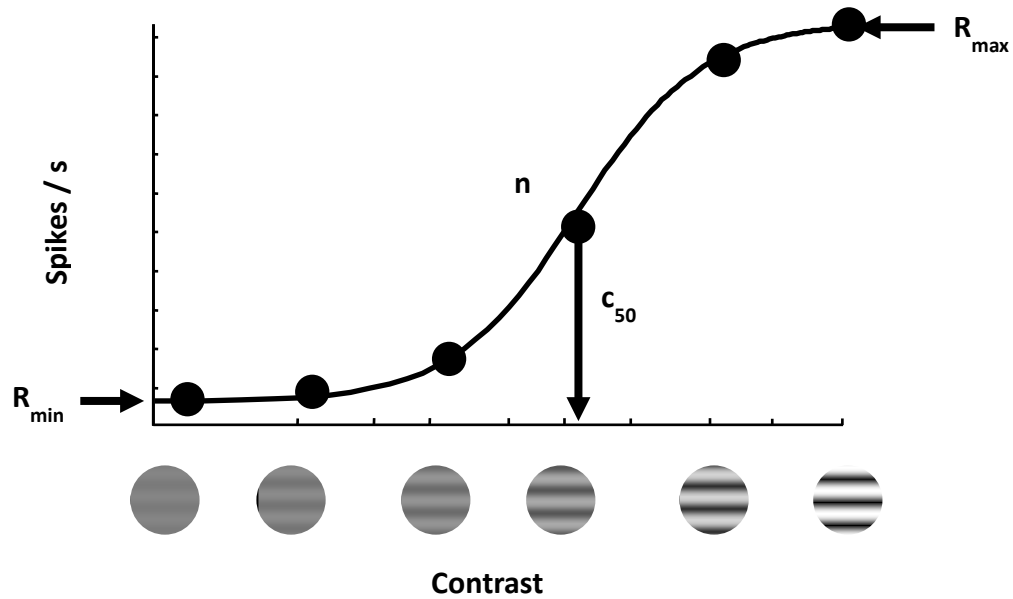
Figure 9: A labeled neural contrast response function. Naka-Rushton functions are used to fit a sigmoid-shape curve to neural responses to contrast, allowing extraction of four parameters for quantitative analysis: (1) R_{Max} and (2) R_{Min}, the maximum and minimum responses, respectively, (3) c_{50}, the contrast that elicits half of the maximum response, and (4) n, which is the exponent that determines the slope.

where P_{Opto} is the value of the parameter from the optogenetic photostimulation (Opto) curve and P_{Ctrl} is the value from the control curve. Changes in c_{50} were calculated by simply subtracting the control value from the Opto value:

$$\Delta c_{50} = Opto(c_{50}) - Ctrl(c_{50}) \tag{4}$$

And finally, changes in slope (n) were quantified as a difference over sum of log slope:

$$\Delta \log n = \frac{Opto \log n - Ctrl \log n}{Opto \log n + Ctrl \log n} \tag{5}$$

2.5.3 *Modelling Contrast Response Function Shifts*

      We modelled the effect of photostimulation on CRFs as either divisive or subtractive changes for cells in Chapter 3 (described in section 1.5.2.2). We fit each neuron's response during photostimulation to a sigmoid curve where the parameters described for equation 2 were held constant using the estimated parameters from control responses, but with one added term to model either divisively scale:

$$R_{Opto} = \frac{R_{Ctrl}}{g} \tag{6}$$

where R_{Opto} is the Opto response, R_{Ctrl} is the Ctrl response, g is the scaling term, or subtractively shift with rectification:

$$R_{Opto} = R_{Ctrl} - h, R_{Opto} \geq 1 \tag{7}$$

where R_{Opto} is the Opto response, R_{Ctrl} is the Ctrl response and h is the shifting term. Each model was fit using the least squares method. We then measured the residuals for both models (i.e. the difference between the models and the opto data points) and calculated an F-statistic to determine which model fit the data better:

$$F \, stat = \frac{SSRes \, Div}{SSRes \, Sub} \tag{8}$$

where SS_{Res} Div is the sum of square residuals for the divisive model and SS_{Res} Sub is the sum of square residuals for the subtractive model. This F-stat calculation is appropriate for comparing models with the same number of free parameters (Motulsky and Ransnas, 1987).

2.5.4 *Exclusion Criteria*

Cells were excluded from population analyses if they met one or more of the following criteria:

1. If the minimum response of the control condition was >25% of its maximum.
2. If the r^2 of the sigmoid fit to neural responses was <0.85 for any condition.
3. If the neuron was excited by photostimulation in PV*Cre or Sst*Cre animals.

These criteria were used to ensure that when comparing parameters between control and optogenetic conditions we were not including neurons that had inconsistent or noisy visual responses, and to make sure we did not include any PV+ or Sst+ INs in our sample. We also used neural latency to distinguish between recordings of VIP+ INs that were directly optogenetically activated by photostimulation and putative Pyr cells that were modulated by VIP+ IN activation (see below).

2.5.4.1 *Neural Latency*

A universal concern when combining optogenetics and electrophysiology is whether the neuron being recorded from is the intended cell type. Some groups aim to photostimulate and record from the same neural population, whereas others, such as our lab, want to stimulate one cell type and determine how it affects the responses of a different cell type. Techniques such as two-photon microscopy can aid with targeting the desired neural population, but one can also take advantage of cellular biophysics to exclude unintended cell types from their population sample.

As described in section 1.4.1, optogenetic proteins respond to LED photostimulation within milliseconds, and for the current work, ChR2 activated one of three inhibitory IN subtypes. Therefore, we reasoned that if we were unintentionally recording from a VIP+ IN we would see essentially an immediate increase in activity

from the neuron after the LED was illuminated. Whereas, if we were recording from a neuron innervated by an optogenetically activated VIP+ IN, its activity would change following the latency of a chemical synapse. To objectively measure whether photostimulation was directly activating the neuron we were recording from, we calculated the standard deviation of the difference between the Opto and Ctrl responses, and then multiplied it by 1.96:

$$Photostimulation\ Threshold = [1.96 \times \sigma(R_{Opto} - R_{Ctrl})] \qquad (9)$$

where σ is the standard deviation, R_{Opto} is the Opto Response and R_{Ctrl} is the Control Response. For our stimulus paradigm in section 2.4.1, we measured neural latency to the 100% contrast test gratings, and for the paradigm in section 2.4.2 we measured the neural latency in our Opto Adapt condition which was presented at 50% contrast. We reasoned that if the Ctrl and Opto responses differed more than this, we could reliably assert that photostimulation was affecting the cell's firing at $\sim p < 0.05$ with a two-tailed test.

Figure 10A-D shows traces from four cells that depict this analysis. Figure 10A-C are traces from Pyr cells recorded from during activation of PV+, Sst+ or VIP+ INs, respectively. Figure 10D shows a trace from a PV+ IN recorded from in a PV-Cre*Ai32 mouse. For all top traces, Control responses are shown in black and the Opto responses are shown as red, blue or orange for PV+, Sst+ or VIP+ IN photostimulation, respectively. The bottom pink traces represent the difference between the Opto and Control responses, with the dashed horizontal line indicating the threshold and the blue asterisks indicating the time it took for firing rates of the Opto and Ctrl signals to significantly diverge for that cell. When comparing the location of the blue asterisks it can be seen that at least a small portion of the pink trace is visible for the cells in Figure 10A-C, indicating that the photostimulation did not immediately affect the neurons' response but rather the INs that were activated took $\sim$100ms to alter the response of the Pyr cell being recorded from. In comparison, the cell in Figure 10D was immediately affected by photostimulation, indicated by the blue asterisks being located so close to 0ms that no pink trace is visible. Indeed, when this photostimulation latency was plotted for all of our cells, divided into which type of mouse they came from, it is obvious that

the cells we determined were PV+ INs had a much lower photostimulation latency than our Pyr cell populations (Figure 10E). To highlight this difference, Figure 10F presents the same data as Figure 10E, but with a zoomed-in y-axis.

We aimed to use this latency analysis as an exclusion criterion to distinguish between photoactivated VIP+ INs and disinhibited Pyr cells. We reasoned that if a cell was directly activated the effect of photostimulation would be evident within less than 10msec.

2.5.5 *Statistical Analyses*

We used parametric analyses (specific tests noted) and applied the Benjamini-Hochberg procedure for controlling false discovery rate (x total comparisons). Adjusted p-values are reported (Benjamini and Hochberg, 1995). Table 1 shows the number of comparisons for each cell type in both studies.

Table 1A: The number of statistical comparisons in Chapter 3

Cell Type	Number of Tests
PV+	6
Sst+	6
VIP+	14
Cell Type Comparisons	5

Table 1B: The number of statistical comparisons in Chapter 4

Cell Type	Number of Tests
PV+	20
Sst+	20
VIP+	30
Cell Type Comparisons	8
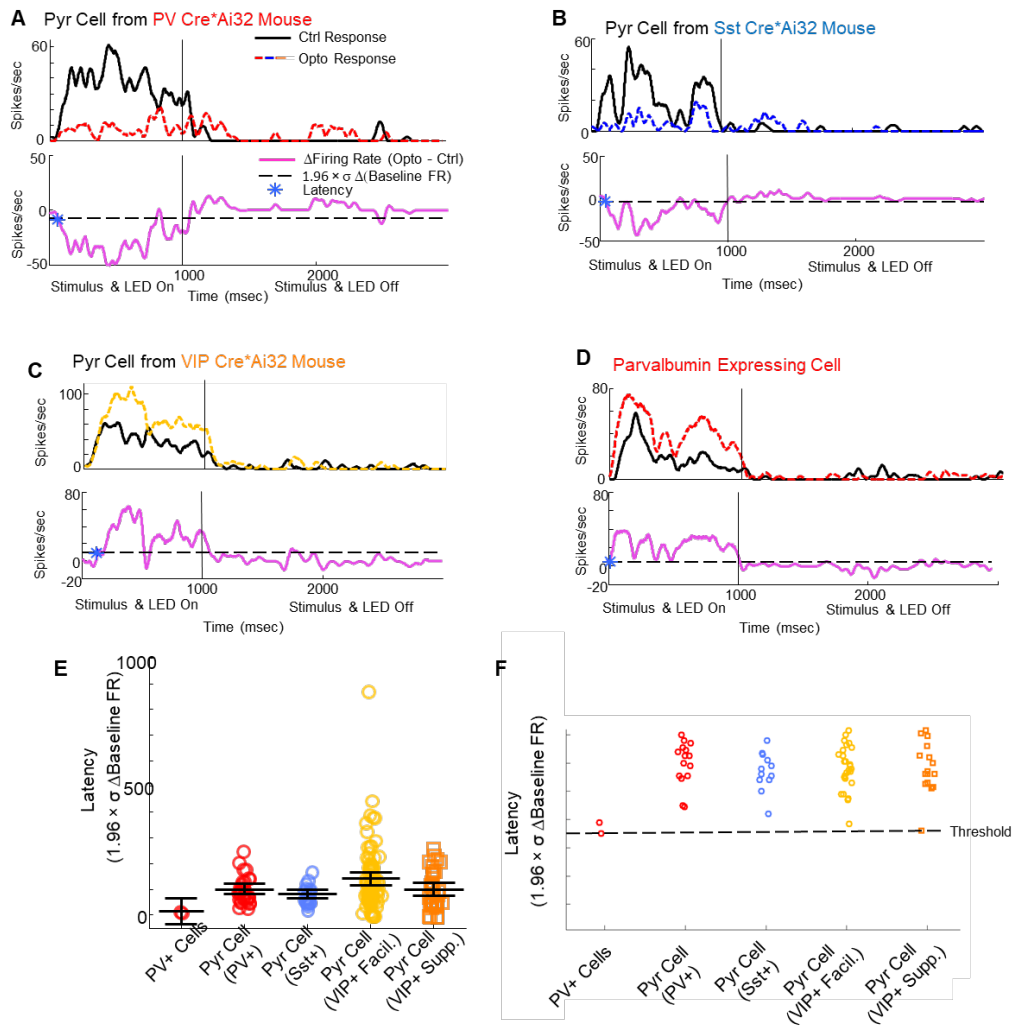
Figure 10. Latency of photostimulation effects (A-D) Top panels show spike density functions from four example cells with control traces shown in black and IN photostimulated curves shown as colored dashed lines (labeled above trace). The pink traces in the bottom panels show the difference between the Control and Opto traces in the top panels, with the 95% threshold for that cell shown as a horizontal dashed line, and the latency of photostimulation indicated with a blue asterisk. X-axis is time in msec and y-axis is spikes/s for all traces. (E) Scatter column showing the latency for all cells in each cell group. Inset demonstrates that no disinhibited Pyr cells had a latency faster than 10ms. (F) A zoomed-in view of E, showing that none of our facilitated Pyr cells via VIP+ IN activation were activated within 10ms.

CHAPTER 3: THE EFFECT OF INTERNEURON ACTIVATION ON CRFs

3.1 HIGHLIGHTS

- Currently, there is not a consensus in visual neuroscience regarding how different IN subtypes modulate Pyr cell responses to visual stimuli because findings have been varied.

- It is thought that some of the discrepancies between studies arise from different experimental paradigms.

- To attempt and parse how differing photostimulation paradigms may have affected previous findings, we used varying LED intensities to selectively activate the three major IN subpopulations while measuring Pyr cell responses to varying levels of contrast.

- Activating PV+, Sst+ or VIP+ INs does modulate Pyr cell responses to contrast.

- Changes to CRF parameters correlate with the amount of photostimulation-induced activity change for all three IN subtypes.

- PV+ IN activation divisively inhibited Pyr cell responses to contrast.

- Sst+ IN activation was just as likely to divisively or subtractively inhibit Pyr cell responses.

- VIP+ IN effects on Pyr cell responses were examined, and we were surprised to observe both facilitation and suppression. Pyr cell responses were not consistently divisively or subtractively altered as a result of VIP+ activation.

We investigated the roles of three different INs in modulating Pyr CRFs. Previous studies have addressed this issue and have produced conflicting results (Wilson et al., 2012; Lee et al., 2012; Atallah et al., 2012), and it is thought that these differences are potentially caused by differences in methodology (Lee et al., 2014; El-Boustani et al., 2014). Therefore, we have added to this body of research by (1) quantifying the effects of multiple LED intensity within the same cell, (2) measuring optogenetic modulation of CRFs to help determine how INs alter both strong and weak Pyr cell responses, and (3) examining how the three primary IN subtypes modulate Pyr cell responses to visual stimuli (PV+, Sst+ and VIP+) because previous work has focused on PV+ and Sst+ INs.

This results chapter is divided into four sections: one section for each IN subtype, and then a fourth section comparing results between subtypes.

3.2 THE EFFECTS OF PV+ INS ON PYR CELL CRFS

We recorded from 55 putative Pyr cells in 5 mice while stimulating PV+ INs, and 37 met our inclusion criteria (see section 2.5.3). Electrophysiological recording depth was not correlated with the changes in any parameter ($p > 0.05$). LED intensities reported here are the measurements recorded at the cortical surface, but we are aware that neurons in deeper layers receive different levels of photostimulation due to light scattering by cortical tissue (Yizhar et al., 2011; Yona et al., 2016). However, because INs of the same subtype are connected with gap junctions, superficial ChR2 activation could still affect deeper layers even if less light penetrates deeper layers (Karnani et al., 2016). Figure 11 shows CRFs for four example cells from our sample, with control responses shown as solid black circles fit with solid black lines, and PV+ photostimulated responses as desaturated red circles fit with dashed red lines. For all data presented in this chapter, spike rates were normalized to control responses to full contrast gratings (Michaelson contrast = 1). PV+ IN activation exclusively caused rightward and downward changes in Pyr cell CRFs, thereby decreasing Pyr cell sensitivity to contrast. The responses in Figures 11A-C show larger photostimulation induced decrements at high contrasts than at low contrasts, whereas the cell in Figure 11D had similar sized decrements across contrasts. The sigmoid functions fitted to the data points allowed us to extract parameters to quantify photostimulation induced changes.

For a subset of cells we recorded CRFs at two or more LED intensities; this allowed us to investigate within individual cells how changes in CRFs were related to the amount of Pyr cell suppression. The importance of this kind of data for comparing results across different laboratories was noted by Lee et al. (2014). Figure 12A shows data from a Pyr cell where visual responses were modulated with two LED intensities, 0.04 mW/mm^2 and 0.1 mW/mm^2. For this cell, the CRF shifted further rightward and downward when PV+ INs were stimulated with more intense LED photostimulation, which was expected based on previous reports (Atallah et al., 2012).
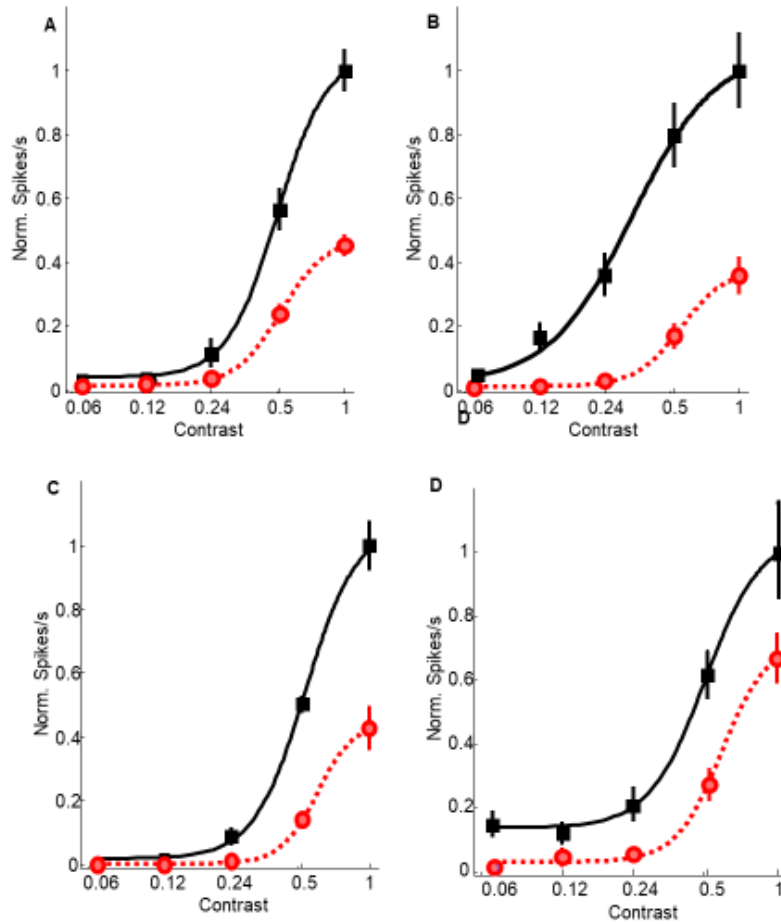
Figure 11: Example CRFs showing the effects of PV+ IN photostimulation on contrast responses. (A-D) CRFs from four example cells, with contrast on the x-axis and normalized spike rate on the y-axis. Control and Opto responses are shown as solid black squares and desaturated red circles, respectively. Curves represent the best fit of a Naka-Rushton function to the control (black solid) or Opto (red dashed) data. All error bars represent SEM.

To quantify CRF parameter changes in contrast coding within one neuron at two different LED intensities, we compared photostimulation-induced changes in Pyr cell responses and sigmoid fit parameters. To do this, we normalized our data to the lower of the two LED intensities so we could calculate changes in octaves from the dim LED condition to the bright LED condition. For example, to normalize AUC differences between dim and bright LED conditions, we subtracted the changes in AUC caused by both the high and dim LED conditions from the changes induced by dim condition so our normalized octave change for the dim condition was always 0, and the normalized bright LED octave change was relative to the dim condition:

$$Dim\ LED\ Octave\ Normalization: Dim\ LED(\Delta Parameter) - Dim\ LED(\Delta Parameter)$$

$$Bright\ LED\ Octave\ Normalization: Dim\ LED(\Delta Parameter) - Bright\ LED(\Delta Parameter)$$

This normalization was done for all five CRF parameters and Pyr cell activity change (equation 10), and ΔParameter was calculated for each parameter as outlined in Chapter 2.

$$Norm.\ Activity\ Change = \left(\frac{Mean\ Opto\ Resp.}{Max\ Ctrl\ Resp.} - \frac{Mean\ Ctrl\ Resp.}{Max\ Ctrl\ Resp.}\right) \times 100 \qquad (10)$$

We calculated photostimulation induced activity changes by normalizing the maximum responses from both conditions to the control response at full contrast and subtracted the normalized Control response from the normalized Opto response such that negative values indicated suppression and positive values indicated facilitation. Some cells were stimulated at ≥3 different irradiances, and we included only the highest and the lowest intensities; this was done with the intention of most accurately demonstrating the effects of varying LED brightness, therefore we did not include the intermediate LED intensities. The graphs in Figure 12B, D, F, H and J shows octave shifts for ΔAUC, ΔR_{Max}, ΔR_{Min}, Δc_{50} and $\Delta log\ Slope$, respectively, from five Pyr cells. In these plots, the data points represent octave changes for the bright LED condition and the asterisk represents the control dim LED condition. The length of the grey line connecting the asterisk to the data point represents the relative difference between the dim and bright conditions. All the

data points fall to the left of the asterisk, indicating that higher LED intensity always produced a bigger change in the normalized activity change than the lower LED intensity. Changes in the sigmoid parameters were affected in different ways when LED intensity increased. For AUC, all points were below the asterisk, indicating that changes in AUC were greater with higher LED intensities (Figure 12B). Changes in R_{Min} were barely affected by LED intensity (Figure 12F), and changes in R_{Max} (Figure 12D), c_{50} (Figure 12H), and log slope (Figure 12J) were all moderate.

To quantify if LED intensity affected the magnitude and of octave changes we calculated the vector sum of our octave changes, converted these values to radians, and plotted the resultant summed vectors on polar plots (shown as red lines in Figures 12C, E, G I and K). We then performed a permutation analysis on the change in each parameter by randomizing our data (i.e. randomized the changes in Pyr cell responses/sigmoid fit parameters so they were not organized based on contrast level or dim/bright LED condition) and then calculated the vector sums for the randomized data 10,000 times. To determine whether the observed vector sums were caused by differences in LED intensity rather than random noise, we plotted the 97.5 and 2.5 percentile values of the radii (which is the magnitude of change, eqn 11) from our permutations as black circles.

$$Radius = \sqrt{(sum\ of\ x\ values)^2} + \sqrt{(sum\ of\ y\ values)^2} \qquad (11)$$

where sum of x and y values are the sums of the 10,000 combinations of changes in Norm. Spike Rate (x values) and changes in sigmoid fit parameters (y values). We reasoned that the radius of our "real" vector sums exceeded the 97.5 percentile from our permutation analyses then we could be reasonably sure that the intensity of the LED was affecting the magnitude of change in sigmoid fit parameters. To determine the angles of our permutated vector sums we used MATLAB's `cart2pol` function which transforms Cartesian to polar coordinates and calculates the resultant angle in radians. To estimate whether the "real" angle of our vector sum was caused by the difference in LED intensity, we calculated two-tail z-scores at $p = 0.05$:

$$z = x - \frac{\mu}{\sigma} \qquad (12)$$

where the critical angle (x) was determined based on a Z-score of ±1.96 and the mean (μ) and the standard deviation (σ) were both calculated using MATLAB's Circular Statistics Toolbox. We plotted the angles that would produce right- and left-tail z-scores as blue triangles such that the triangles encompassed the outer 5% of the distribution. Therefore, we reasoned that if our vector sum fell within this triangle, we could be confident that the difference in the change in sigmoid fit parameters between the two LED intensities was indeed caused by the LED intensity and not random noise. This is different than looking at the radius of the vector because it isolates the change in parameter from the change in spike rate, which the radius of the vector sum does not. The results from our permutation analyses indicate that the magnitude of the octave changes we observed as a result of activating PV+ INs could not have occurred by chance, but the angle of the octave changes could have, for all parameters (Figure 12C, E, G I and K).
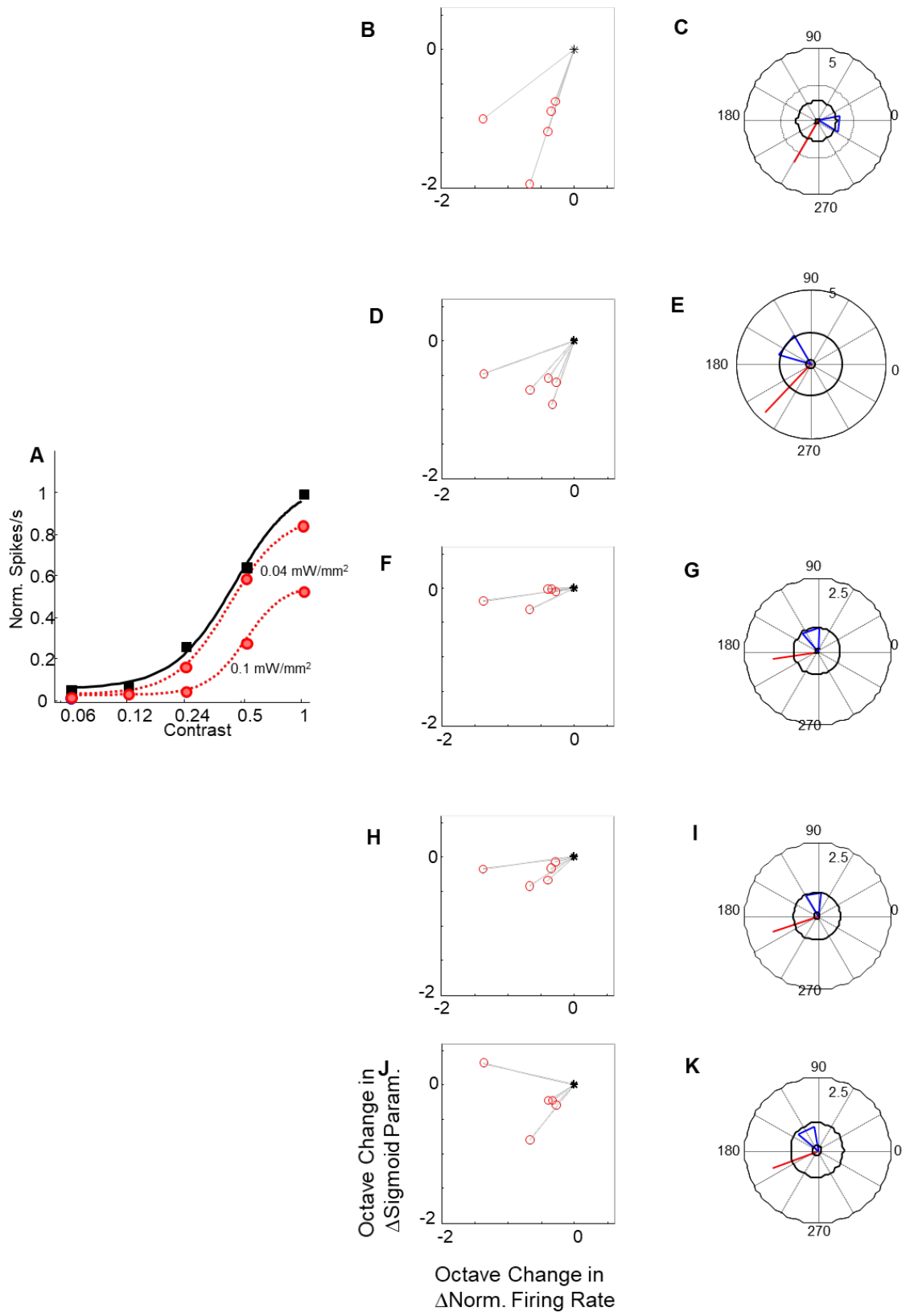
Figure 12: Effects of two levels of photostimulation of PV+ INs on a single Pyr cell. (A) Example CRF from a cell stimulated at two different photostimulation intensities. Format is identical to figure 11, photostimulation intensities inset. Middle column, B-J: Scatterplots showing the octave changes in firing rate (x-axis) and parameter change (y-axis) for AUC, R_{Max}, R_{Min}, c_{50} and log Slope, respectively. Data is normalized to the dimmer photostimulation intensity, indicated by the asterisk. Far left column, C-K: Polar plots showing the vector sum from the adjacent scatter plot. Black circles and blue triangles indicate percentile cutoffs as described in the text.

For most of our Pyr cell sample recorded in PV+*Cre mice, we only obtained data with one LED intensity. We aimed to induce moderate suppression of Pyr activity because if photostimulated CRFs were flat due to too much photostimulation, or unchanged as a result of too little photostimulation, we would be unable to quantify how the photostimulated IN subtype altered Pyr cell CRFs. We have incorporated the cells from Figure 12 into the following set of analyses but included only the recording with the larger change in AUC under the assumption that this condition would be best for characterizing the nature of the inhibition. We did not divide cells into simple and complex because we have previously not found differences in responses to contrast between these two cell types (e.g. King et al., 2015). To determine the overall impact of PV+ INs activation on our sample of Pyr cell CRFs we generated averaged normalized CRFs (Figure 13A), and observed a large decrease in R_{Max}, but very little change to R_{Min}. We then plotted Control CRF parameters against Opto CRF parameters from individual cells (Figure 12B-F). AUC and R_{Max} significantly decreased (Figure 13B and C). R_{Min} was moderately affected by PV+ activation, although still significantly decrased (Figure 13D). c_{50} significantly shifted rightwards, and log Slope was not consistently altered (Figure 13F, p = 0.14). The p-values from statistical comparisons are in table 2. All of these changes are consistent with CRFs that decreased their maximum spike rate and became less sensitive to contrast.

After determining that PV+ IN activation does influence Pyr cell CRFs, we wanted to see whether the amount of Pyr cell suppression was correlated with the magnitude of parameter changes. This is a crucial analysis because as mentioned, previous findings may have conflicted due to different photostimulation protocols, including how much Pyr cells were suppressed (Lee et al., 2014; El-Boustani et al., 2014).
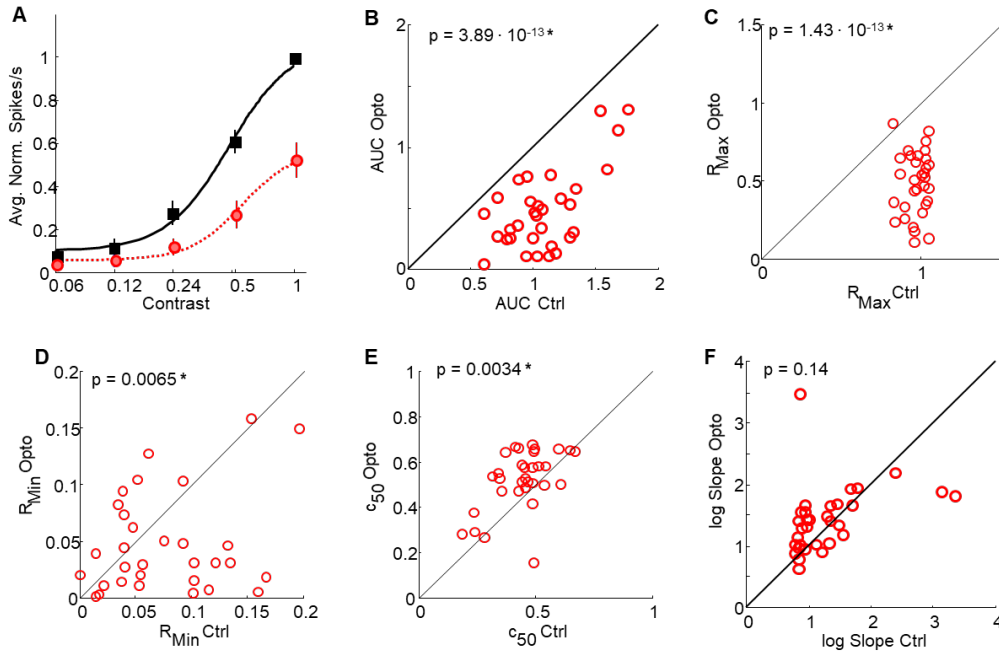
Figure 13. Effects of PV+ IN photostimulation on CRF parameters. (A) Average normalized CRFs from Pyr cells recorded from during PV+ IN activation. Format is identical to Figure 10. (B-F) Scatterplots comparing sigmoid fit parameters between Control (x-axis) and photostimulated (y-axis) curves; B-F plots show AUC, RMax, RMin, c50 and log slope, respectively. P-values are inset.

Table 2: Control and Opto means from sigmoid parameters, and corresponding p-values, quantifying how PV+ INs affect Pyr cell responses to contrast.

Parameter	Ctrl Mean ± 95% C.I.	Opto Mean ± 95% C.I.	p-value
AUC	1.07 ± 0.1	0.49 ± 0.11	$3.9 \cdot 10^{-13}$
R_{Max}	0.97 ± 0.02	0.48 ± 0.07	$1.43 \cdot 10^{-13}$
R_{Min}	0.08 ± 0.02	0.04 ± 0.015	0.0065
$c50$	0.45 ± 0.04	0.52 ± 0.045	0.0034
log Slope	1.27 ± 0.2	1.43 ± 0.19	0.14

To determine whether the relationship between parameter changes and photostimulation was better described with LED intensity or the magnitude of Pyr cell suppression we first examined the relationship between LED intensity and Pyr cell activity change and found that there was no correlation (Figure 14A, $r^2 = 7.95 \cdot 10^{-5}$, p = 0.96). Therefore, we decided to use activity change because it best describes how PV+ IN activation altered CRF fit parameters. We suppressed Pyr cell activity by 22%, with a range of 5-38% suppression. The magnitude of CRF shifts appear to largely depend on the amount of Pyr cell suppression because we observed significant correlations for AUC (Figure 14B, $r^2 = 0.97$, p = $1.25 \cdot 10^{-24}$), R_{Max} (Figure 14C, $r^2 = 0.41$, p = $8.5 \cdot 10^{-5}$), R_{Min} (Figure 14D, $r^2 = 0.38$, p = 0.0002), and c_{50} (Figure 14E, $r^2 = 0.14$, p = 0.03), but not for log Slope (Figure 14F, $r^2 = 0.04$, p = 0.3). Correlations between Pyr cell suppression and AUC change were tightly correlated because so much of AUC comes from the maximum response to contrast. Figure 14G shows ΔR_{Max} vs. ΔR_{Min}, which is a rudimentary way of determined whether a neuron underwent divisive or subtractive inhibition, and 36/37 cells experienced a larger decrease in R_{Max} than R_{Min} (p = $2.934 \cdot 10^{-13}$, paired t-test), which indicative of divisive scaling. However, a comparing SS_{Res} between the models is a more accurate way to quantify divisive vs. subtractive inhibition due to spiking nonlinearity, (see Figure 16).

Next, we examined whether PV+ IN activation was more likely to induce divisive or subtractive inhibition, which has been the primary focus of previous research. We quantified divisive vs. subtractive inhibition in two ways: (1) we compared ΔR_{Max} with ΔR_{Min} because larger changes in R_{Max} are characteristic in divisive shifts (Figure 14G), and (2) we calculated the SS_{Res} for both divisive and subtractive models because a

larger residual indicates a poorer fit between the data and a model. An F-statistic (SS_{Res} div/SS_{Res} sub) greater than 1 indicates a better fit to the divisive model. Figure 15A-B shows two example cells with the control curves (black) and models where this function was scaled divisively (dashed purple curves) and shifted subtractively (dotted green curves). The cell in Figure 15A experienced divisive inhibition, which can be seen by the divisive curve better fitting the photostimulated data points and is confirmed with a smaller SS_{Res}, and the cell in Figure 15B shifted subtractively. We then calculated whether our sample had more cells that were divisively scaled or subtractively shifted. However, as described above the spike rate nonlinearity may have limited the amount that responses at low contrasts could decrease, hence limiting the decrease in R_{min}. Therefore, for a refined measure of divisive vs subtractive inhibition we compared SS_{res} between the two models, and we found that the residuals were not as clearly segregated; 19/37 cells better fit the divisive model, and 18/37 cells fit the subtractive model better (Figure 15C). However, as can be seen in the scatter plot in Figure 15C that compares divisive SS_{Res} (x-axis) and subtractive SS_{Res} (y-axis) values, the subtractive values fall further from the line of equality, indicating that these residuals are larger than those from the divisive model. Indeed, the divisive model was overall a significantly better fit (Figure 15C, p = 0.0176, paired t-test), which agrees with a majority of previous work (Atallah et al., 2012; Wilson et al., 2012).

Lastly, we wanted to determine whether the type of inhibition induced by PV+ IN activation was correlated with the amount of Pyr cell suppression. Figure 15D shows octave shifts for the F-Stat for the subset of five cells recorded from at two LED irradiances. Format and analyses are identical to that in Figure 12. The octave shifts suggest that divisive scaling provided better fits when neurons were more suppressed (Figure 15D). We ran identical permutation analyses for magnitude of octave change for the F-statistic as in Figure 12, and our permutation tests suggest that the magnitude of octave changes depend on LED intensity, but the angle does not (Figure 15E). We then examined this relationship in our sample of cells tested with one LED intensity. Figure 15F shows data from our full sample, and we found a moderate, but significant, correlation between Pyr cell suppression and the F-stat ($r^2 = 0.21$, p = 0.008). Both

Figures 15D and 15F suggest that Pyr cells that have more PV+ IN-induced suppression are better described by divisive scaling.

Overall, the results in this section demonstrate that PV+ IN activation decreases Pyr cell contrast sensitivity, with significant changes to CRFs for AUC, R_{Max}, R_{Min} and c_{50} parameters. We also show that both the magnitude and type of sigmoid parameter changes are largely dependent on the amount of PV+ IN induced Pyr cell suppression. Finally, divisive models fit our data with significantly smaller residuals than subtractive models.
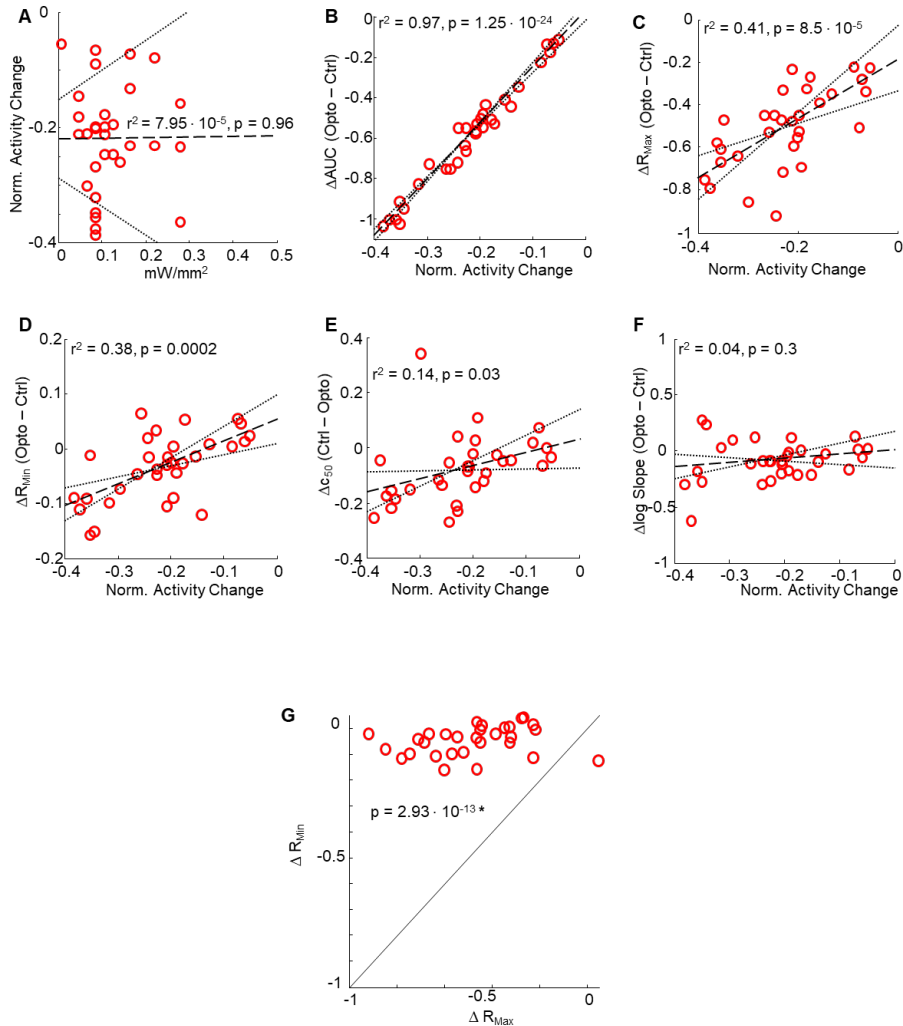
Figure 14. Effects of PV+ IN-induced suppression on CRF parameters. (A) Correlation between surface LED brightness (x-axis) with Pyr cell suppression (y-axis). We found no correlation, so used Pyr cell suppression as our measure of PV+ IN induced CRF fit parameter changes. (B-F) Correlation of Pyr cell suppression (x-axis) with change in sigmoid parameters (y-axis) for AUC, R_{Max}, R_{Min}, c_{50} and log slope, respectively. Long dashed line represents the regression line, and shorted dashed lines represent 95% confidence intervals. R^2 and p-values are inset. (G) Comparison of changes in R_{Max} and R_{Min} as a result of photostimulation.

A SS$_{Res}$ Divisive = 0.005
SS$_{Res}$ Subtractive = 0.023

B SS$_{Res}$ Divisive = 0.016
SS$_{Res}$ Subtractive = 0.001

C p = 0.0176 *

D Octave Change in ΔF-Stat.
Octave Change in ΔNorm. Firing Rate

E

F r^2 = 0.21, p = 0.008
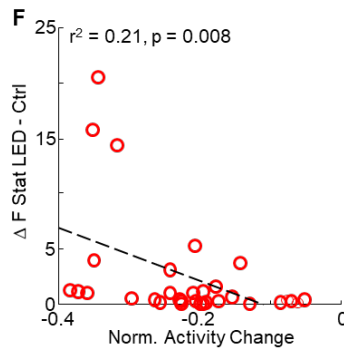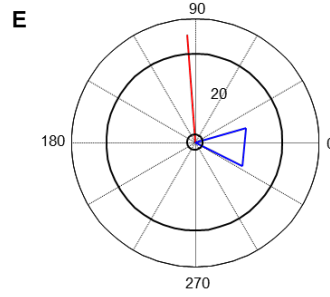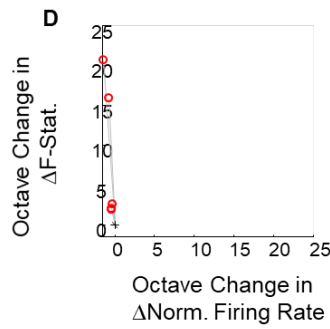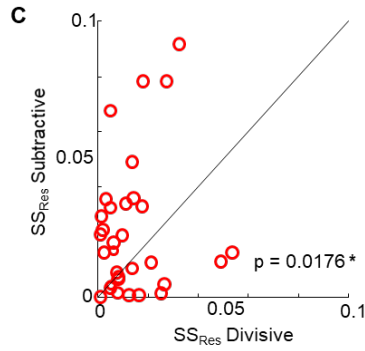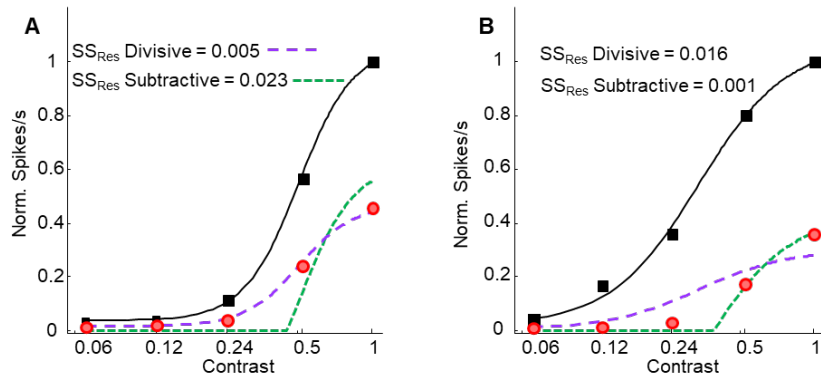
Figure 15. Quantifying PV+ IN-induced divisive vs. subtractive inhibition. (A&B) CRFs from two example cells, one that demonstrated divisive scaling (A) and one that experienced a subtractive shift (B). Color and format are identical to figure 11, except the Opto curve has been exchanged for the divisive (purple dashed curve) and subtractive (green dashed curve) models. SSRes for both models are inset. (C) A scatterplot comparing SS_{Res} from the divisive model (x-axis) and the subtractive model (y-axis) for all cells. P-value inset. (D) Octave shifts in Firing Rate (x-axis) and F-statistic (y-axis) for the subset of cells stimulated at two photostimulation intensities. Data is normalized to the dimmer photointensity. (E) A polar plot showing the vector sum for octave shifts and the percentile cutoffs for the radius and angle. Figure format is identical to figure 12. (F) Correlation of Pyr cell suppression (x-axis) with change in the F-statistic (y-axis). Format identical to Figure 14.

3.3 THE EFFECTS OF SST+ INS ON PYR CELL CRFS

We recorded from 46 putative Pyr cells in 5 mice while stimulating Sst+ INs, and 22 met our inclusion criteria (see section 5.2.3). As with the recordings in section 3.1, cortical depth was not correlated with the effects of photostimulation on any CRF parameter so we did not segregate by cortical layer. Figure 16 shows four example cells from our sample, demonstrating the range of effects we observed as a result of Sst+ IN activation. For these CRFs, Control responses are indicated by solid black squares fit with solid black lines, and Sst+ photostimulated responses are desaturated blue squares fit with dashed blue lines. Identical to PV+ IN activation, stimulating Sst+ INs exclusively caused rightward and downward shifts in Pyr cell CRF functions, thereby decreasing Pyr cell sensitivity to contrast. Figures 16A-C show cells that had substantial decreases in responses to high contrasts but little-to-no change in responses to low contrast. Figure 16D shows a cell that had consistent suppression across all contrasts.

Because the analyses discussed for the following four figures follow the same logic as Figures 11-15 in section 3.1.1, therefore for brevity we will only report findings from Sst+ photostimulation in this section, and not repeat the underlying motivation behind each analysis.

As with PV+ IN perturbation, we recorded CRFs from a subset of cells at multiple LED intensities while stimulating Sst+ INs. Figure 17A shows a Pyr cell that was recorded from where Sst+ INs were photoactivated with two LED intensities: 0.16 mW/mm^2 and 2.1 mW/mm^2. Similar to our findings during PV+ IN photostimulation, Pyr cell CRFs often shifted further when Sst+ INs were stimulated at a higher surface LED irradiance. The data in Figure 17 is analyzed and organized identically to Figure 12, but represents data from nine Pyr cells that were photostimulated at two different LED intensities in Sst-Cre*Ai32 mice. When looking at the octave shifts shown by scatter plots in Figure 17B, D, F, H and J it can be seen that changes in AUC and R_{Max} were the most affected by differences in LED intensity. The results from our permutation analyses indicate that magnitude of changes caused by different photostimulation intensities could not have occurred by chance, but the angle could have, for all CRF parameters: AUC (Figure 17C), R_{Max} (Figure 17E), R_{Min} (Figure 17G), c_{50} (Figure 17I) and log Slope (Figure 17K).
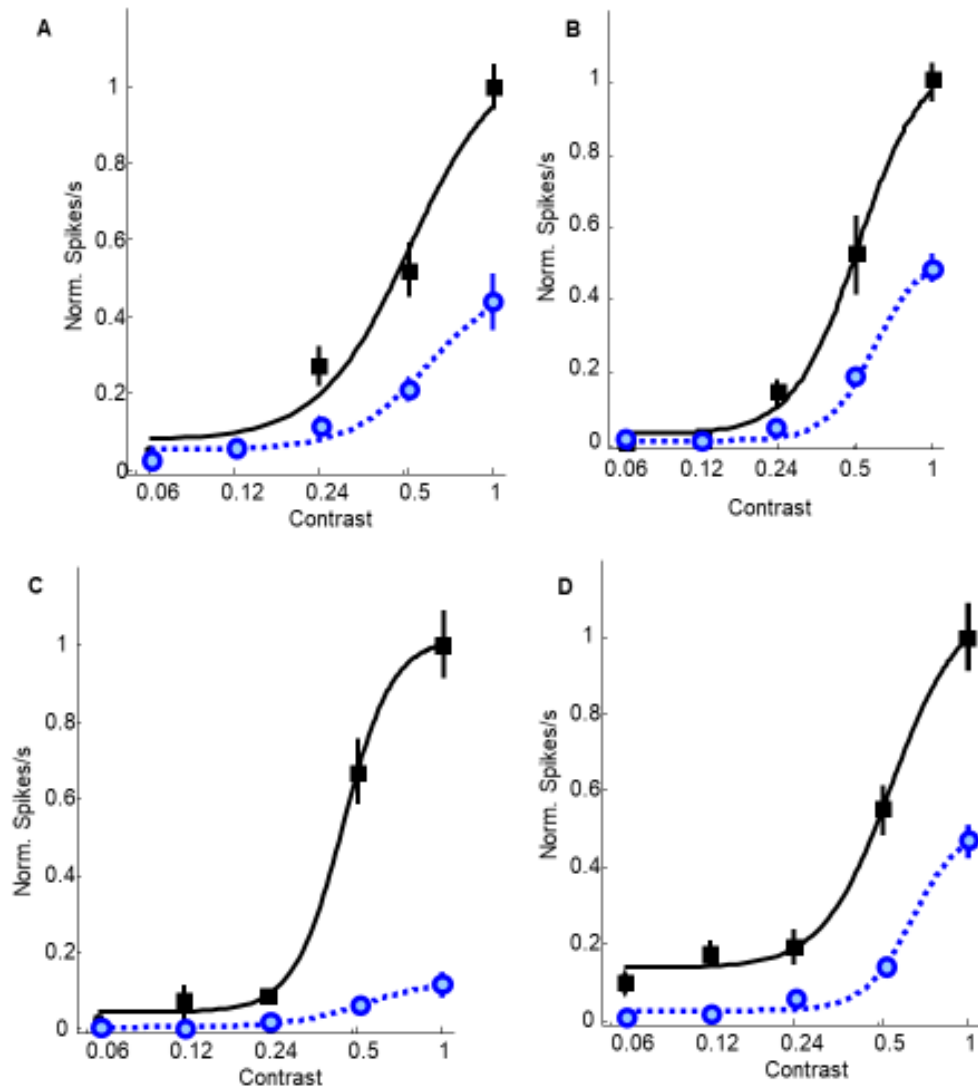
Figure 16. Example CRFs showing the effects of Sst+ IN photostimulation on contrast responses. (A-D) CRFs from four example cells, with contrast on the x-axis and normalized spike rate on the y-axis. Control and Opto responses are shown as solid black and desaturated blue circles, respectively. Curves represent the best fit of a Naka-Rushton function to the control (black solid) or Opto (blue dashed) data. All error bars represent SEM.
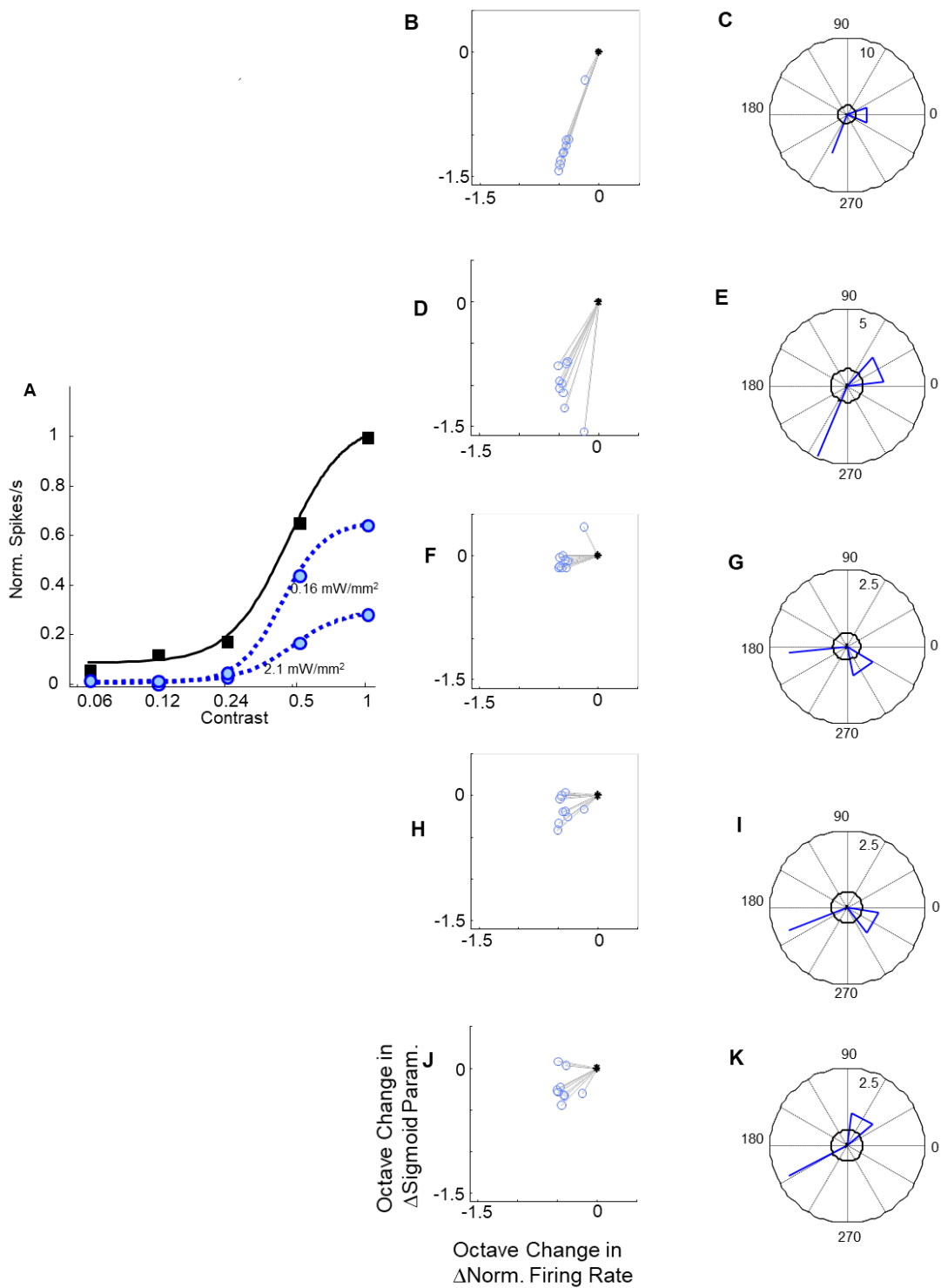
Figure 17: Effects of two levels of photostimulation of Sst+ INs on a single Pyr cell. (A) Example CRF from a cell stimulated at two different photostimulation intensities. Format is identical to figure 11, photostimulation intensities inset. Middle column, B-J: Scatterplots showing the octave changes in firing rate (x-axis) and parameter change (y-axis) for AUC, R_{Max}, R_{Min}, c_{50} and log Slope, respectively. Data is normalized to the dimmer photostimulation intensity, indicated by the asterisk. Far left column, C-K: Polar plots showing the vector sum from the adjacent scatter plot. Black circles and blue triangles indicate percentile cutoffs as described in the text.

To determine the overall effect of photostimulating Sst+ INs on Pyr cell CRFs we generated averaged normalized curves, and as with PV+ IN activation, observed a noticeable decrease in R_{Max} compared to R_{Min} (Figure 18A). We then plotted Control CRF parameters against Opto CRF parameters from individual cells (Figure 18B-F). AUC, R_{Max} and R_{Min} significantly decreased (Figure 18B-D). c_{50} shifted rightwards in 21/22 cells, which was significant (Figure 18E), and log Slope was not consistently altered (Figure 18F). The p-values for statistical comparisons are in table 3. All these changes are consistent with CRFs that decreased their maximum spike rate and became less sensitive to contrast.

To determine whether the magnitude of activity suppression caused by Sst+ activation was correlated with CRF shifts, we plotted the change in CRF parameters against the amount of Pyr cell suppression. We suppressed Pyr activity on average by 27% ranging from 10-61%. We also did not find a correlation between surface photostimulation intensity and Pyr activity change (Figure 19A, $r^2 = 0.11$, $p = 0.13$), and therefore used activity change as a measure of the effect of Sst+ IN photostimulation. We observed activity-dependent shifts in CRFs, although different parameters were correlated than with PV+ IN activation. We found significant correlations for AUC (Figure 19B, $r^2 = 0.99$, $p = 2.97 \cdot 10^{-20}$), R_{Min} (Figure 19D, $r^2 = 0.37$, $p = 0.0025$), c_{50} (Figure 19E, $r^2 = 0.52$, $p = 0.00014$), and log Slope (Figure 19F, $r^2 = 0.52$, $p = 0.00014$),
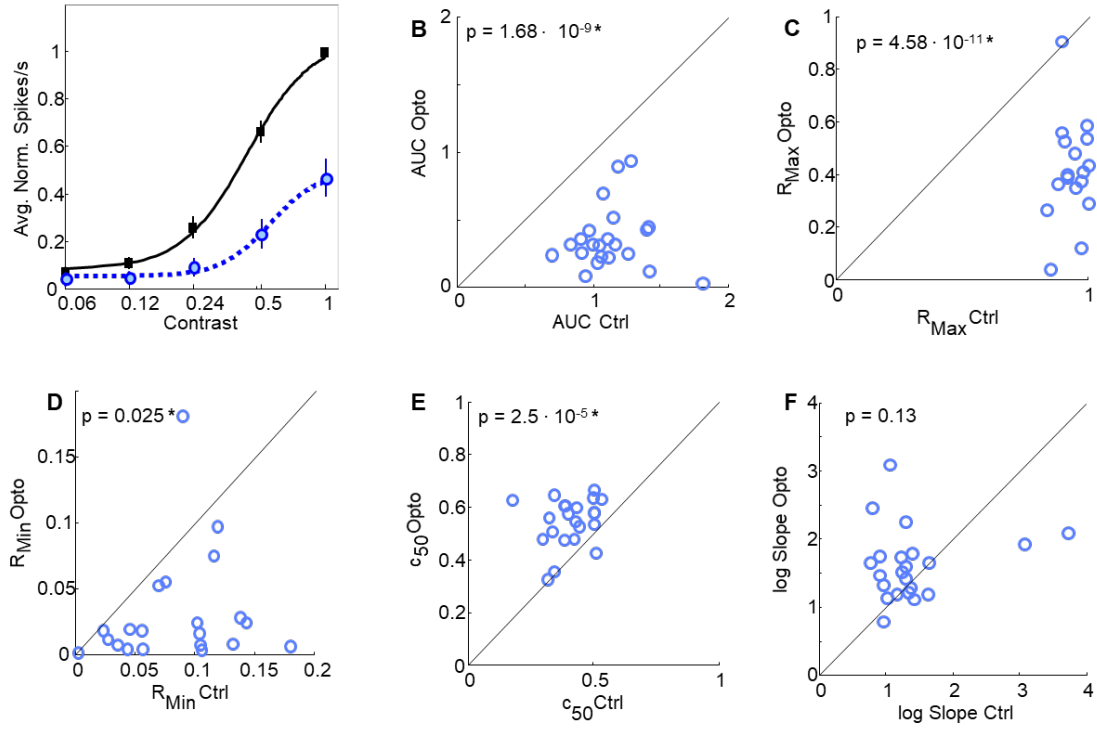
Figure 18. Effects of Sst+ IN photostimulation on CRF parameters. (A) Average normalized CRFs from Pyr cells recorded from during Sst+ IN activation. Format is identical to Figure 15. (B-F) Scatterplots comparing sigmoid parameters between Control (x-axis) and Opto (y-axis) curves; B-F plots show AUC, RMax, RMin, c50 and log slope, respectively. P-values are inset.
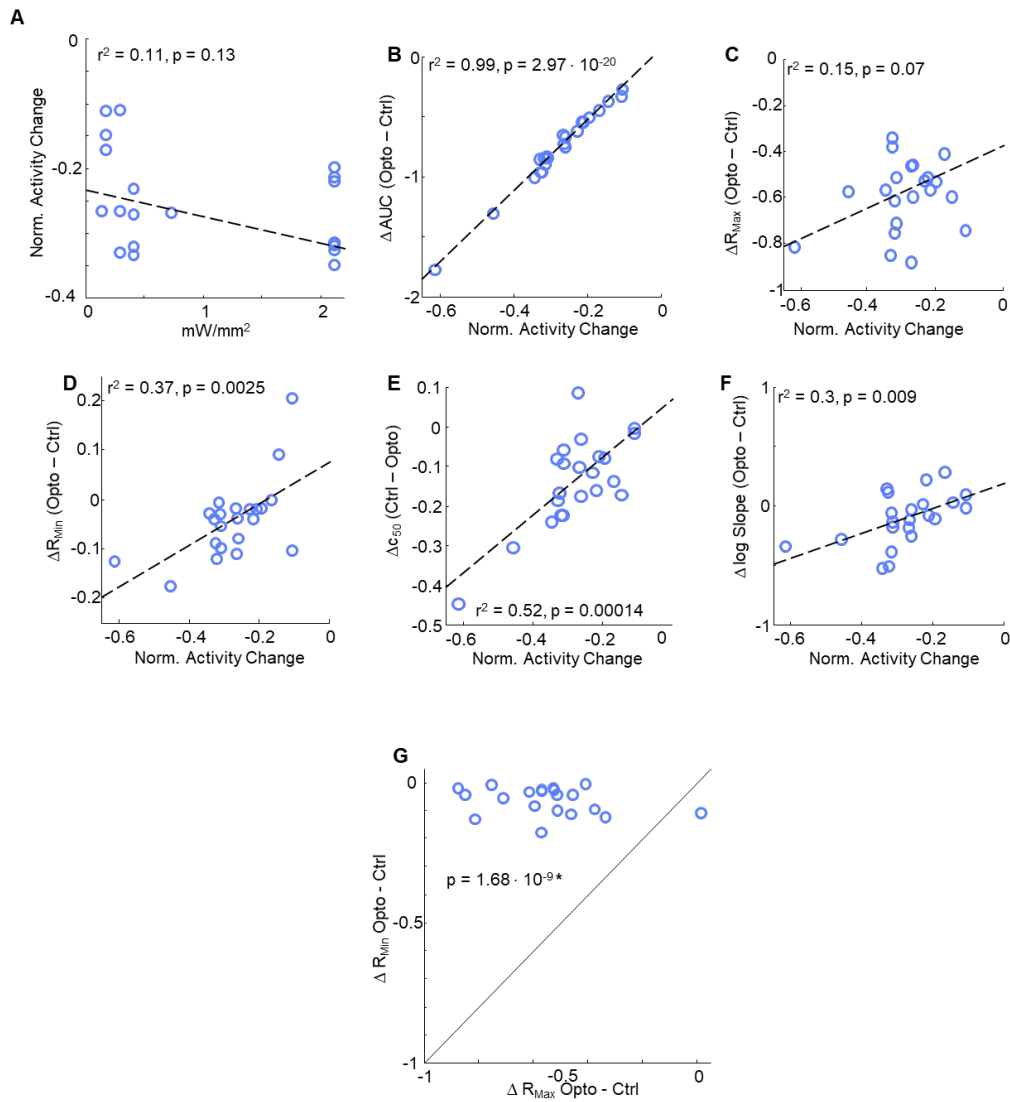
Figure 19. Effects of Sst+ IN-induced suppression on CRF parameters. (A) Correlation of surface LED intensity (x-axis) with Pyr cell suppression (y-axis). (B-F) Correlation of Pyr cell suppression (x-axis) with change CRF parameters (y-axis) for AUC, RMax, RMin, c50 and log slope, respectively. Long dashed line represents the regression line, and short dashed lines represent 95% confidence intervals. R^2 and p-values are inset. (G) Comparison of changes in R_{Max} and R_{Min} as a result of photostimulation.

but not for R_{Max} (Figure 19C, $r^2 = 0.15$, p = 0.07). Overall, even though slightly different parameters than expected were correlated with activity change, CRF shifts induced by Sst+ IN activation were largely dependent on the magnitude of Pyr cell suppression. Figure 20C shows ΔR_{Max} vs. ΔR_{Min}, and as with PV+ IN activation, it is obvious that most cells experienced a larger drop in R_{Max} (21/22, p = $1.68 \cdot 10^{-9}$, paired t-test), indicative of divisive scaling. Below we compare SS_{Res} between the two models as we did for PV+ INs.

Table 3: Control and Opto means from sigmoid parameters, and corresponding p-values, quantifying how PV+ INs affected Pyr cell responses to contrast.

Parameter	Ctrl Mean ± 95% C.I.	Opto Mean ± 95% C.I.	p-value
AUC	1.12 ± 0.08	0.37 ± 0.08	$1.68 \cdot 10^{-9}$
R_{Max}	0.96 ± 0.02	0.39 ± 0.06	$4.58 \cdot 10^{-11}$
R_{Min}	0.08 ± 0.01	0.04 ±0.019	0.025
c50	0.41 ± 0.03	0.54 ± 0.03	$2.6 \cdot 10^{-5}$
log Slope	1.4 ± 0.2	1.63 ± 0.18	0.13

After determining that Sst+ IN activation does affect Pyr cell CRFs, we assessed whether the CRF changes were better described as divisive or subtractive. Figure 20A-B show two example CRFs with the Control curves shifted divisively and subtractively. Divisive shifts are shown with longer, purple dashes and subtractive shifts are shown with shorter, green dashes. The cell in Figure 20A appeared to scale divisively, whereas the cell in Figure 20B appeared to shift subtractively. We then looked at whether Sst+ IN activation was more likely to induce subtractive or divisive inhibition by using the same measures described in section 3.1.1. When we compared divisive and subtractive SS_{Res} we again found that there was not a consistent type of inhibition: half of our sample had smaller divisive SS_{Res} (11/22), and the other half had smaller subtractive SS_{Res} (Figure 20C). Unlike our PV+ perturbed sample, the SS_{Res} from both models fell within the similar ranges relative to the line of equality (except for two cells that were extremely divisive), and therefore one model did not better describe CRF changes in this sample of Sst+ perturbed Pyr cells (p = 0.48, paired t-test). Previous work reports both divisive and subtractive shifts as a result of Sst+ stimulation (Wilson et al., 2012; Lee et al., 2012).

Lastly, we wanted to determine whether the type of inhibition caused by Sst+ IN activation was correlated with the amount of Pyr cell suppression; Figure 20D looks at the octave shifts in the F-Stat for the subset of nine cells recorded at two LED irradiances. In this plot, data that is leftward and upward from the black asterisk indicates a more divisive shift as a result of larger decreases in Pyr cell activity, and it can be seen that cells trended towards more divisive inhibition as a result of brighter photostimulation. The results from our permutation analyses indicate that the differences we observed in the magnitude of F-Stat changes could not have occurred by chance, but the angle could have, during Sst+ IN activity at two different LED intensities (Figure 20E). We then examined whether the type of inhibition provided by Sst+ INs was related to the amount of the resulting Pyr cell suppression in our population data. Figure 20H shows a poor correlation between the change in F-stat and activity change ($r^2 = 0.05$, $p = 0.3$), indicating that the F-Stat is not affect by the amount of Pyr suppression caused by Sst+ IN activation. These findings do not agree with one another, and it would likely be resolved with a larger sample of Pyr cells where Sst+ INs were stimulated at multiple LED intensities.
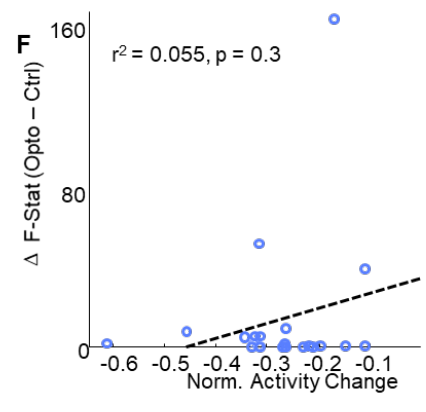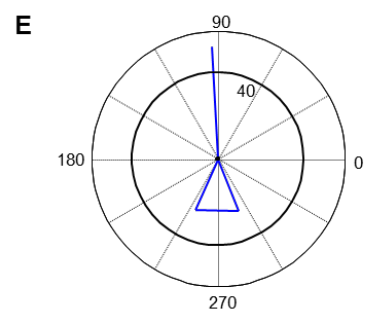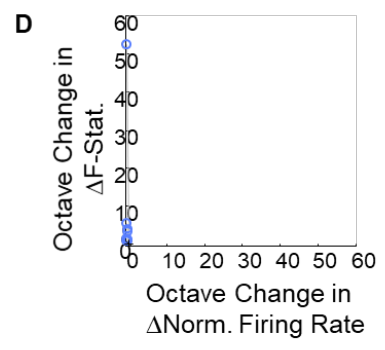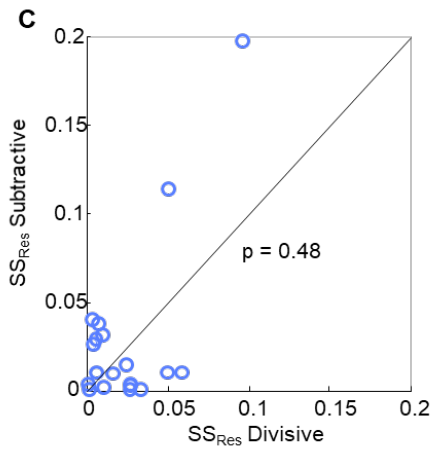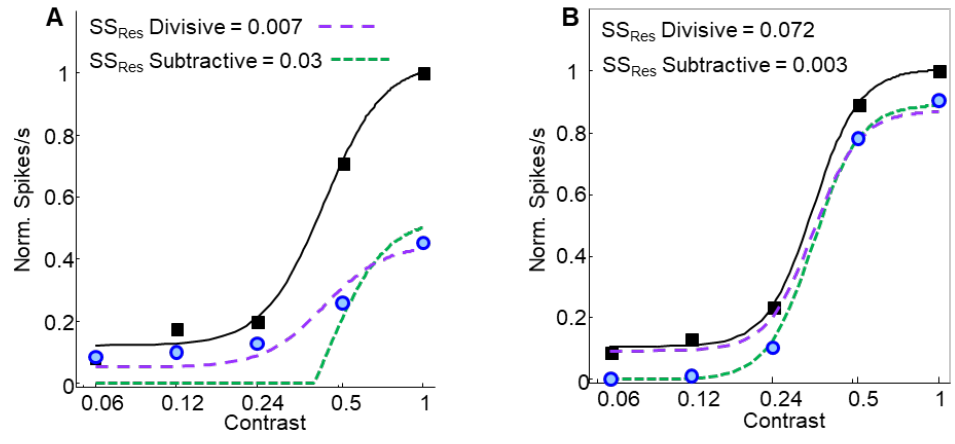
Figure 20. Quantifying Sst+ IN-induced divisive vs. subtractive inhibition. (A&B) CRFs from two example cells, one that demonstrated divisive scaling (A) and one that experienced a subtractive shift (B). Color and format are identical to figure 11, except the Opto curve has been exchanged for the divisive (purple dashed curve) and subtractive (green dashed curve) models. SSRes for both models are inset. (C) A scatterplot comparing SS_{Res} from the divisive model (x-axis) and the subtractive model (y-axis) for all cells. P-value inset. (D) Octave shifts in Firing Rate (x-axis) and F-statistic (y-axis) for the subset of cells stimulated at two photostimulation intensities. Data is normalized to the dimmer photointensity. (E) A polar plot showing the vector sum for octave shifts and the percentile cutoffs for the radius and angle. Figure format is identical to figure 17. (F) Correlation of Pyr cell suppression (x-axis) with change in the F-statistic (y-axis). Format identical to Figure 19.

Overall, the results in this section demonstrate that Sst+ IN activation also decreases Pyr cell contrast sensitivity, with significant changes to CRFs for AUC, R_{Min}, c_{50} and log Slope parameters. We also show that both the magnitude of sigmoid parameter changes are largely dependent on the amount of Sst+ IN induced Pyr cell suppression, and that divisive and subtractive models can describe photostimulation effects of individual Pyr quite well, but neither model was favoured across our sample.

3.4 THE EFFECTS OF VIP+ INS ON PYR CELL CRFS

We recorded from 288 putative Pyr cells in 20 mice while stimulating VIP+ INs, and 123 met our inclusion criteria (see section 5.2.3). As with the recordings in the previous two sections, depth was not correlated with the effects of photostimulation on any CRF parameter so we did not segregate recordings by cortical layer. Figure 21 shows CRFs from four example cells, demonstrating the range of effects we observed as a result of VIP+ IN activation. Surprisingly, VIP+ IN activation caused both leftward/upward (Pyr cell facilitation) and rightward/downward (Pyr cell suppression) shifts in CRFs, and therefore photostimulated responses are divided into two groups: facilitated cells are represented by yellow triangles oriented upwards, and suppressed responses are
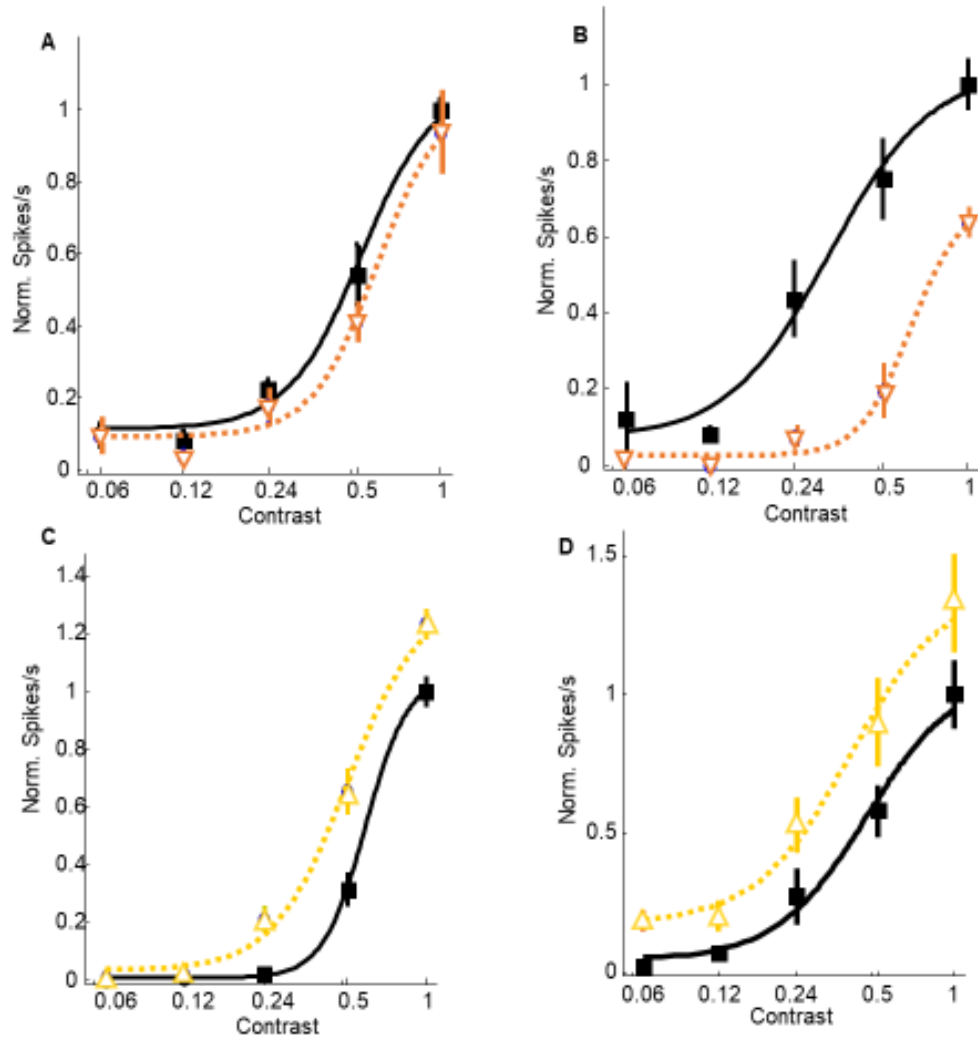
Figure 21. Example CRFs showing the effects of VIP+ IN photostimulation on contrast responses. (A-D) CRFs from four example cells, with contrast on the x-axis and normalized spike rate on the y-axis. A and B show CRFs from two cells that were suppressed by VIP+ IN activation, with Control and Opto responses shown as solid black and desaturated downward oriented orange triangles, respectively. C and D show CRFs from two cells that were facilitated with Control and Opto responses shown as solid black and desaturated yellow upward oriented triangles, respectively. Curves represent the best fit of a Naka-Rushton function to the data in the corresponding color of the data points. All error bars represent SEM.

downward oriented orange triangles. These CRFs are fit with sigmoids of corresponding colors, and control responses are solid black triangles fit with solid black lines. Figures 21A-B show two cells that were suppressed by VIP+ IN activation. Photostimulation of the neuron in Figure 21A appears to induce a subtractive shift. The CRFs in Figure 21B look similar to those we observed while photoactivating PV+ or Sst+ INs. Figure 21C-D shows two cells that were facilitated by VIP+ IN activation; the cell in Figure 21C has more facilitation at higher contrasts, whereas the cell in Figure 21D has similar increases across all contrasts.

As with PV+ and Sst+ IN photostimulation, while stimulating VIP+ INs we recorded CRFs from a subset of neurons at multiple LED intensities. Figure 22A shows a Pyr cell that was recorded from at two LED intensities: 0.002 mW/mm^2 and 2.1 mW/mm^2. In some recordings, we observed facilitation at one LED intensity and suppression at another, which is demonstrated in this example cell. Figure 21 shows data from 64 Pyr cells recorded at two different LED intensities, analyzed and organized as in Figures 12 and 17. Because VIP+ INs caused both facilitation and suppression, in these plots there are also data points above and to the right of the control asterisk, which represents cells that were facilitated and as such had an increase in sigmoid fit parameters. Our octave shift data suggest that spike rate induced changes from differing LED intensities were greatest for changes in AUC (Figure 22B), and R$_{Max}$ (Figure 22D), whereas changes in R$_{Min}$ (Figure 22F), c$_{50}$ (Figure 22H) and log Slope (Figure 22J) were much less affected by different LED intensities. As with PV+ and Sst+ INs, our permutation analyses using VIP+ data suggest that the magnitude of octave changes were significantly affected by LED intensity for all parameters, but the angle of octave changes were not (Figures 22C, E, G, I and K). In these polar plots only the 97.5 percentile radius cut-off can be seen because the 2.5 percentile radius is so small. This is sensible because the changes in CRF sigmoid fit parameters were much smaller when VIP+ INs were photostimulated compared to PV+ and Sst+ INs, and the positive and negative changes caused by Pyr cell suppression and facilitation cancel each other out.

To determine the overall effect of photostimulating VIP+ INs on Pyr cell CRFs we generated averaged normalized curves for both facilitated and suppressed responses (Figures 23A and B, respectively), and observed more subtle differences than with PV+

and Sst+ IN activation. We then plotted Control CRF parameters against Opto CRF parameters from individual cells (Figures 23C-G). VIP+ IN activation caused both suppression and facilitation, quantified identically to PV+ and Sst+ INs (eqn 10), therefore we ran a repeated measures ANOVA with optogenetic stimulation as the within factor and activation change (i.e. facilitation or suppression) as a between factor. We observed significant main effect differences for only two CRF parameters, R_{Min} (Figure 23E) and c_{50} (Figure 23F), but not for AUC (Figure 23C), R_{Max} (Figure 23D), or log Slope (Figure 23G). These findings are not surprising because by including both facilitated and suppressed cells in our statistical sample, positive and negative parameter changes cancel each other out. P-values are in table 4. However, because of this, we found interactions for all parameters except log Slope: AUC (Figure 23C), R_{Max} (Figure 23D), R_{Min} (Figure 23E), c_{50} (Figure 22F), log Slope (Figure 23G). p-values are in table 5. These interactions were expected because CRF parameters quantitatively describe CRFs and facilitated vs. suppressed curves have opposite polarity changes in all parameters except for log Slope.

A

2.1 mW/mm²

0.002 mW/mm²

Spikes/s

Contrast

B

D

F

H

J

C

E

G

I

K

Octave Change in
ΔSigmoid Param.

Octave Change in
ΔNorm. Firing Rate
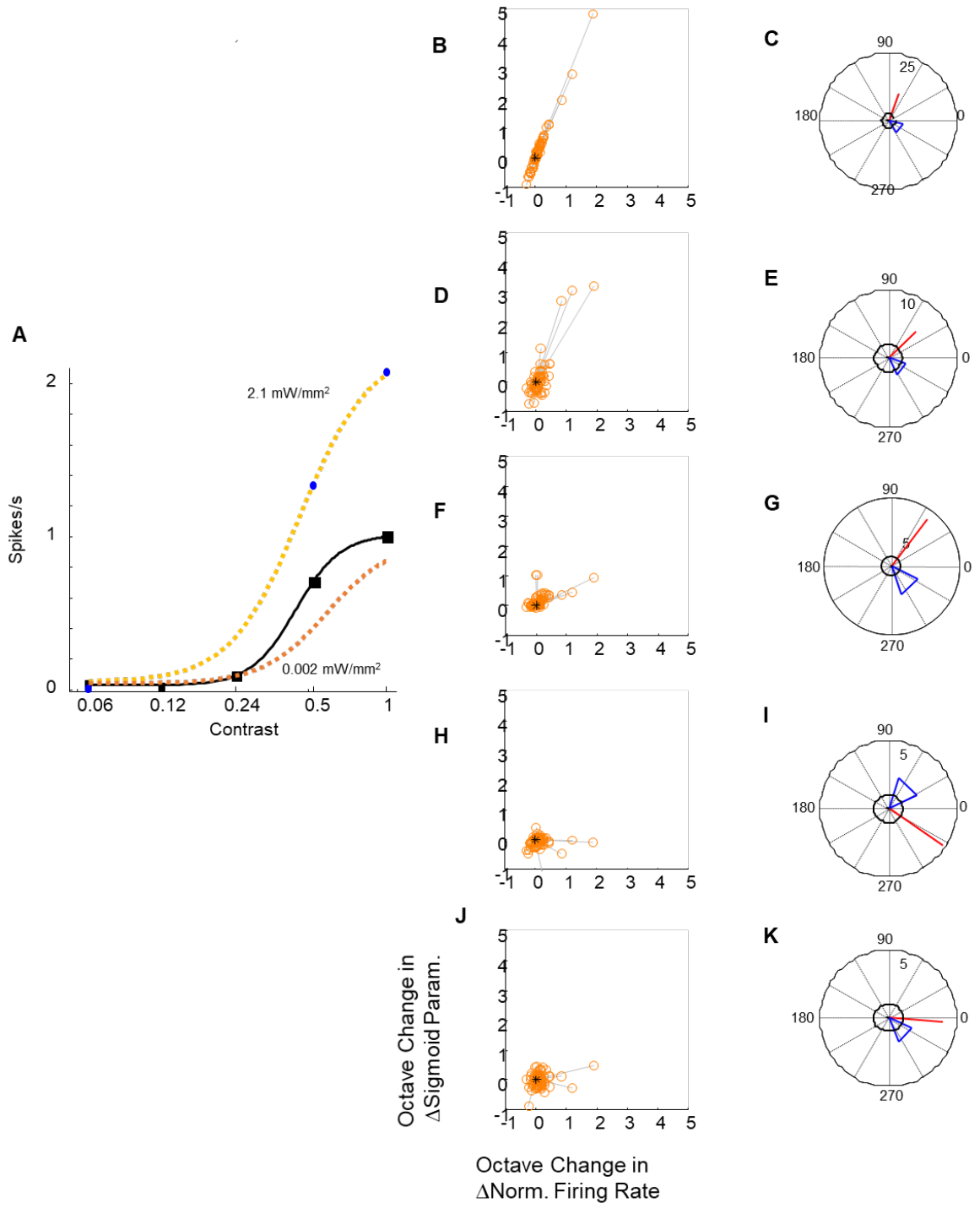
Figure 22: Effects of two levels of photostimulation of VIP+ INs on a single Pyr cell. (A) Example CRF from a cell stimulated at two different photostimulation intensities. Format is identical to figure 11, photostimulation intensities inset. Middle column, B-J: Scatterplots showing the octave changes in firing rate (x-axis) and parameter change (y-axis) for AUC, R_{Max}, R_{Min}, c_{50} and log Slope, respectively. Data is normalized to the dimmer photostimulation intensity, indicated by the asterisk. Far left column, C-K: Polar plots showing the vector sum from the adjacent scatter plot. Black circles and blue triangles indicate percentile cutoffs as described in the text.
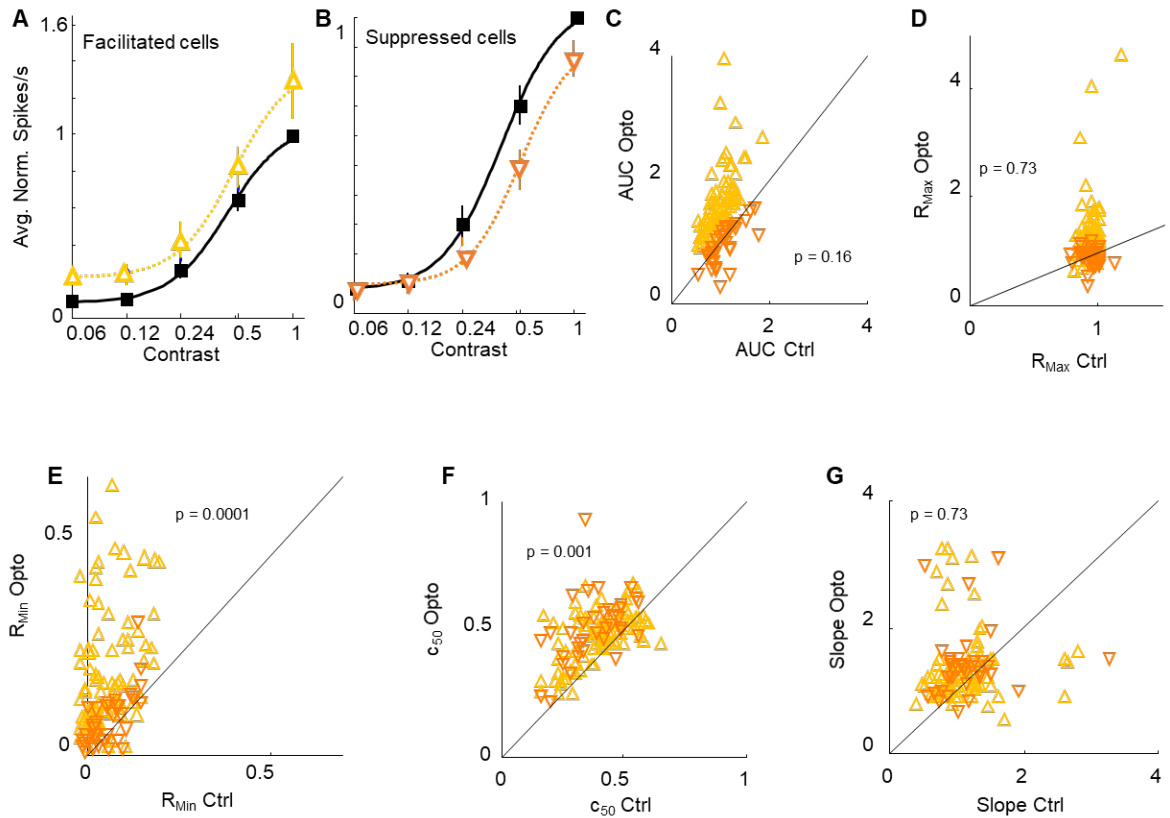
Figure 23: Effects of VIP+ IN photostimulation on CRF parameters. Average normalized CRFs from Pyr cells recorded from during VIP+ IN activation that caused facilitation, with photostimulation data shown as upward oriented yellow triangles (A) and suppression, with photostimulation data shown as downward oriented orange triangles (B). Format is identical to Figure 19. (C-G) Scatterplots comparing sigmoid parameters between Control (x-axis) and Opto (y-axis) curves; C-G plots show AUC, R_{Max}, R_{Min}, c_{50} and log slope, respectively, with color and shape of data points corresponding to Opto data points in A and B, indicating whether the cell was facilitated or suppressed. P-values are inset.

Table 4: Control and Opto means from sigmoid parameters, and corresponding main effect (Opto*Adapt) p-values from a one-way, quantifying how VIP+ INs affect Pyr cell responses to contrast.

Parameter	Ctrl Mean ± 95% C.I.	Opto Mean ± 95% C.I.	p-value
AUC	1.26 ± 0.08	1.26 ± 0.16	$F_{(1,121)} = 2.84$, p $= 0.16$
R_{Max}	0.94 ± 0.02	0.8 ± 0.08	$F_{(1,121)} = 0.25$, p $= 0.73$
R_{Min}	0.08 ± 0.017	0.18 ± 0.05	$F_{(1,121)} = 19.53$, p $= 0.0001$
c50	0.36 ± 0.038	0.43 ± 0.05	$F_{(1,121)} = 19.11$, p $= 0.0001$
log Slope	1.17 ± 0.19	1.28 ± 0.2	$F_{(1,121)} = 0.12$, p $= 0.73$

Table 5: Interaction p-values quantifying whether VIP+ INs affect Pyr cell responses to contrast differently whether the neuron was suppressed or facilitated.

Parameter	Interaction p-value
AUC	$F_{(1,121)} = 47.81$, p $= 3.33 \cdot 10^{-9}$
R_{Max}	$F_{(1,121)} = 12.26$, p $= 0.0018$
R_{Min}	$F_{(1,121)} = 18.86$, p $= 0.0001$
c50	$F_{(1,121)} = 11.68$, p $= 0.002$
log Slope	$F_{(1,121)} = 0.84$, p $= 0.56$

Like the other two INs we examined, we did not find a correlation between photostimulation intensity and Pyr activity change, and indeed observed both facilitation and suppression for both dim and bright LED photostimulation, so used percent activity change as our measure of the effect of VIP+ IN stimulation on sigmoid parameters (Figure 24A, $r^2 = 0.009$, $p = 0.3$). To determine whether the magnitude of activity change caused by VIP+ IN activation was correlated with changes in sigmoid parameters, we plotted the change in sigmoid parameters against the amount of Pyr cell activity change. Based on previous work and the current model circuit for INs, we expected Pyr cell responses to only be facilitated and were surprised by the amount of suppression we observed. From our sample of 123 cells, 87 were facilitated and 36 were suppressed. On average we facilitated Pyr activity by 17% with a range of 0.7-114% and suppressed

activity by 9.25% with a range of (-0.3%) to (-32%). Not surprisingly, because CRF parameter values change in opposite directions for cells that are facilitated compared to cells that are suppressed, we observed strongly correlated activity-dependent shifts in CRFs for AUC, R_{Max} and R_{Min}: AUC $r^2 = 0.99$, $p = 2.14 \cdot 10^{-123}$ (Figure 24B), R_{Max} $r^2 = 0.72$, $p = 6.78 \cdot 10^{-35}$ (Figure 24C), R_{Min} $r^2 = 0.59$, $p = 3.54 \cdot 10^{-25}$ (Figure 24D). For log Slope, we observed a mild, but significant, correlation (Figure 24F, $r^2 = 0.034$, $p = 0.041$), and c_{50} was not correlated with VIP+ IN induced Pyr cell activity change (Figure 24E, $r^2 = 0.0006$, $p = 0.79$). Figure 25C shows ΔR_{Max} vs. ΔR_{Min}, and there was no main effect ($F_{(1,121)} = 0.62$, $p = 0.6$), but there was a significant interaction ($F_{(1,121)} = 5.9$, $p = 0.034$). Most of the facilitated data points in Figure 24C indicate that their CRFs had larger drops in R_{Max} than R_{Min}, whereas the suppressed data points are much closer to the line of equality, suggesting VIP+ photostimulation might induce divisive facilitation and subtractive suppression in Pyr cells. This is further explored below.

After determining that VIP+ IN activation proportionally influenced Pyr cell sigmoid changes in our sample of cells photostimulated at one photointensity, we quantified whether these changes were divisive or subtractive. Figure 25A-B show two example CRFs, one that was facilitated (Figure 25A) and one that was suppressed (Figure 25B). Identical to sections 3.1.1 and 3.1.2, divisive shifts are shown with longer, purple dashes and subtractive shifts are shown with shorter, green dashes. The facilitated CRF shift in Figure 25A shows a cell that increased by similar amounts across all contrasts, characteristic of subtractive shifts. The suppressed cell in Figure 25B shows clear divisive inhibition. We then looked at whether VIP+ INs were more likely to induce divisive or subtractive changes by using the same measures described in section 3.1.1 and 3.1.2. We then compared SS_{Res} from the two models, but found no main effect of VIP+ IN activation ($F_{(1,121)} = 0.21$, $p = 0.73$) or interaction between facilitated and suppressed cells ($F_{(1,121)} = 0.84$, $p = 0.14$). This is somewhat surprising by looking at the scatterplot in Figure 25C, because all the suppressed neurons show a smaller divisive SS_{res}, but the interaction was likely cancelled out by the wide range of SS_{Res} values from facilitated cells. Overall, even though the optogenetic effect in most cells was better described by the divisive model, there was not enough difference between the two models' residuals to suggest that VIP+ INs are more likely to induce one type of inhibition over the other.

This is possibly because VIP+ IN activation has a relatively small effect on Pyr cell activity compared to PV+ and Sst+ IN activation. Indeed, while stimulating VIP+ INs we were often using our maximum LED intensity and saw only moderate changes in Pyr cell spike rate, whereas when we stimulated PV+ INs with our maximum LED intensity in King et al. (2016), V1 was completely silenced.

Lastly, we wanted to determine whether the type of shift caused by VIP+ IN activation was correlated with the amount of Pyr cell suppression. Figure 25D shows the octave shifts for the F-Stat for our subset of cells recorded from at two LED irradiances, and it appears that most neurons' F-statistic increases with Pyr cell suppression, suggesting that more suppression causes more divisive scaling, and our permutation analyses indicate that the change in magnitude of the F-statistic could not have occurred by chance, but the change in the angle of the vector sum could have (Figure 25E). Figure 25F shows the changes in F-Stat plotted against change in Pyr cell activity. As with Sst+ IN activation, VIP+ IN activation was not significantly correlated with the type of CRF shift, regardless of whether we looked at facilitated or suppressed Pyr cells. R and p-values for the combined facilitated and suppressed data set are inset. As with our Sst+ dataset, there is a discrepancy between our subsample of cells that were stimulated at two different LED intensities and our dataset with cells that were only stimulated at one intensity. VIP+ INs did not have a consistent impact on Pyr cell activity, so perhaps collecting more data with cells stimulated at two intensities would resolve these findings.

Overall, VIP+ IN activation can both decrease and increase Pyr cell contrast sensitivity. We also show that the magnitude of CRF shifts are proportional to how much VIP+ IN activation affects Pyr cell firing rate, although photostimulation intensity was not correlated with whether VIP+ INs caused facilitation or suppression. Additionally, we also demonstrated that resultant CRF changes are just as likely to be divisive as subtractive.
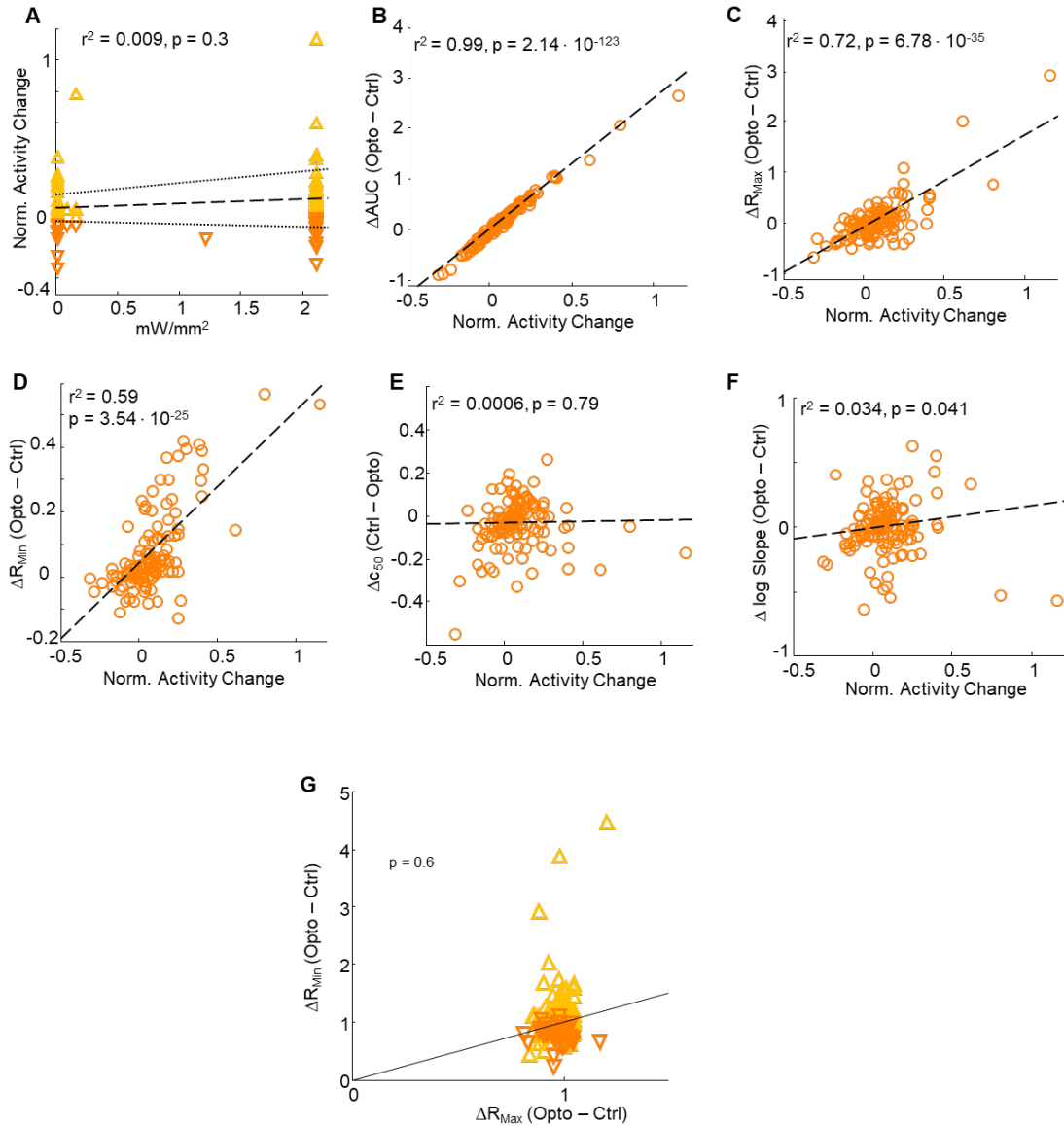
Figure 24. Effects of VIP+ IN-induced activity changes on CRF parameters. (A) Correlation of surface LED brightness (x-axis) with Pyr cell activity change (y-axis). (B-F) Correlation of Pyr cell activity change (x-axis) with change CRF parameters (y-axis) for AUC, RMax, RMin, c50 and log slope, respectively. Positive and negative values on the x-axis represent facilitation and inhibition of Pyr cell activity, respectively, and positive and negative values on the y-axis represent rightward/upward and leftward/downward sigmoid changes, respectively. Long dashed line represents the regression line, and shorted dashed lines represent 95% confidence intervals. R^2 and p-values are inset. (G) Comparison of changes in R_{Max} and R_{Min} as a result of photostimulation.
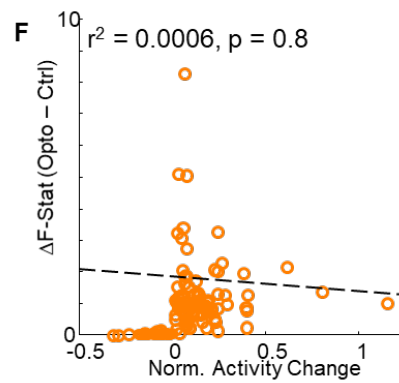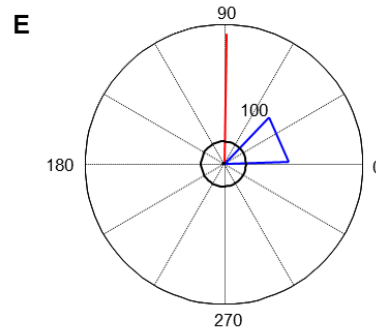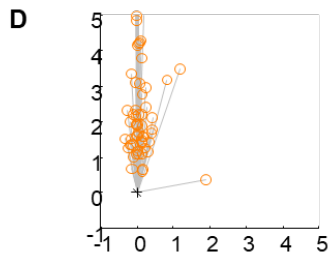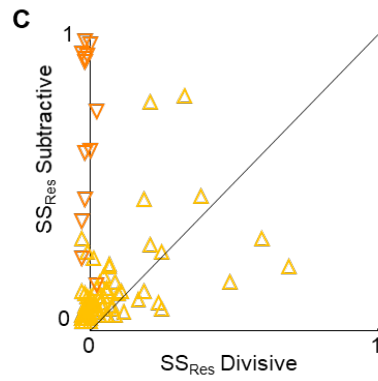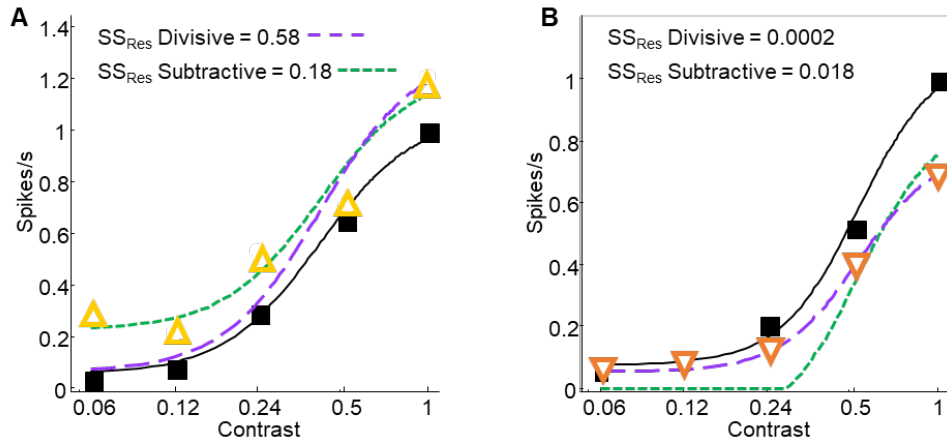
Figure 25. Quantifying Sst+ IN-induced divisive vs. subtractive inhibition. (A&B) CRFs from two example cells, one that demonstrated divisive scaling (A) and one that experienced a subtractive shift (B). Color and format are identical to figure 11, except the Opto curve has been exchanged for the divisive (purple dashed curve) and subtractive (green dashed curve) models. SSRes for both models are inset. (C) A scatterplot comparing SS_{Res} from the divisive model (x-axis) and the subtractive model (y-axis) for all cells. P-value inset. (D) Octave shifts in Firing Rate (x-axis) and F-statistic (y-axis) for the subset of cells stimulated at two photostimulation intensities. Data is normalized to the dimmer photointensity. (E) A polar plot showing the vector sum for octave shifts and the percentile cutoffs for the radius and angle. Figure format is identical to figure 17. (F) Correlation of Pyr cell suppression (x-axis) with change in the F-statistic (y-axis). Format identical to Figure 21.

3.5 COMPARISONS BETWEEN IN SUBTYPES

Finally, it is important to consider whether the magnitude of IN-induced CRF shifts vary between IN subtypes. We focused on changes in AUC, R_{Max}, R_{Min}, and c_{50} because these are the parameters that were most consistently affected by photostimulation. We plotted the changes in these parameters as scatter columns, with the data from Pyr cell CRFs divided into four groups based on perturbation: (1) PV+ INs, (2) Sst+ INs, (3) VIP+ INs that caused facilitation and (4) VIP+ INs that caused suppression. The color and shape for each group is identical to those from their respective sections. We ran one-way ANOVAs for each parameter, followed by Bonferroni post-hoc tests to determine whether cell types differed from one other. Figures 26A-D show changes in parameters for AUC, R_{Max}, R_{Min}, and c_{50}, respectively. For AUC (Figure 26A) and R_{Max} (Figure 26B), we observed identical patterns of significant parameter changes between IN subtypes: photostimulation of PV+ INs and Sst+ INs both caused significantly larger decreases than VIP+ INs that caused suppression, and VIP+ INs that caused facilitation caused significantly larger increases than all other IN groups; this is sensible based on how AUC and R_{Max} change depending on if Pyr cell activity is facilitated or suppressed (p-values in Tables 6 & 7). VIP+ INs that caused facilitation significantly increased R_{Min} compared to the three IN groups that caused suppression (Figure 26C, p-values in Table 8). And finally, for c_{50}, we observed significant increases as a result of VIP+ IN photostimulation (both facilitated and suppressed) compared to Sst+ IN photostimulation, but PV+ IN-induced changes were not significantly different from any IN subgroup (p-values in Table 9). It is not surprising that for all four parameters there were differences between VIP+ facilitation and the three inhibitory groups because parameters shift in opposite directions. Also, because there were no differences between PV+ and Sst+ induced CRF parameter changes, this suggests that these two classes of INs similarly modulate Pyr cell sensitivity to contrast.

Figure 27 is a diagram that outlines potential functionality of the three primary IN subtypes based on our findings in this chapter. PV+ INs provided significantly more divisive scaling, suggesting that their primary role is modulating cortical activity levels. Sst+ INs provided roughly equal amounts of divisive and subtractive inhibition, which suggests that they are involved in both controlling activity levels and in tuning neural

preferences to visual stimuli. Finally, VIP+ INs both facilitated and suppressed Pyr cell activity, and provided both divisive and subtractive gain control, which suggests that they have three roles in the cortex: (1) propagating information between Pyr cells, (2) moderate gain control, because they provided much less inhibition than PV+ and Sst+ INs, and (3) tuning neural responses to visual stimuli due to the subtractive gain control they provided.
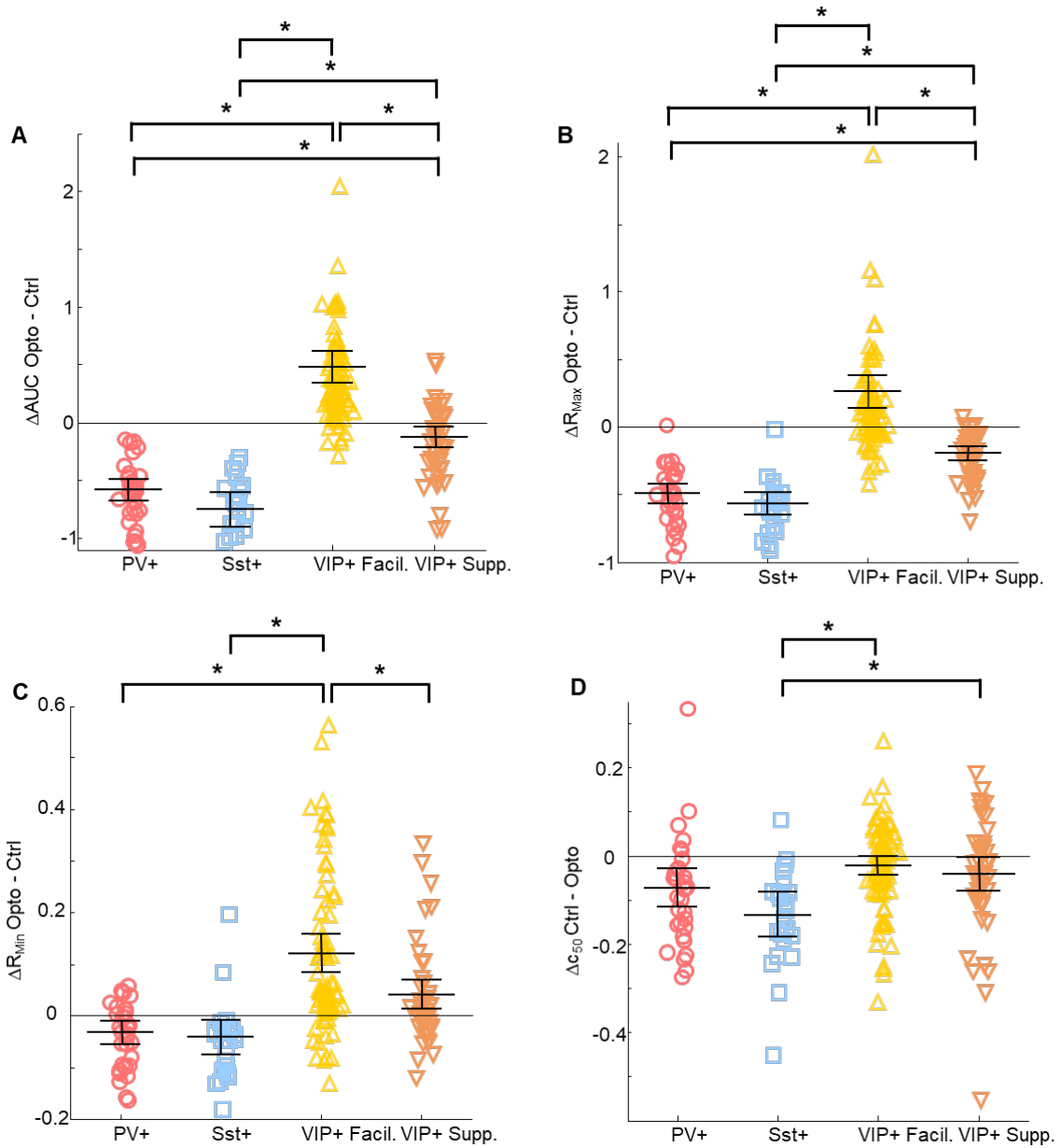
Figure 26. Comparison of photostimulation effects on CRF parameters between IN subtypes. (A-D) Scatter columns comparing IN-induced CRF parameter changes for AUC, RMax, RMin and c50, respectively. Data is divided into PV+, Sst+, and VIP+ IN subgroups, with VIP+ INs being further divided into facilitated and inhibited Pyr cell responses. Colors of each group correspond to their scatterplots in previous figures. Error bars are 95% CIs, with the middle horizontal line representing the mean change. Brackets and asterisks above the columns represent Bonferroni post-hoc comparisons following a one-way ANOVA.

Table 6: P-values comparing changes in AUC between IN subtypes.

Cell Type		p-value
PV+	Sst+	0.577
	VIP+ Facil.	4.53E-13
	VIP+ Supp.	0.00034
Sst+	PV+	0.577
	VIP+ Facil.	4.53E-13
	VIP+ Supp.	0.00007
VIP+ Facil.	PV+	4.53E-13
	Sst+	4.53E-13
	VIP+ Supp.	4.02E-10
VIP+ Supp.	PV+	0.00034
	Sst+	0.00007
	VIP+ Facil.	4.02E-10

Table 7: P-values comparing changes in R_{Max} between IN subtypes.

Cell Type		p-value
PV+	Sst+	0.912
	VIP+ Facil.	4.56E-13
	VIP+ Supp.	0.008
Sst+	PV+	0.912
	VIP+ Facil.	4.93E-13
	VIP+ Supp.	0.003
VIP+ Facil.	PV+	4.56E-13
	Sst+	4.93E-13
	VIP+ Supp.	2.23E-08
VIP+ Supp.	PV+	0.008
	Sst+	0.003
	VIP+ Facil.	2.23E-08

Table 8: P-values comparing changes in R_{Min} between IN subtypes.

Cell Type		p-value
PV+	Sst+	0.994
	VIP+ Facil.	0.000000199
	VIP+ Supp.	0.063
Sst+	PV+	0.994
	VIP+ Facil.	0.000002
	VIP+ Supp.	0.65
VIP+ Facil.	PV+	0.000000199
	Sst+	0.000002
	VIP+ Supp.	0.004
VIP+ Supp.	PV+	0.063
	Sst+	0.065
	VIP+ Facil.	0.004

Table 9: P-values comparing changes in c_{50} IN subtypes.

Cell Type		p-value
PV+	Sst+	0.23
	VIP+ Facil.	0.15
	VIP+ Supp.	0.624
Sst+	PV+	0.23
	VIP+ Facil.	0.0005
	VIP+ Supp.	0.01
VIP+ Facil.	PV+	0.15
	Sst+	0.0005
	VIP+ Supp.	0.795
VIP+ Supp.	PV+	0.624
	Sst+	0.01
	VIP+ Supp.	0.795
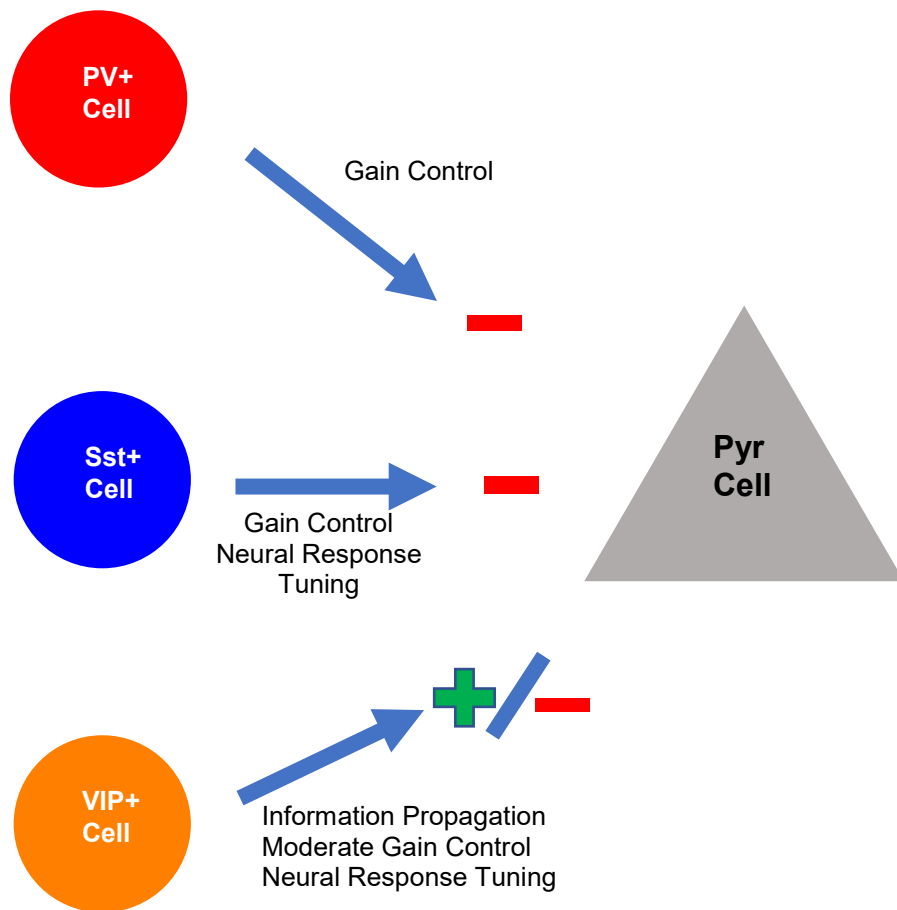
Figure 27: A diagram outlining the functions of PV+, Sst+ and VIP+ INs based on our findings from Chapter 3. Green plus signs and red subtraction signs indicate whether the IN provides facilitation or suppression to Pyr cells, respectively.

CHAPTER 4: THE EFFECT OF INTERNEURON ACTIVATION ON ADAPTED CRFs

4.1 HIGHLIGHTS

- Our lab has previously examined the role of different brain regions in contrast adaptation by optogenetically silenced V1 during the adaptation period by simultaneous activation of all IN subtypes. We found evidence that the adapted LGN signal that arrives at V1 is divisively scaled via local network effects during contrast adaptation.

- The current work shifts focus to examining the potential roles of individual IN subtypes in this local network by employing the same experimental paradigm but optogenetically activating the three primary IN subtypes individually.

- It appears that in mouse V1, PV+ have the greatest impact on modulating Pyr cell responses to contrast whereas Sst+ INs have a minor role, although they are both involved in modulating response gain control.

- VIP+ INs have a separate role because they only increased responses to low contrasts, an effect that has not previously been reported.

Previously, our lab investigated the role of different brain regions in contrast adaptation by silencing V1 during the adaptation period by optogenetically activating all IN subtypes. We found evidence that adapted LGN input is divisively scaled via local network effects in V1 during contrast adaptation (King et al., 2016). In that study we also determined that contrast adaptation is a primarily activity-dependent phenomena, and that silencing V1 during the adaptation period decreased the magnitude of adaptation. However, in this study cortical silencing was brought about by simultaneously activating all IN subtypes, and we therefore could not parse apart individual IN contributions, or determine whether V1 silencing affected local cell processes due to the lack of excitation or the increase in inhibition provided by photostimulated INs. The current study used identical visual stimuli and photostimulation protocols to King et al. (2016), but we individually targeted the three primary IN subtypes and only partially suppressed V1 activity because we wanted to preserve the secondary effects of IN photoactivation (see section 1.6.2.2). Our aim was to determine if amplifying different types of inhibition

during the adaptation period (i.e. divisive and somatic (PV+, Atallah et al., 2012; Pfeffer et al., 2013; Fino and Yuste, 2011) vs. subtractive and dendritic (Sst+, Wilson et al., 2012; Pfeffer et al., 2013; Wang et al., 2004) would produce different constellations of adaptive changes. We also examined the effects of VIP+ IN activation. According to recent models of V1 interneuron circuits, VIP+ INs predominantly synapse on Sst+ INs and increase Pyr cell activity by disinhibition (Pfeffer et al., 2013; Karnani et al., 2016). Therefore, if local V1 adaptation mechanisms are activity-dependent we expected VIP+ activation to cause an increase in adaptation magnitude compared to the decrease in magnitude we observed while activating all IN subtypes. Identical to chapter 3, this results chapter is divided into four sections: one section for each IN subtype, and then a fourth section comparing the findings between subtypes.

4.2 THE EFFECTS OF PV+ INS ON CONTRAST ADAPTATION

We recorded from 85 putative Pyr cells in 15 mice during a contrast adaption protocol while simultaneously stimulating Pvb+ INs, and 55 met our inclusion criteria (see section 2.5.3). Electrophysiological recording depth was not correlated with photostimulation-induced changes for any parameter so we did not segregate recordings by cortical layer. Figures 28A,C,D show CRFs from three example cells in our sample, demonstrating the range of effects we observed as a result of PV+ IN activation during the adapt period. Figure 28B shows spike density functions (SDFs) for the Control Adapt (black line) and Opto Adapt (red line) conditions at full contrast (top panel) and 0.04 contrast (bottom panel) for the cell in Figure 28A. Black data points indicate the Control Nonadapt condition. The empty and filled arrows on the right of the CRFs in Figure 28 indicate the average spike rate during the adapt period for Control Adapt and Opto Adapt conditions, respectively. For the cells in Figure 28A,C&D, photostimulation of PV+ INs produced similar relative decreases in spike rates (also see Figure 30).The two adapt conditions are most pertinent because this study was designed to examine the effects of IN activation on CRFs after contrast adaptation, therefore the relevant "control condition" for all analyses examining the effects of photostimulation is the Control Adapt curve. Overall, based on the responses of the three cells shown in Figure 28 it appears that PV+ IN activation
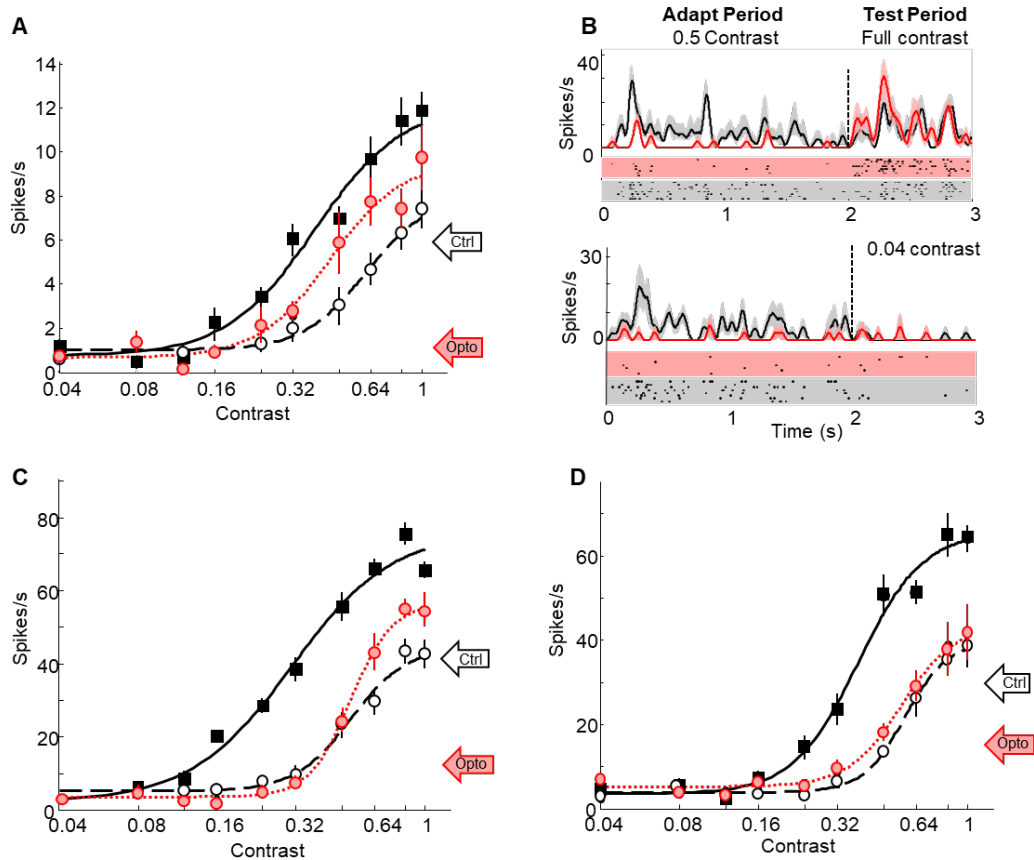
Figure 28: Example CRFs showing the effects of PV+ IN photostimulation on contrast adaptation. (A,C&D) CRFs from three example cells, with contrast displayed on the x-axis and spike rate on the y-axis. Control Nonadapt and Control Adapt responses are shown as solid black and empty circles, respectively. Opto Adapt responses are shown as filled red circles. Curves represent the best fit of a Naka-Rushton function to the Control Nonadapt (black solid), Control Adapt (black dashed) and Opto Adapt (red dashed) data. Arrows to the right of the CRFs represent the average spike rate during the Control Adapt (white arrow) and Opto adapt (red arrow) period. All error bars represent SEM. (B) SDFs and rasters for the cell in A during both the adapt and test periods. The dashed vertical line represents when the adapt period ended and the test period started. The black trace is the Control Adapt response, and the red trace is the Opto Adapt response, with spike rasters of corresponding colors underneath. The desatured shadows behind the traces represent SEM error bars. The top trace is the neuron's response during the full contrast test trial, and the bottom trace is the neuron's response at 0.04 contrast.

primarily caused moderate increases in the maximum response to contrast with no change to the minimum response (Figure 28A&C), or essentially no change to any contrast responses (Figure 28D). In Figure 28B, the first 2s of the SDFs represent the 2s adapt period when the cell was presented a drifting 0.5 contrast grating, and the last second represents the 1s test grating that was a drifting grating at one of 10 different contrasts (outlined in section 2.4.1 The neuron in Figure 28A/B show was highly suppressed during the adapt period, and the first 2s of the SDFs (Figure 26B). For the full contrast test grating (Figure 26B top; 2 - 3s), the SDFs show that the Opto Adapted condition had a greater response than the Control Adapted condition, but at 0.04 contrast there was essentially no difference in responses between the Control and Opto Adapt conditions (Figure 28B bottom; 2 - 3s). As in Chapter 3, the sigmoid fits to the CRFs allow quantitative analysis of changes in adaptation as a result of IN activation. For Figures 28A, C, and D the solid black lines indicate fits to Control Nonadapted data, dashed black lines indicate fits to Control Adapted data, and doted red lines indicate fits to Opto Adapted data.

Even though we were primarily interested in differences between the two adapt conditions, our stimulus protocol included four conditions: (1) Control Nonadapt, (2) Control Adapt, (3) Opto Nonadapt and (4) Opto Adapt (described in section 2.4.2); this was to ensure that our photostimulation paradigm did not have any unintended physiological effects on the post adaption period. In King et al. (2016), we demonstrated that simultaneously photostimulating all GABAergic INs subtypes had no effect on Nonadapted responses, which indicated that photostimulation was not causing any sort of unrelated rebound effects that would have contaminated our measures of adaptation. Therefore, in the current study we compared our two Nonadapted curves to ensure that an optogenetic rebound effect was not occurring from activating only PV+ INs. Figure 29A shows the average, normalized responses for all four conditions: Control Nonadapted, Control Adapted and Opto Adapted are in the same format as Figure 28, and the Opto Nonadapted CRF is shown as solid red data points with a solid red line indicating the fit. All data is normalized to the Control Nonadapt Condition. Figure 29B shows the normalized differences between in the four sigmoid parameters from the two Nonadapted
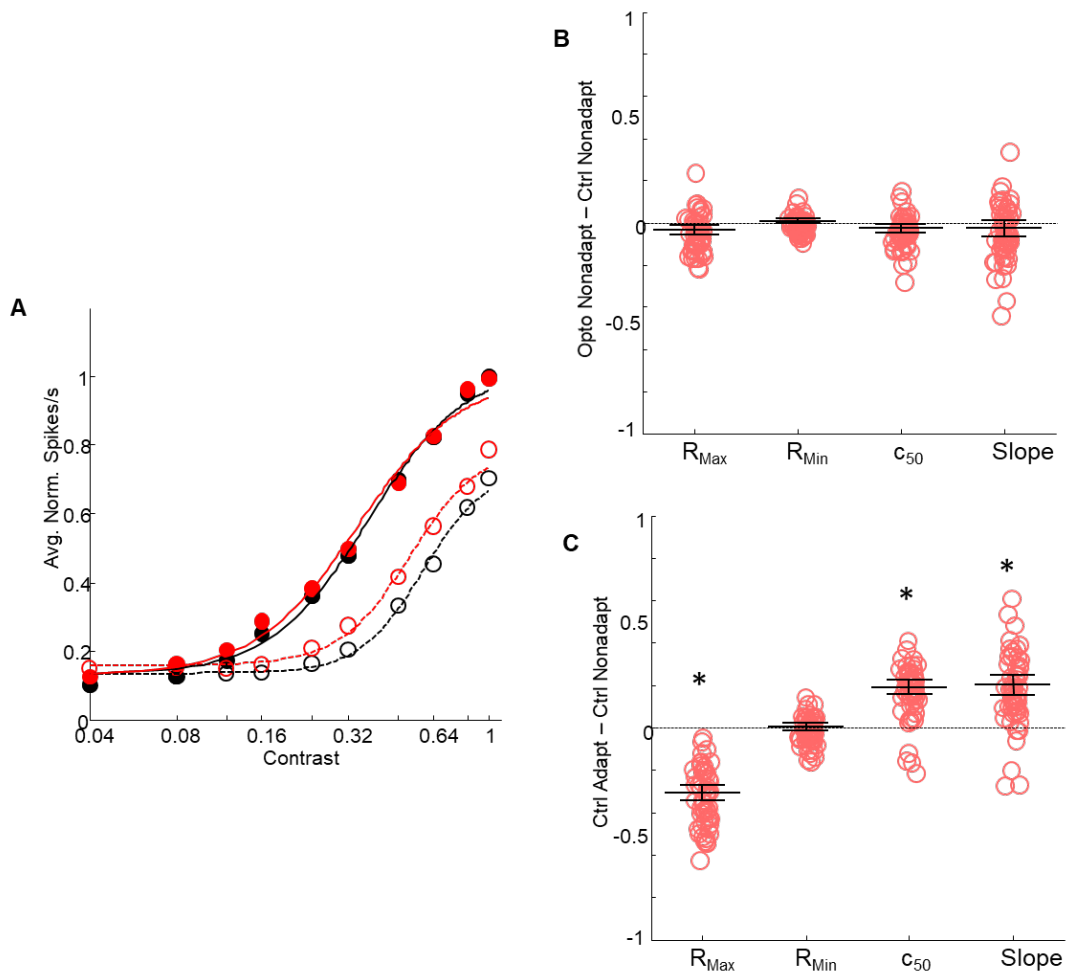
Figure 29: Effects of photostimulation on PV-Cre-Ai32 mice. (A) Average normalized CRFs for Ctrl Nonadapt, Ctrl Adapt, photostimulated Nonadapt and photostimulated Adapt. Format is the same as Figure 26, with the phototsimulated Nonadapt condition being shown as solid red circles with a solid red curve. (B) Scatter columns comparing sigmoid fit parameters between Control Nonadapt and Opto Nonadapt conditions. There were no significant differences. (C) Scatter columns comparing CRF fit parameters between Control Nonadapt and Control Adapt conditions. We observed changes that were consistent with previous reports.

curves. It is obvious based on both the average normalized CRFs (Figure 29A) and the scatter columns (Figure 29B) that there is no substantial difference between these two Nonadapt curves. A statistical analysis did not support a difference for any of the parameters (p-values in Table 5, paired t-tests). Figure 29 also highlights the difference between the Control Nonadapt and Control Adapt conditions, which indicates the contrast adaptation we measured without photostimulation was comparable to previous studies in mouse V1 (e.g. LeDue et al., 2013; King et al., 2015). We observed a rightward and downward shift in CRFs as a result of adaptation (Figure 29A), and the scatter columns (Figure 29C) indicate normal contrast adaptation was associated with significant decreases in R_{Max} and significant increases in c_{50} and log Slope (p-values in Table 10, paired t-tests). These findings align with previous studies and confirmed that our adaptation protocol was adequate to compare to other work in the field (LeDue et al., 2013; King et al., 2015; King et al., 2016).

Once we were confident that photostimulation alone was not creating any artifacts in the post-photostimulation period and that our adaptation protocol was acceptable, we started examining the differences between our two adapt conditions using parameters from the sigmoidal fits to the CRFs. For the following comparisons we ran two-way ANOVAs to statistically quantify the effects of PV+ photostimulation. Our two independent variables were adaptation (Nonadapt and Adapt) and photostimulation (Control and Opto), and we were primarily interested in the photostimulation*adapt interaction, which quantified whether optogenetically activating PV+ INs during the adapt period significantly altered how Pyr cells adapted to contrast. Figures 30A-E are scatter plots comparing parameters from Control Adapt and Opto Adapt CRF sigmoid fits. AUC was a holistic measure of the CRF shape calculated from the data points (see methods section 2.5.1) , wheras R_{Max}, R_{Min}, c_{50} and log slope were extracted from sigmoid fits to the two adapted curves. After stimulating PV+ INs during adaptation, we observed significant interactions between photostimulation and adaptation that produced increases in AUC and R_{Max} (Figure 30A&B, respectively. AUC mean change: 2.5, p = 0.001; R_{Max} mean change: 0.07, p = 0.002), but no other parameters were significantly altered (R_{Min} mean change: 0.03, p = 0.17; c_{50} mean change: -0.035, p = 0.62; and log Slope mean change: -0.02, p = 0.08; Figures 30C-E, respectively).
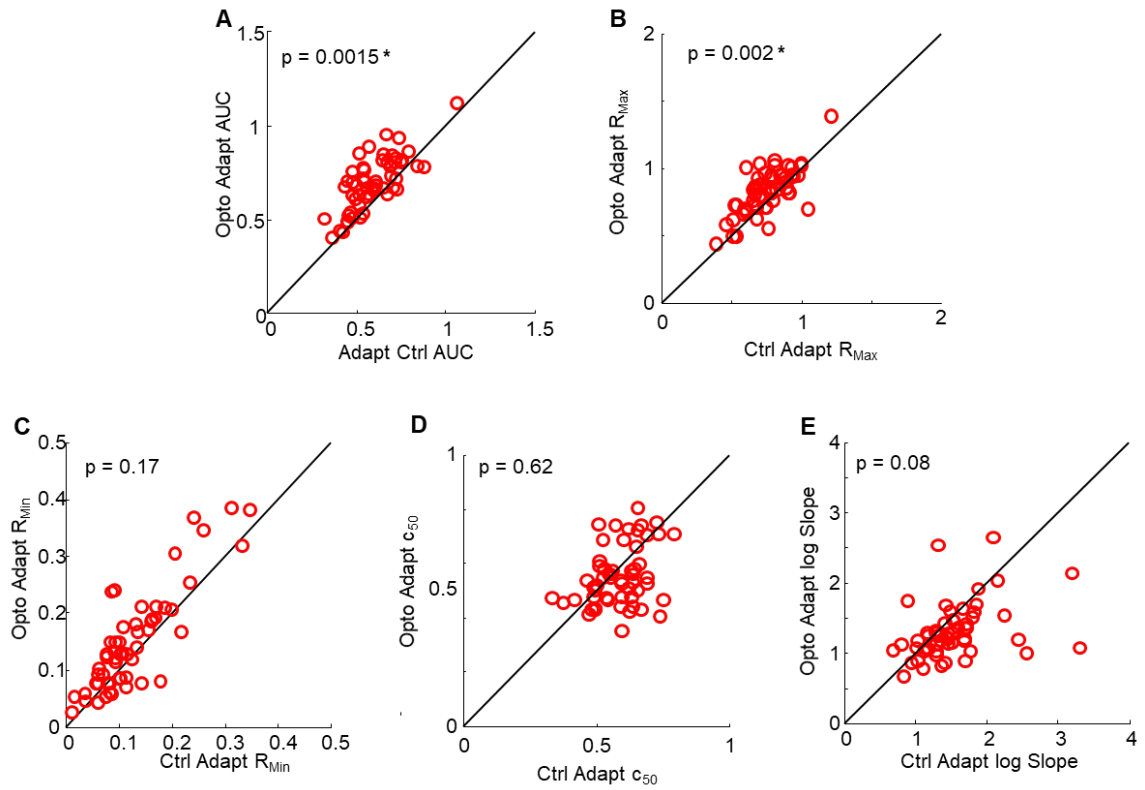
Figure 30: Effects of PV+ IN photostimulation on adapted sigmoid fit parameters. (A-E) Scatterplots comparing sigmoid parameters between Ctrl Adapted (x-axis) and Opto Adapted (y-axis) curves; A-E plots show AUC, R_{Max}, R_{Min}, c_{50} and log slope, respectively. P-values are inset.

After determining that PV+ IN activation had only a subtle effect on CRFs, we wanted to see whether the magnitude of pyramidal cell suppression during the adapt period was correlated with CRF parameter changes because we observed in King et al. (2016) that 99% of contrast adaptation in mouse V1 could be accounted for by activity-dependent mechanisms. Therefore, we expected larger decreases in Pyr cell activity during the adapt period to cause larger parameter changes. We calculated photostimulation induced activity changes by normalizing the mean responses from the adapt period for both conditions to the control response at full contrast, and subtracted the normalized control response from the normalized Opto response such that negative values indicated suppression and positive values indicated facilitation (see eqn 11; Figure 31A top inset).

$$Norm.\,Activity\,Change = \left(\frac{Opto\,Adapt\,Firing\,Rate}{Max\,Nonadapt\,Firing\,Rate} - \frac{Opto\,Adapt\,Firing\,Rate}{Max\,Nonadapt\,Firing\,Rate} \right) * 100 \qquad (11)$$

In our sample of Pyr neurons, PV+ photostimulation decreased activity during the 2s adaptation period by 32.7% on average, with a range of (-10%) to (-67%). Figure 31A shows an example cell demonstrating how we calculated pyramidal cell activity change during the adapt period as a result of PV+ IN activation, and Figures 31B-F show AUC and sigmoid fit parameter changes (see section 2.5.2) plotted against Pyr cell activity change. We observed a significant correlation of weak to moderate strength with activity change for only AUC and c_{50} (Figures 31B&E, respectively, r values inset), but not for any other fit parameters (Figures 31C,D,F, R_{Max}, R_{Min} and log Slope, respectively, r values inset). The discordant observations between AUC and R_{Max} were surprising because these two values are often modulated similarly due to the majority of AUC being composed by the higher spike rates. However, this difference could be explained by the moderate, though not statistically significant, increase PV+ IN activation had on R_{Min} (Figure 30C), which could add variability to the magnitude of R_{Max} increases; because R_{Max} represents the maximum firing rate above the R_{Min} baseline, if the firing rate increased at both low and high contrasts there would be no increase in R_{Max}. Conversely, AUC values are only mildly affected by responses to low contrast.
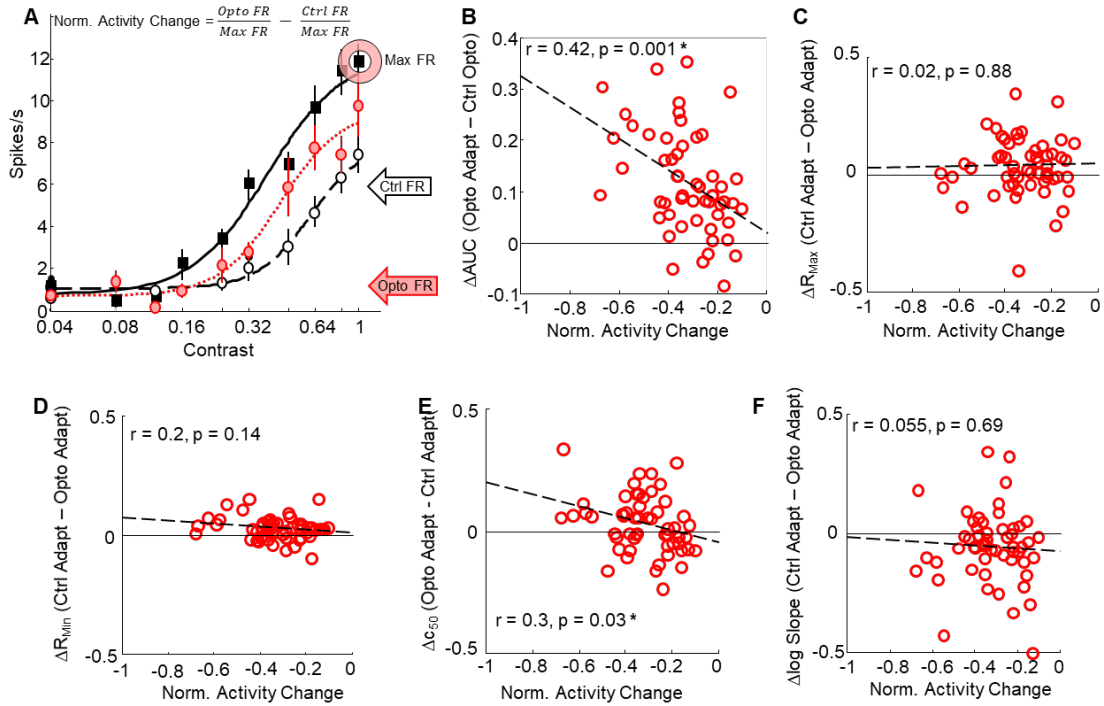
Figure 31: Effects of PV+ IN-induced suppression on adapted CRF parameters. (A) CRFs from an example cell showing how we calculated photostimulation-induced activity changes. Format is the same as Figure 26. (B-F) Correlation of Pyr cell suppression (x-axis) with change in adapted CRF parameters (y-axis) for AUC, R_{Max}, R_{Min}, c_{50} and log Slope, respectively. Long dashed line represents the regression line. R and p-values are inset.

4.3 THE EFFECTS OF SST+ INS ON CONTRAST ADAPTATION

We recorded from 54 putative Pyr cells in 13 mice during a contrast adaption protocol while simultaneously stimulating Sst+ INs, and 35 met our inclusion criteria (see section 2.5.3). As with PV+ IN activation, depth was not correlated with any photostimulation-induced parameter changes so we did not segregate recordings by cortical layer. Figures 32A-C show three example cells from our sample, demonstrating the range of effects we observed as a result of Sst+ IN activation, and Figure 32D shows SDFs demonstrating how photostimulation affected the response of the cell in 32C during the adaption period. Figure format for the following section is identical to that in Figures 29-31 except that we have used blue to represent Sst+ photostimulation. The three example cells show mild to nonexistent effects of Sst+ photostimulation on contrast adaptation in mouse V1. The response to maximum contrast was only slightly elevated in all three cells, and responses to lower contrasts were slightly increased in the cell in Figure 32C. The decrease in firing rate during the adapt period for the cell is Figure 30C is shown in the first 2s of the SDFs, and the slight increase in test responses for both full (top panel) and 0.04 contrast (bottom panel) is shown in the last 1s (Figure 32D).

The logic behind the analyses in Figures 33-35 is identical to that of Figures 29-31, therefore for brevity I will not repeat the motivation and background underlying each analysis from section 4.1.

First we determined that photostimulation of Sst+ INs was not having any unexpected physiological effects. Figure 33A shows the average, normalized responses for all four of our conditions, and Figures 33B&C highlight the differences between the two Nonadapted curves and the two Control curves, respectively. We did not observe any significant differences between our two Nonadapted curves (Figure 33B, p-values in Table 11, paired t-tests), and our Control curves demonstrated the expected parameter changes caused by adaptation (Figure 31C, p-values in Table 11, paired t-tests).

Next, we looked at the effects of photostimulating Sst+ INs during the adapt period on CRF fit parameters. For our sample of Pyr cells recorded from during Sst+ stimulation, we decreased activity by 35.7% on average, with a range of (-74%) to (-2.4%). Figures 34A-E show scatter plots comparing Control Adapt and Opto Adapt CRF parameters with statistical comparisons using the same ANOVA configuration as the previous

Figure 32: Example CRFs showing the effects of Sst+ IN photostimulation on contrast adaptation. (A-C) CRFs from three example cells, with contrast on the x-axis and spike rate on the y-axis. Control Nonadapt and Control Adapt responses are shown as solid black and empty circles, respectively. Opto Adapt responses are shown as empty blue circles. Curves represent the best fit of a Naka-Rushton function to the Control Nonadapt (black solid), Control Adapt (black dashed) and Opto Adapt (blue dashed) data. Arrows to the right of the CRFs represent the average spike rate during the Control Adapt (white arrow) and Opto adapt (blue arrow) period. All error bars represent SEM. (D) SDFs and rasters for the cell in C during both the adapt and test periods. The dashed vertical line represents when the adapt period ended and the test period started. The black trace is the Control Adapt response, and the blue trace is the Opto Adapt response, with spike rasters of corresponding colors underneath. The desaturated shadows behind the traces represent SEM error bars. The top trace is the neuron's response during the 0.04 contrast test trial, and the bottom trace is the neuron's response at full contrast.

section, and we were again primarily interested in the photostimulation*adapt interaction. When stimulating Sst+ INs during adaptation, we observed a significant interaction for only R_{Max} (Figure 34B, mean change = 0.08, p = 0.03), but no other parameters were significantly altered (AUC mean change = 1.2, p = 0.88; R_{Min} mean change = 0.03, p = 0.85; c_{50} mean change = 0.018, p = 0.19; and log Slope mean change = 0.37, p = 0.16; Figures 34A,D-F, respectively). This pattern of changes is not surprising because the two adapted CRFs in Figure 31A were very similar. However, it was unexpected that AUC did not show significant decreases along with R_{Max}, but when looking at the scatter plots it appears that although roughly the same number of cells showed increases in AUC (Figure 34A) and R_{Max} (Figure 34B) as a result of photostimulation, AUC data points are closer to the line of equality indicating a smaller magnitude changes.

Next we determined whether the magnitude of Pyr cell suppression was correlated with sigmoid parameter changes. Figure 35A shows an example cell demonstrating how we calculated Pyr cell activity change during the adapt period in the same format as Figure 31A, and Figures 33B-F show sigmoid parameter changes plotted against Pyramidal cell activity change in the same format as Figure 31B-F. We observed no correlation between changes in any sigmoid parameters and activity change (all p-values and r-values are inset), indicating the modest changes Sst+ activation had on Pyr adaptation did not appear to depend on the magnitude of Pyr suppression.

4.4 THE EFFECTS OF VIP+ INS ON CONTRAST ADAPTATION

We recorded from 135 putative Pyr cells in 17 mice during a contrast adaption protocol while simultaneously stimulating VIP+ INs, and 70 met our inclusion criteria (see section 2.5.3). Depth was not correlated with the effects of photostimulation-induced changes for any CRF parameters so we did not segregate recordings by cortical layer. Figures 36A&C show CRFs from two example cells from our sample, and Figures 36B&D show SDFs which correspond to the cells in Figures 36A&C, respectively. Figure format is identical to that in sections 4.2 and 4.3 but in this section orange indicates VIP+ photostimulation. As first reported in Chapter 3, we found that VIP+ activation caused some Pyr neurons to be suppressed during the adapt period but others to be facilitated. Moreover, we predicted that if V1 adaptation is based on an activity-dependent mechanism suppression during the
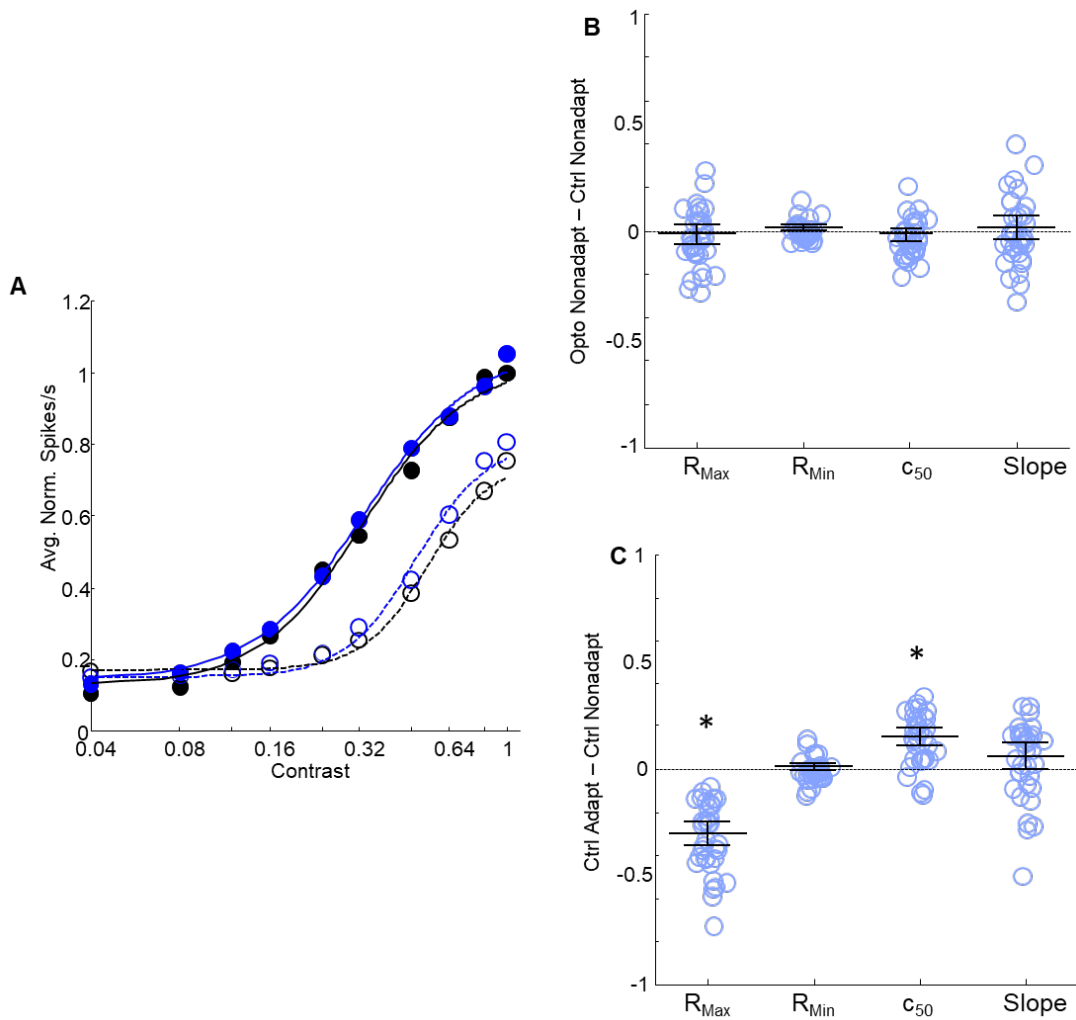
Figure 33: Effects of photostimulation on Sst-Cre-Ai32 mice. (A) Average normalized CRFs for all four conditions. Format is the same as Figure 30, with the Opto Nonadapt condition being shown as solid blue circles with a solid blue curve. (B) Scatter columns comparing CRF fit parameters between Control Nonadapt and Opto Nonadapt conditions. There were no significant differences. (C) Scatter columns comparing sigmoid fit parameters between Control Nonadapt and Control Adapt conditions. We observed changes that are consistent with previous reports.

Figure 34: Effects of Sst+ IN photostimulation on adapted CRF parameters. (A-E) Scatterplots comparing CRF parameters between Adapted (x-axis) and Opto Adapted (y-axis) curves; A-E plots show AUC, R_{Max}, R_{Min}, c_{50} and log slope, respectively. P-values are inset.
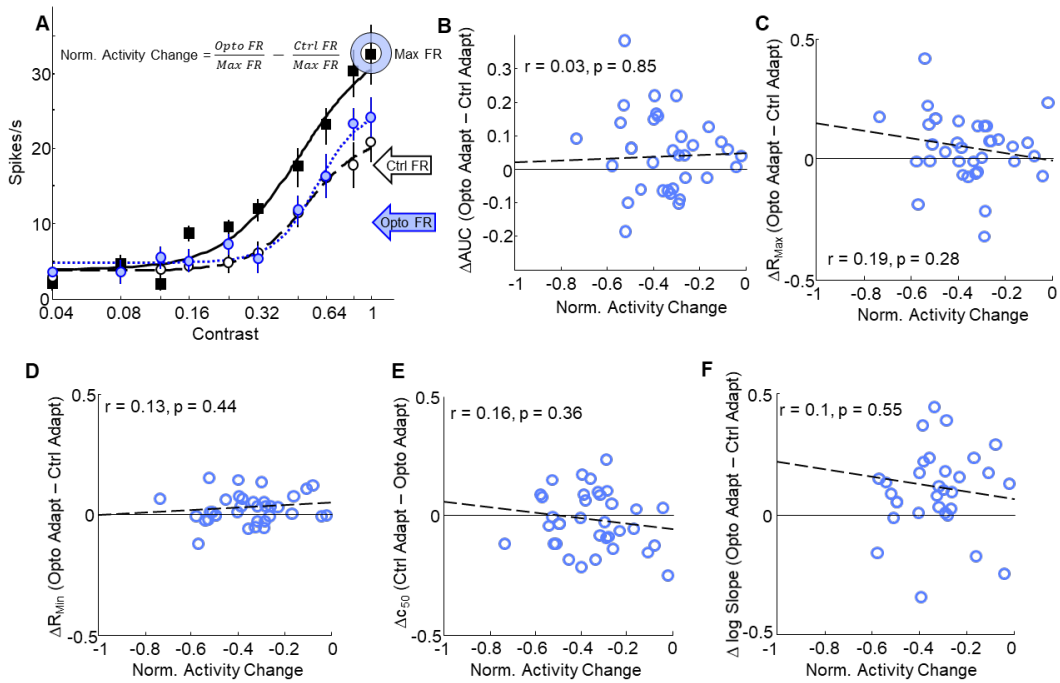
Figure 35: Effects of Sst+ IN-induced suppression on adapted CRF parameters. (A) CRFs from an example cell showing how we calculated photostimulation-induced activity changes. Format is the same as Figure 30. (B-F) Correlation of Pyr cell suppression (x-axis) with change in adapted CRF parameters (y-axis) for AUC, R_{Max}, R_{Min}, c_{50} and log slope, respectively. Long dashed line represents the regression line. R and p-values are inset.
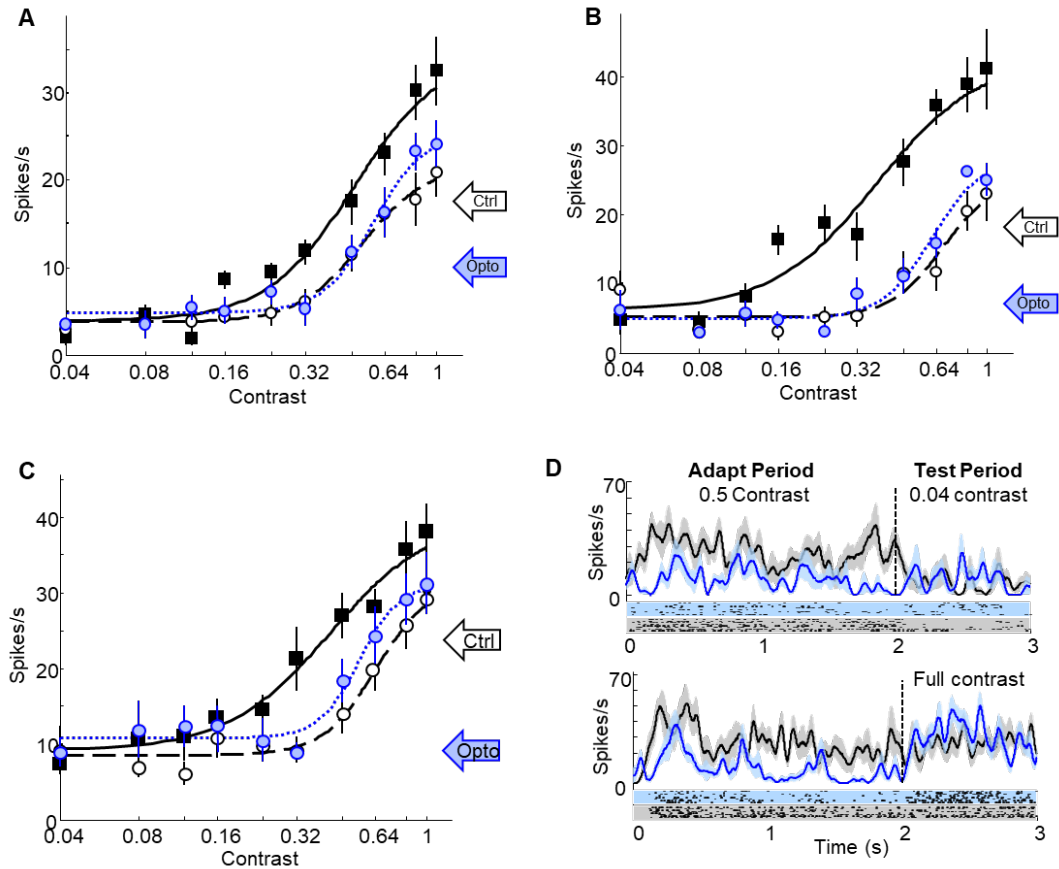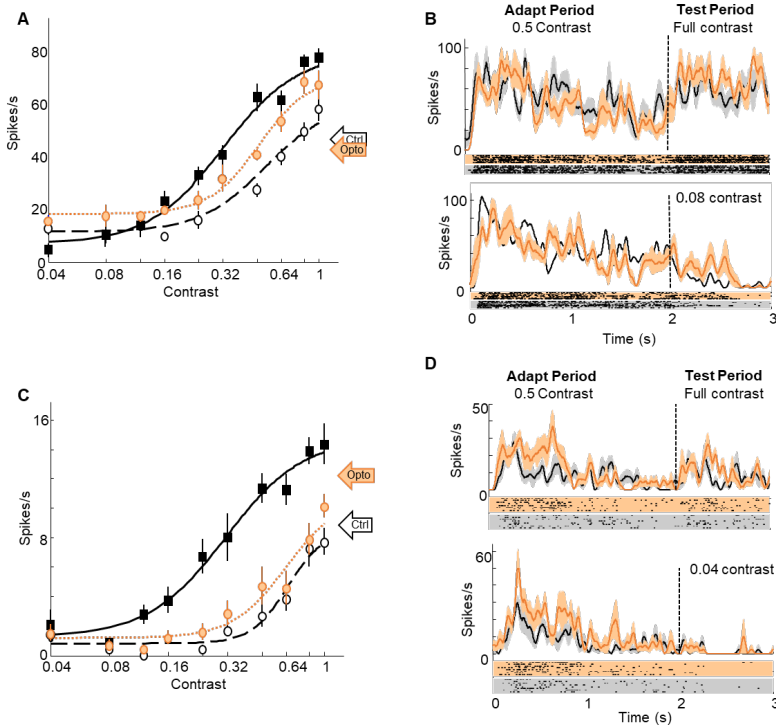
Figure 36: Example CRFs showing the effects of VIP+ IN photostimulation on contrast adaptation. (A&C) CRFs from two example cells, with contrast on the x-axis and spike rate on the y-axis. Control Nonadapt and Control Adapt responses are shown as solid black and empty circles, respectively. Opto Adapt responses are shown as empty orange circles. Curves represent the best fit of a Naka-Rushton function to the Control Nonadapt (black solid), Control Adapt (black dashed) and Opto Adapt (orange dashed) data. Arrows to the right of the CRFs represent the average spike rate during the Control Adapt (white arrow) and Opto adapt (orange arrow) period. It can be seen that the cell in A was suppressed in the Opto Adapt condition whereas the cell in C was facilitated. All error bars represent SEM. (B&D) SDFs and rasters for the cells in A&C, respectively, during both the adapt and test periods. The dashed vertical line represents when the adapt period ended and the test period started. The black trace is the Control Adapt response, and the orange trace is the Opto Adapt response, with spike rasters of corresponding colors underneath. The desatured shadows behind the traces represent SEM error bars. The top traces are the neuron's response during the full contrast test trial, and the bottom trace is the neuron's response at 0.08 (B) and 0.04 contrast (D).
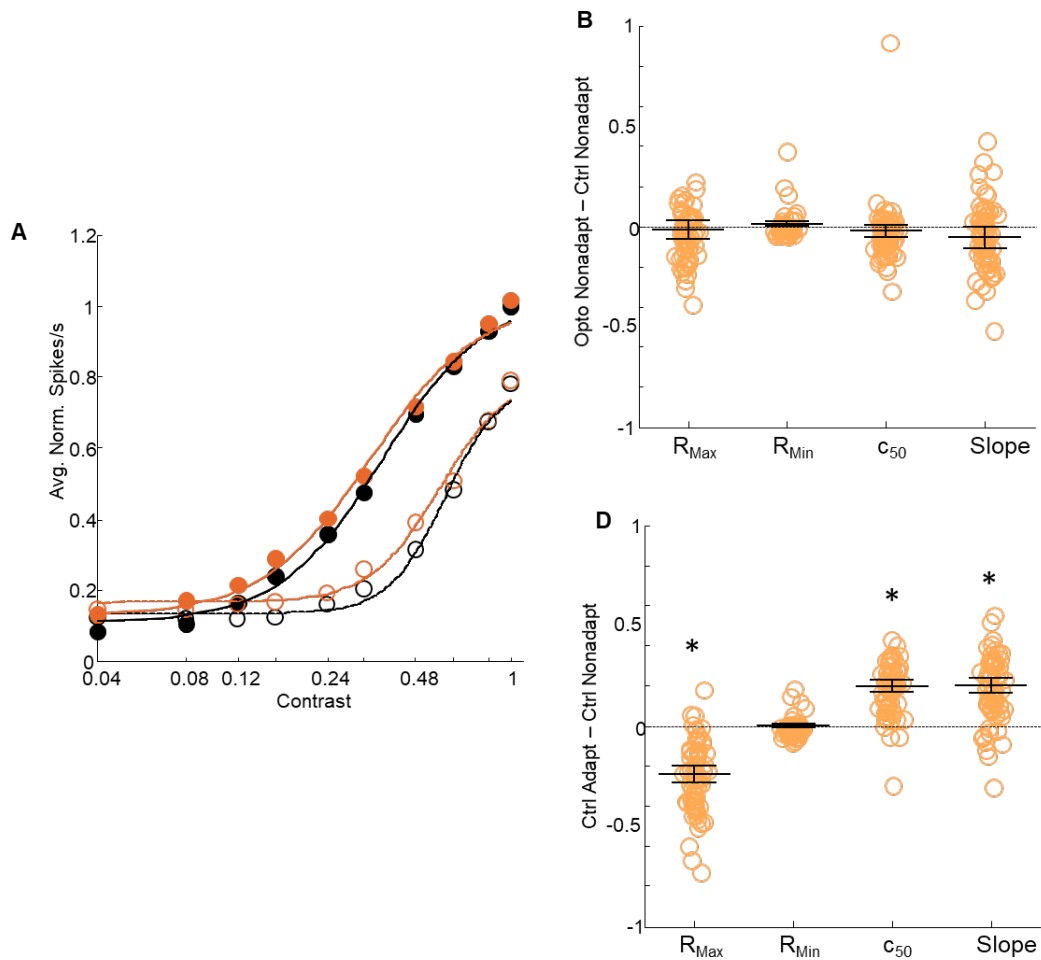
Figure 37: Effects of photostimulation on VIP-Cre-Ai32 mice. (A) Average normalized CRFs for all four conditions. Format is the same as Figure X, with the Opto Nonadapt condition being shown as solid orange circles with a solid orange curve. (B) Scatter columns comparing CRF fit parameters between Control Nonadapt and Opto Nonadapt conditions. There were no significant differences. (C) Scatter columns comparing CRF fit parameters between Control Nonadapt and Control Adapt conditions. We observed changes that are consistent with previous reports.

adapt period should reduce contrast adaptation, but facilitation during the adapt period should enhance contrast adaptation. The suppressed Pyr cell in Figure 36A shows a decrease in adaptation magnitude across all contrasts, with a notable increase in responses to low contrasts. The corresponding SDF in Figure 36B shows the slight decrease in firing rate during the adapt period, and the increases in test responses at full and 0.08 contrast (top and bottom panels, respectively). The facilitated cell in figure 36C shows a slight decrease in the magnitude of adaptation, with the largest effect at higher contrasts. The SDF for this facilitated cell (Figure 36D) shows the increase in firing rate during the adapt period followed by a slight increase in response at full contrast (top panel) and essentially no difference in response at 0.04 contrast (bottom panel).

The logic behind the analyses in Figures 37-39 is identical to previous sections, therefore for brevity I will not repeat the motivation and background underlying each analysis from sections 4.1 and 4.2.

As with PV+ and Sst+ photostimulation, we first wanted to ensure that activating VIP+ INs did not cause any physiological rebound effects. Because we hypothesized that VIP+ IN photostimulation would cause Pyr cell facilitation, we expected any potential rebound effect to be a decrease in activity, which is the opposite of how a rebound effect caused by PV+ and Sst+ IN-induced suppression would manifest. Figure 37A shows the average, normalized responses for all four of our conditions, and figures 37B&C highlight the differences between the two Nonadapted curves and the two Control curves, respectively. We did not observe any significant differences between our two Nonadapted curves (Figure 37B, p-values in Table 7, paired t-tests), and our Control curves demonstrated the standard parameter changes expected to arise from contrast adaptation (Figure 37D, p-values in Table 12, paired t-tests).

Next, we looked at the effects of photostimulating VIP+ INs during the adapt period on sigmoid fit parameters. For our sample of Pyr cells recorded from during VIP+ stimulation, we added a between factor to our ANOVA to determine any interaction between facilitated and suppressed cells. An interaction between cells that were facilitated and cells that were suppressed would indicate that the cells were adapting differently; we expected interactions because previous findings indicate that contrast adaptation is mediated by firing rate dependent mechanisms (King et al., 2016), and we
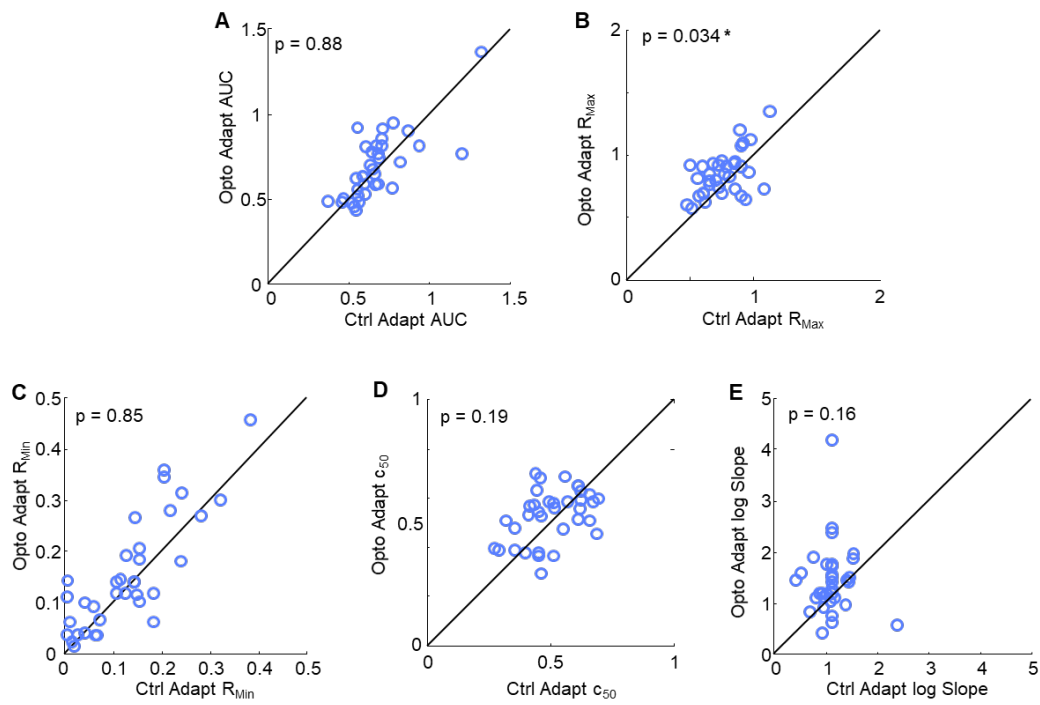
106
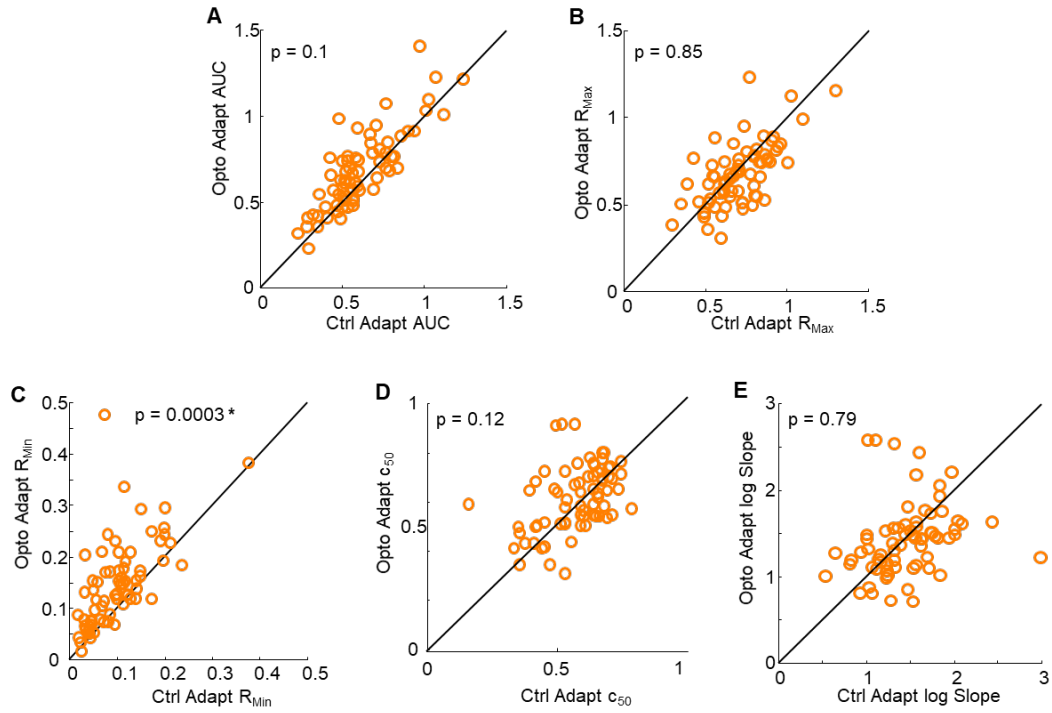
Figure 38: Effects of VIP+ IN photostimulation on adapted CRF parameters. (A-E) Scatterplots comparing CRF parameters between Adapted (x-axis) and Opto Adapted (y-axis) curves; A-E plots show AUC, R_{Max}, R_{Min}, c_{50} and log Slope, respectively. P-values are inset.

hypothesized that when VIP+ IN activation caused an increase in Pyr cell firing we would observe an increase in the magnitude of adaptation. However, we found that adaptation magnitude never increased, and that there were no suppression/facilitation interactions for any CRF parameters (p-values in Table 13); therefore we have not differentially labeled facilitated and suppressed data points in the following figures. Figures 36A-E show scatter plots comparing Control Adapt and Opto Adapt sigmoid fit parameters. When stimulating VIP+ INs during adaptation, we observed significant interactions between photostimulation and adaptation for only R_{Min} (Figure 38D, mean change = 3.03, p = 0.00003), no other parameters were significantly altered (AUC mean change = 0.06, p = 0.1; R_{Max} mean change = -1.15, p = 0.85; c_{50} mean change = 0.02, p = 0.12; and log Slope mean change = 0.03, p = 0.79; Figures 36B,C,E,F, respectively). This pattern of changes broadly agrees with the averaged normalized curve in Figure 37A, which also indicated the only difference between adapted curves was the increase in the response to minimum contrasts.

Next we directly tested our activity-dependent adaptation hypothesis from King et al. (2016): that larger decreases in Pyr cell activity during the adapt period cause larger changes to CRF fit parameters. For VIP+ IN photostimulation, we predicted that facilitation of Pyr cell activity would cause an increase in the magnitude of CRF adaptation, whereas VIP+ IN-induced suppression would decrease CRF adaptation. Figure 39A shows an example cell demonstrating how we calculated Pyr cell activity change. Overall, activity was increased on average by 2.56% as a result of optogenetic photostimulation, with a range of -35 to 37%. Pyr cells that were inhibited were suppressed on average by -8.9% with a range of (-0.015%) to (-35%), and cells that were disinhibited were facilitated on average by 12.2% with a range of 0.04 to 37%. Figures 39B-F show AUC and sigmoid fit parameter changes plotted against Pyr cell activity change. Unlike the plots in the previous sections, the x-axis on Figures 39B-F have positive and negative values to account for the facilitation and suppression we observed, respectively. We have shown facilitated Pyr cell correlations as solid regression lines, and dashed lines represent suppressed Pyr cell correlations. There were no correlations between activity and parameter changes for facilitated Pyr cells, but suppressed cells had moderate correlations for changes in AUC (Figure 39B) and c_{50} Figure 39D). The
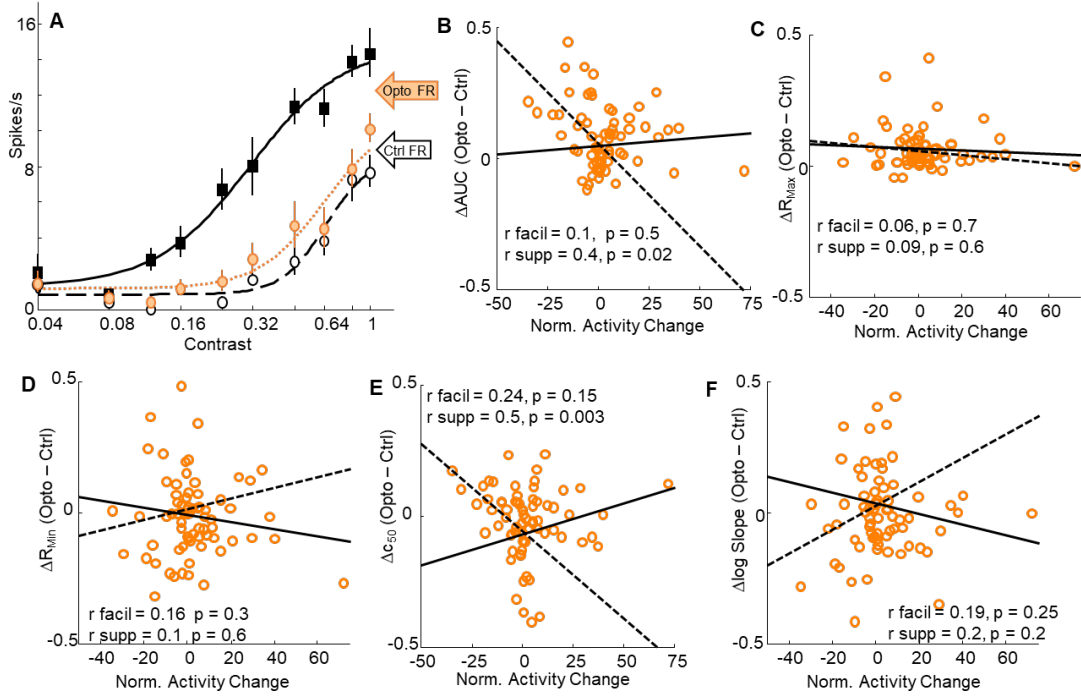
Figure 39: Effects of VIP+ IN-induced activity change on adapted CRF parameters. (A) CRFs from an example cell showing how we calculated photostimulation-induced activity changes. Format is the same as Figure 34. (B-F) Correlation of Pyr cell suppression (x-axis) with change in adapted sigmoid fit parameters (y-axis) for AUC, R_{Max}, R_{Min}, c_{50} and log Slope, respectively. Solid line represents the facilitated regression line, and shorted dashed lines represents suppressed regression line. R and p-values are inset.

differences in AUC and R_{Max} are not surprising because of the VIP+ IN-induced increase in R_{Min} (Figure 37C) – an increase in response to low contrast increases AUC, but an increase to R_{Min} value decreases R_{Max} because R_{Max} is the maximum response to contrast *above* R_{Min}, not simply the maximum response to contrast (see section 2.5.1).

4.5 COMPARISONS BETWEEN IN SUBTYPES

The final set of analyses examined whether photostimulation altered the magnitude of adaptation of the IN subtypes by different amounts. We focused on changes in AUC, R_{Max}, and R_{Min} because these parameters were most consistently affected by photostimulation. Changes in AUC (Figure 38A), Rmax (Figure 40B), and Rmin (Figure 40C) are plotted as scatter columns to compare altered Pyr cell adaptation when PV+ (red), Sst+ (blue) and VIP+ (orange) INs were activated. The color and shape for each group is identical to those from their respective sections. We ran one-way ANOVAs for each parameter, followed by Bonferroni post-hoc tests on significant ANOVAs to determine whether activating different IN subtypes changed fit parameters in unique ways. PV+ IN photostimulation caused significant increases to AUC compared to Sst+ INs (Figure 38A, p = 0.0018), and VIP+ IN activation caused significantly larger increases to R_{Min} than PV+ IN photostimulation (Figure 40C, p = 0.004). In conclusion, adaptation was similarly modulated by different IN subgroups, with the only major differences being that PV+ INs significantly attenuated the amount of adaptation-induced AUC decreases, and VIP+ INs significantly increase responses to low contrast compared to PV+ INs. All p-values are in table 14.
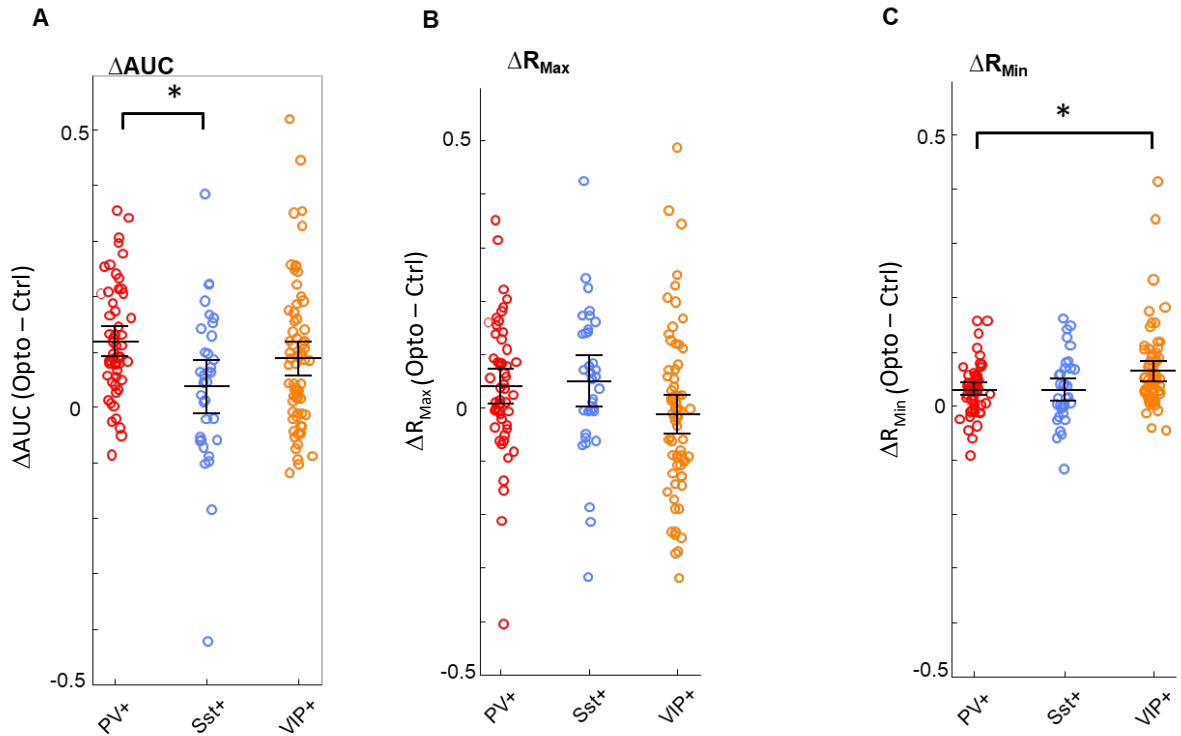
Figure 40: Comparison of photostimulation effects on adapted CRF parameters between IN subtypes. (A-C) Scatter columns comparing IN-induced CRF parameter changes for AUC, R_{Max}, and R_{Min}, respectively. Data is divided into PV+, Sst+, and VIP+ IN subgroups. Colors of each group correspond to their scatterplots in previous figures. Error bars are 95% CIs, with the middle horizontal line representing the mean change. Brackets and asterisks above the columns represent Bonferroni corrections from a one-way ANOVA.

Table 10: P-values comparing PV+ IN Control and Opto Nonadapt and Control Nonadapt and Adapt

Condition	Parameter	p-value (critical p = 0.01)
Control Nonadapt	R_{Max}	0.03
vs	R_{Min}	0.12
Opto Nonadapt	c_{50}	0.011
	log Slope	0.17
Control Nonadapt	R_{Max}	4.62E-13
vs	R_{Min}	0.1
Control Adapt	c_{50}	7.25E-16
	log Slope	4.38E-10

Table 11: P-values comparing Sst+ IN Control and Opto Nonadapt and Control Nonadapt and Adapt

Condition	Parameter	p-value
Control Nonadapt	R_{Max}	0.11
vs	R_{Min}	0.052
Opto Nonadapt	c_{50}	0.25
	log Slope	0.6
Control Nonadapt	R_{Max}	7.65E-09
vs	R_{Min}	0.42
Control Adapt	c_{50}	1.43E-08
	log Slope	0.037

Table 12: P-values comparing VIP+ IN Control and Opto Nonadapt and Control Nonadapt and Adapt. Critical p = 0.01.

Condition	Parameter	p-value
Control Nonadapt	R_{Max}	0.28
vs	R_{Min}	0.06
Opto Nonadapt	c_{50}	0.17
	log Slope	0.017
Control Nonadapt	R_{Max}	6.53E-10
vs	R_{Min}	0.8
Control Adapt	c_{50}	4.83E-21
	log Slope	3.6E-14

Table 13: VIP+ IN Opto*Adapt Interaction p-values

Condition	Parameter	p-value
Suppression	R_{Max}	0.47
vs	R_{Min}	0.66
Facilitation	c_{50}	0.79
Interaction	log Slope	0.54

Table 14: P-values comparing parameter changes induced by each IN subtype. Critical p = 0.016.

Cell Comparison	Parameter	p-value
PV+ vs. Sst+	AUC	0.0018
	RMax	0.72
	RMin	0.98
PV+ vs. VIP+	AUC	0.15
	RMax	0.04
	RMin	0.004
Sst+ vs. VIP+	AUC	0.07
	RMax	0.04
	RMin	0.02

CHAPTER 5. DISCUSSION

Mouse V1 activity is modulated by a complex inhibitory circuit, where INs synapse onto both Pyr cells and other INs (Figure 5, Pfeffer et al., 2013; Karnani et al., 2016). Currently, INs are grouped into three subtypes based on molecular markers: PV+, Sst+ and VIP+ INs (see section 5.1). Early evidence suggested that PV+ INs inhibited themselves and Pyr cells, Sst+ INs inhibited all other cell types except themselves, and VIP+ INs selectively inhibited Sst+ INs (Pfeffer et al., 2013). However, more recent studies on this circuit support additional roles: PV+ INs inhibit all cell types, and VIP+ INs also inhibit and weakly excite themselves (Karnani et al., 2016). It was also found that INs within the same group are connected via gap junctions (Karnani et al., 2016).

As our understanding of IN circuity has increased, so has knowledge regarding IN functionality. Initially it was proposed that each IN subtype had its own role in visual processing, and many groups interpreted their findings based on this view. For example, Atallah et al. (2012) found that PV+ INs modulate Pyr cell gain control, and therefore assigned PV+ INs as being responsible for gain control in the V1. However, Wilson et al. (2012) found similar findings for Sst+ INs, and subsequently Lee et al. (2014) determined that INs behave differently under varying photostimulation protocols. Consequently, individual results on this circuit's functionality have become increasingly difficult to interpret, and findings within the field remain conflicted. As such, IN function is poorly understood at the circuit level and much more work needs to be done to describe this crucial neural network.

There are three terms that are used throughout this chapter to describe how INs modulate Pyr cell activity based on our findings: (1) intrinsic effects, which include the activity levels of the Pyr cells we recorded from, and any processes within that cell, (2) extrinsic effects, which are any processes happening outside of the cell we recorded from. These can include LGN input, cortical feedback, and the overall state of the IN network. For the purposes of this discussion, the overall state of the network refers to how the functionality of the circuit is altered by the intensity of inhibition coming from an IN subtype(s), and/or the timing of synaptic communication between cells in the network. Both of these network properties can be modulated by numerous factors, such as anesthesia (Vaiceliunaite et al., 2013). We were not able to isolate sources of modulation

114

for the data in the current projects and have therefore collectively grouped them. The last effect is (3) local network effects, which refers to the activity-dependent contributions to contrast adaptation from V1 we observed in King et al. (2016). In that study we completely silenced V1 during adaptation, thereby removing any local V1 network contributions. Therefore, we can be reasonably confident that any effects we measured in that study were caused by the removal of these local network contributions.

This discussion will be divided into four major sections; the first and second sections will discuss caveats that specifically relate to IN effects on contrast responses and contrast adaptation, respectively, the third section will consider general circuit issues, and the final section will outline potential future work.

5.1 IN SUBTYPES MODULATE CRFS

In the first study within this thesis (Chapter 3), we selectively stimulated the three main IN subtypes under varying levels of photostimulation because previous work has suggested that photostimulation intensity can alter the type of inhibition provided by INs (i.e. divisive or subtractive inhibition; Lee et al., 2014; El-Boustani and Sur, 2014). Additionally, we used various levels of contrast gratings as our visual stimuli to ensure that we obtained a wide range of Pyr cell responses; previous work has primarily used orientation tuning curves to examine how INs affect Pyr cell responses (e.g. Atallah et al., 2012; Ingram et al., 2019), but because mouse V1 is not particularly well tuned to orientation (e.g. King and Crowder, 2018) we reasoned that utilizing contrast as a stimulus would provide us with more "room" to quantify subtle differences between IN types.

PV+ or Sst+ IN activation caused all Pyr cells to be suppressed, aligning with *in vitro* model findings (Pfeffer et al., 2013). We found that PV+ IN-induced changes to CRFs were significantly better described by divisive scaling, which agrees with a majority of previous work (Atallah et al., 2012; Lee et al., 2014; Phillips et al., 2016), but does not agree with Lee et al. (2012). We found that Sst+ IN-induced changes to individual Pyr cell CRFs could be accurately described by the divisive model in about half our sample and by the subtractive model in the other half. We therefore concluded that under our experimental conditions Sst+ activation does not homogenously inhibit Pyr

neurons with either subtractive or divisive inhibition. Previous studies have reported that Sst+ INs induce primarily subtractive (Wilson et al., 2012) or divisive (Lee et al., 2012; Phillips and Hasenstaub, 2016) inhibition, so our findings do not agree with the current literature. However, this could possibly be explained by differences in the optogenetic protocols between studies. For example, El-Boustani and Sur (2014) demonstrated that when Sst+ IN and Pyr cell activation occurred simultaneously, Sst+ INs provided divisive inhibition, but when Sst+ IN activation lagged Pyr cell activity, Sst+ INs induced subtractive inhibition. However, in that study they provided single-optogenetic pulses to Sst+ INs whereas we continuously stimulated Sst+ INs for 1s – perhaps the difference in the length of photostimulation caused the discrepancy in the type of inhibition reportedly caused by Sst+ INs. Indeed, Wilson et al. (2012) simultaneously activated Sst+ INs and Pyr cells and stimulated Sst+ INs for 1s, which matches the current photostimulation protocol, and reported that Sst+ INs provide subtractive inhibition. Therefore, we conclude that Sst+ INs act dynamically, and the type of modulation they provide is dependent on the state of their local circuit.

Another potential reason for conflicting results on Sst+ INs functionality is the heterogeneity within this IN subtype – if the type of inhibition induced by some Sst+ INs is affected by factors such as network activity, while other Sst+ INs always induce the same type of inhibition, than the type of inhibition reportedly caused by Sst+ INs would be strongly affected by sampling practices. For example, we preferentially recorded from Pyr cells that had robust visual responses, but other setups that utilize electrode shanks more evenly sample all Pyr cells. If one type of Sst+ IN is more likely to synapse onto a Pyr cell based on its stimuli preferences, then a setup like ours could obtain a biased measure of the type of inhibition provided by Sst+ INs.

Examining the effects of VIP+ IN activation on Pyr cell CRFs has not been previously investigated. Surprisingly, we found that photostimulation of VIP+ INs caused both Pyr cell facilitation and suppression, which was not predicted based on *in vitro* models (Pfeffer et al., 2013; Karnani et al., 2016), or previous work *in vivo* that has reported only facilitation (Pi et al., 2013; Fu et al., 2014). This general observation is discussed further in section 5.3.1. As with Sst+ INs, we observed both divisive scaling

and subtractive shifts in modulated CRFs, but neither model better described the changes across our sample.

5.2 IN CONTRIBUTIONS TO CONTRAST ADAPTATION

For the second project in this thesis (Chapter 4), we built on a previous study we conducted that examined the role of different brain regions in contrast adaptation by optogenetically silencing V1 during the adaptation period by activating all IN subtypes. We found evidence that the adapted LGN signal that arrives at V1 is divisively scaled via local network effects during contrast adaptation. The current work expanded this by examining potential roles of individual IN subtypes in this local network by utilizing identical experimental paradigms, but we partially suppressed V1 activity by optogenetically activating the three primary IN subtypes individually. We had two main reasons for only partially suppressing V1 activity as opposed to silencing it as we did in King et al. (2016): (1) We wanted to explore whether regulating Pyr cell firing rate divisively via PV+ IN activation (Atallah et al., 2012) vs. subtractively via Sst+ IN photostimulation (Wilson et al., 2012) produced distinct forms of adaptation. When the firing rate is zero (as it was in King et al., 2016) these two forms of inhibition are indistinguishable and therefore silencing would not be useful; (2) In the normally functioning cortical circuit, it seems likely that activating a specific interneuron type will have both primary and secondary effects (see section 1.6.2.2). If the cortex was silenced, these secondary effects may be absent or distorted if the circuit is pushed too far below its normal operating range.

Additionally, we also photostimulated VIP+ INs and expected their activation to cause an increase in adaptation magnitude because these cells have been reported to facilitate Pyr cell responses (Karnani et al 2016; Fu et al 2014; Pi et al 2013).

PV+ IN activation had a larger effect on modulating Pyr cell responses than Sst+ INs (Figure 40). However, this is not surprising because we found that PV+ INs significantly increase AUC and R_{Max} sigmoid parameters whereas Sst+ INs only increased R_{Max}. Perhaps PV+ INs have a larger impact on Pyr cell responses to adaptation because they synapse on Pyr cell somas where action potentials are initiated (Pfeffer et al., 2013; Xu et al., 2010), whereas Sst+ INs synapse on their distal dendrites and have

less of an impact on firing rate (Chiu et al., 2013; Kawaguchi and Kubota, 1997; Wang et al., 2004).

VIP+ IN activation caused both facilitation and suppression, so it was surprising that we did not observe any interactions between CRF changes and Pyr cell modulation because both PV+ and Sst+ IN activation support the hypothesis that adaptation depends on the firing rate of the recorded neuron. The data from our VIP+ IN experiments provides evidence that contrast adaptation is not exclusively regulated by intrinsic Pyr cell activity. Potential reasons for the unexpected effects caused by activating VIP+ INs are discussed below.

5.2.1 VIP+ IN-Induced R_{Min} Increase After Contrast Adaptation

VIP+ IN activation exclusively caused a significant increase in R_{Min} after contrast adaptation, and this increase occurred regardless of whether Pyr cell suppression or facilitation was induced. To our knowledge, a manipulation that caused only an increase in R_{Min} has not been previously reported, therefore VIP+ IN photostimulation is isolating a novel adaptation mechanism. Perhaps because VIP+ INs only inhibit Sst+ INs, but not PV+ INs (whereas Sst+ and PV+ both inhibit each other), VIP+ INs disrupt the balance of inhibitory inputs to Pyr cells during adaptation in a way that differs from how PV+ and Sst+ IN inhibition modulates Pyr cell adaptation.

5.2.2 Why did Pyr cell facilitation via VIP+ activation not increase the magnitude of adaptation?

We were extremely surprised that Pyr cell facilitation caused by VIP+ IN activation did not have any effect on Pyr cell responses to high contrasts. We think there are two potential reasons why VIP+ IN-induced Pyr cell facilitation did not increase the magnitude of adaptation. First, if the firing rate dependent mechanism of V1 adaption is modulated by the local network, increasing the firing rate of a small proportion of Pyr cells while many others are being decreased may not have enough of an effect to alter the magnitude of adaptation. Second, VIP+ IN activation would not cause more adaptation if the mechanisms producing the normal level of Pyr adaptation were already at saturation. This possibility could be tested by inducing milder adaptation in Pyr cells with a lower

adapting contrast while facilitating their firing with VIP+ photostimulaiton.

5.3 GENERAL CIRCUIT ISSUES

5.3.1 VIP+ IN-Induced Pyr Cell Suppression

   We were surprised that VIP+ IN activation caused Pyr cell suppression because this was not predicted by *in vitro* models of the local circuit (Pfeffer et al., 2013; Karnani et al., 2016). However, previous findings that used two-photon photostimulation to map synaptic connections indicate that VIP+ INs have a 12% chance of connecting to a Pyr cell monosynaptically (Fino and Yuste, 2011; Packer and Yuste, 2011), which could produce Pyr inhibition. However, this alone cannot account for relatively frequent VIP+ photostimulation-induced suppression we observed. VIP+ modulation might also indirectly inhibit Pyr cells via disinhibition of other IN subtypes. For example, Pyr cell suppression could be caused by VIP+ activation if this hypothetical VIP+ IN were strongly inhibiting an Sst+ IN, this could provide disinhibition to PV+ INs which in turn could increase the amount of PV+ IN inhibition received by a Pyr cell.

5.3.2 Network Considerations

        Our findings appear to support the theory that INs do not have individual roles but rather modulate Pyr cell activity depending on the state of the network (i.e. INs have state-dependent functions). This was first suggested by El-Boustani and Sur (2014) who found the timing of visual stimuli relative to IN activation greatly affects the type of IN-induced inhibition and suggested that IN responses are a dynamic property of circuitry as opposed to a fixed role. Similarly, in mouse primary auditory cortex, Phillips and Hasenstaub (2016) found that when PV+ and Sst+ INs were activated individually it appeared that these two IN subtypes played similar roles in auditory processing. However, when they inactivated PV+ or Sst+ INs, the two subtypes unexpectedly modulated Pyr cell responses in different ways. Combined, these studies inform researchers that experimental results regarding IN functionality should be carefully interpreted because findings appear to be strongly affected, or "governed" (Phillips and Hasenstaub, 2016), by the state of the network, which is often dictated by experimental design.

5.3.3 Physiological and Anatomical Considerations

In addition to the network state issues outlined above, there are also multiple anatomical and physiological nuances to take into consideration when determining the roles of different IN subtypes. As outlined in the introduction (section 5.1), molecular markers are currently used to divide IN subgroups, however the field is still trying to determine if there is a more optimal IN property to use and classify subtypes. An example of a current IN subtype classification that could possibly benefit from being parsed into two separate groups based on anatomy are Martinotti vs. non-Martinotti Sst+ INs; it is currently not known whether the anatomical differences between these two cell types affect the type of inhibition provided to Pyr cells (for review, see Tremblay et al., 2016). Physiologically, there is evidence that suggests the current classification system does not fully capture the diversity within a genetically defined IN class (Fishell and Rudy, 2011; Markram et al., 2004). For example, Sst+ INs exhibit layer dependent differences in activation (Munoz et al., 2017), and diverse electrophysical and morphological properties within different cortical layers (Nigro et al., 2018); a similar spectrum of functions have also been reported for VIP+ INs (Pronneke et al., 2015). As such, IN roles have likely been overstated and their overall cortical organization and anatomy is possibly more important than previously thought.

There have been several proposed approaches to parse out effects of the heterogenous cell types included within the same genetically defined subgroups. Perhaps the most obvious suggestion is to further divide the current three subgroups. However, as discussed in Tremblay et al. (2016), this task is not nearly as simple as it appears because the proper way to classify INs is still under debate. In lieu of creating more IN subgroups, there are methodological designs researchers can utilize that take the diversity within IN subgroups into consideration. When designing transgenic animals, one could target optogenetic proteins to specific cortical layers via virus injection (e.g. Adesnik, 2018). In terms of equipment, one could utilize micro-LEDs that allow stimulation of a single cell adjacent to a microelectrode to study layer differences within an IN subgroup (for review, see Qazi et al., 2018).

5.4 FUTURE WORK

Investigating the roles of INs in visual processing initially appeared to be a relatively simple endeavor with the advancement of optogenetics, but as we continue to learn more about IN circuitry the results are becoming increasingly difficult to interpret. Therefore, to determine how the current IN subgroups contribute to perception, performing awake-behaving tasks using optogenetic transgenic mice implanted with optrodes is a logical next step. Cone et al. (2019) measured contrast detection thresholds while selectively stimulating PV+, Sst+ or VIP+ INs, and found that PV+ and Sst+ INs decreased mouse performance while VIP+ INs increased performance. However, they did not combine their behavior task with electrophysiological recordings. It would be informative to correlate how Pyr cell activity changes with behavior performance depending the activated IN subtype.

As discussed, one of the reasons that findings from IN investigations are difficult to interpret is that a single IN subtype can be a part of numerous different circuit motifs. If researchers knew how likely it was for an IN to be a member of a specific motif organization, the results from experiments that probe their functionality could be better determined. A possible way to accomplish this is to apply connectomics to the V1 inhibitory circuit. Connectomics refers to the study and production of connectomes, which are essentially maps of connections within the nervous system (for review, see Bassett and Sporns, 2017). On a microscale, connectomes can be made by fixing neural tissue and then imaging it using a 3D electron microscope. Therefore, a connectome of IN connections within the mouse cortex could be constructed by creating transgenic mice that have varying labeling proteins targeted to IN subtypes and their axons/dendrites that are visible under the electron microscope, and then reconstructing their connections via 3D electron microscopy. This information would elegantly complement physiological studies and having an estimate of the probability of IN connections within the circuit would greatly improve our ability to decipher how INs modulate Pyr cell activity because it has becoming increasingly clear that IN networks impact both Pyr cell and IN function (El-Boustani and Sur, 2014; Tremblay et al., 2016).

However helpful it would be to know the likelihood of IN connections for interpreting results from electrophysiological investigations of IN function, it would obviously be the most informative to know the connections within the local circuit you are recording from. This could be achieved by combining a few different methodologies: (1) virus-mediated neuronal circuitry tracing, which is when a virus is injected into a single neuron that labels its connections, allowing researchers to visualize the neuron's local network (Schubert et al., 2017); (2) optogenetics to target IN subtypes within the visualized network; and (3) cell-specific fluorescent labeling with *in vivo* two-photon imaging, which allows many different types of neurons in a living animal to be identified in real-time (for review see Svoboda and Yasuda, 2006). If a lab had the resources to utilize all of these methods in concert, they would be able to visualize connections within the IN circuit they were probing and perturb activity of individual IN subtypes to determine their role in Pyr cell modulation in various IN circuit motifs. This setup would provide the clearest and most straight-forward findings regarding IN roles within local circuits in the cortex.

BIBLIOGRAPHY

Adesnik, H. (2018). Layer-specific excitation / inhibition balances during neuronal synchronization in the visual cortex. J. Physiol. *9*, 1639–1657.

Adesnik, H., Bruns, W., Taniguchi, H., Huang, Z.J., and Scanziani, M. (2012). A neural circuit for spatial summation in visual cortex. Nature *490*, 226–231.

Albrecht, D.G., and Hamilton, D.B. (1982). Striate cortex of monkey and cat: contrast response function. J. Neurophysiol. *48*, 217–237.

Ali, A.B., and Thomson, A.M. (2008). Synaptic alpha 5 subunit-containing GABAA receptors mediate IPSPs elicited by dendrite-preferring cells in rat neocortex. Cereb. Cortex *18*, 1260–1271.

Allman, J.M., and Kaas, J.H. (1971). A representation of the visual field in the caudal third of the middle temporal gyrus of the owl monkey (Aotus trivirgatus). Brain Researh *31*, 85–105.

Amitai, Y., Gibson, J.R., Beierlein, M., Patrick, S.L., Ho, A.M., Connors, B.W., and Golomb, D. (2002). The spatial dimensions of electrically coupled networks of interneurons in the neocortex. J. Neurosci. *22*, 4142–4152.

Applebury, M.L., Antoch, M.P., Baxter, L.C., Chun, L.L.Y., Falk, J.D., Farhangfar, F., Kage, K., Krzystolik, M.G., Lyass, L.A., and Robbins, J.T. (2000). The Murine Cone Photoreceptor : A Single Cone Type Expresses Both S and M Opsins with Retinal Spatial Patterning. Neuron *27*, 513–523.

Asrican, B., Augustine, G.J., Berglund, K., Chen, S., Chow, N., Deisseroth, K., Feng, G., Gloss, B., Hira, R., Hoffmann, C., et al. (2013). Next-generation transgenic mice for optogenetic analysis of neural circuits. Front. Neural Circuits *7*, 1–24.

Atallah, B. V., Bruns, W., Carandini, M., and Scanziani, M. (2012). Parvalbumin-expressing interneurons linearly transform cortical responses to visual stimuli. Neuron *73*, 159–170.

Atallah, B. V., Scanziani, M., and Carandini, M. (2014). Atallah et al. reply. Nature *508*, E3.

Baker, M. (2013). Through the eyes of a mouse. Nature *502*, 156–158.
Bartfeld, E., and Grinvald, A. (1992). Relationships between orientation-preference pinwheels , cytochrome oxidase blobs , and ocular-dominance columns in primate striate cortex. Proc. Natl. Acad. Sci. *89*, 11905–11909.

Bassett, D.S., and Sporns, O. (2017). Network neuroscience. Nat. Neurosci. *20*, 353–364.

Bayraktar, T., Welker, E., Freund, T.F., Zilles, K., and Staiger, J.F. (2000). Neurons immunoreactive for vasoactive intestinal polypeptide in the rat primary somatosensory cortex: morphology and spatial relationship to barrel-related columns. J. Comp. Neurol. *420*, 291–304.

Beierlein, M., Gibson, J., and Connors, B. (2003). Two dynamically distinct inhibitory networks in layer 4 of the neocortex. J. Neurophysiol. *90*, 2987–3000.

Benjamini, Y., and Hochberg, Y. (1995). Controlling the False Discovery Rate: A Practical and Powerful Approach to Multiple Testing. J. R. Stat. Soc. *57*, 289–300.

Bickford, M.E., Wei, H., Eisenback, M.A., Chomsung, R.D., Slursarczyk, A.S., and Dankowski, A.B. (2008). Synaptic organization of thalamocortical axon collaterals in the perigeniculate nucleus and dorsal lateral geniculate nucleus. J. Comp. Neurol. *508*, 264–285.

Blakemore, C., and Campbell, F. (1969). On the existence of neurones in the human visual system selectivity sensitive to the orientation and size of retinal images. J. Physiol. *203*, 237–260.

Blitz, D.M., and Regehr, W.G. (2005). Timing and Specificity of Feed-Forward Inhibition within the LGN. *45*, 917–928.

Boyden, E.S., Zhang, F., Bamberg, E., Nagel, G., and Deisseroth, K. (2005). Millisecond-timescale, genetically targeted optical control of neural activity. Nat. Neurosci. *8*, 1263–1268.

Brainard, D.H. (1997). The psychophysics toolbox. Spat. Vis. *10*, 433–436.

Bryda, E.C. (2013). The Mighty Mouse: The Impact of Rodents on Advances in Biomedical Research. 207–211.

Callaway, E.M. (1998). Local circuits in primary visual cortex of the macaque monkey. Annu. Rev. Neurosci. *21*, 47–74.

Callaway, E.M. (2005). Structure and function of parallel pathways in the primate early visual system. *1*, 13–19.

Carandini, M., and Heeger, D. (2012). Normalization as a canonical neural computation. Nat. Neurosci. *13*, 51–62.

Chiu, C.Q., Lur, G., Morse, T.M., Carnevale, N.T., Ellis-Davies, G.C., and Higley, M.J. (2013). Compartmentalization of GABAergic inhibition by dendritic spines. Science (80-.). *340*, 759–762.

Cohen, S.N., Chang, A.C.Y., Boyert, H.W., and Hellingt, R.B. (1973). Construction of biologically functional bacterial plasmids in vitro. Proc. Natl. Acad. Sci. *70*, 3240–3244.

Coltheart, M. (1971). Visual feature-analyzers and aftereffects of tilt and curvature. Psychol. Rev. *78*, 114–121.

Cone, J.J., Scantlen, M.D., Histed, M.H., and Maunsell, J.H.R. (2019). Different Inhibitory Interneuron Cell Classes Make Distinct Contributions to Visual Contrast Perception. *107464*, 1–12.

Connolly, M., and Van Essen, D. (1984). The representation of the visual field in parvicellular and magnocellular layers of the lateral geniculate nucleus in the macaque monkey. J. Comp. Neurol. *226*, 544–564.

Costantini, F., and Lacy, E. (1981). Introduction of a rabbit β-globin gene into the mouse germ line. Nature *294*, 92–94.

Dadarlat, X.M.C., and Stryker, X.M.P. (2017). Locomotion Enhances Neural Encoding of Visual Stimuli in Mouse V1. J. Neurosci. *37*, 3764–3775.

Dantzker, J.L., and Callaway, E.M. (2000). Laminar sources of synaptic input to cortical inhibitory interneurons and pyramidal neurons. Nat. Neurosci. *3*, 701–707.

Dean, A., and Tolhurst, D.J. (1983). On the distinctness of simple and complex cells in the visual cortex of the cat. J. Physiol. *344*, 305–325.

DeAngelis, G.C., Ohzawa, I., and Freeman, R.D. (1993). Spatiotemporal organization of simple-cell receptive fields in the cat's striate cortex. II. Linearity of temporal and spatial summation. J. Neurophysiol. *69*, 1118–1135.

DeFelipe, J., and Jones, E. (1988). Cajal on the Cerebral Cortex: An Annotated Translation of the Complete Writings.

Deisseroth, K. (2010). Optogenetics: Controlling the Brain with Light. Sci. Am.

Demb, J.B., and Singer, J.H. (2015). Functional Circuitry of the Retina. Annu. Rev. Vis. Sci. *1*, 263–289.

El-Boustani, S., and Sur, M. (2014). Response-dependent dynamics of cell-specific inhibition in cortical networks in vivo. Nat. Commun. *5*, 1–14.

El-Boustani, S., Wilson, N.R., Runyan, C.A., and Sur, M. (2014). El-Boustani et al. reply. Nature *508*, E3–E4.

Engel, S.A., and Furmanski, C.S. (2001). Selective Adaptation to Color Contrast in

Human Primary Visual Cortex. J. Neurosci. *21*, 3949–3954.

Fino, E., and Yuste, R. (2011). Dense inhibitory connectivity in neocortex. Neuron *69*, 1188–1203.

Fishell, G., and Rudy, B. (2011). Mechanisms of Inhibition within the Telencephalon: "Where the Wild Things Are." Annu. Rev. Neurosci. *34*, 535–567.

Freund, T.F. (2003). Interneuron Diversity series: Rhythm and mood in perisomatic inhibition. Trends Neurosci. *26*, 489–495.

Fries, W. (1984). Cortical projections to the superior colliculus in the macaque monkey: A retrograde study using horseradish peroxidase. J. Comp. Neurol. *230*, 55–76.

Fu, Y., Tucciarone, J.M., Espinosa, J.S., Sheng, N., Darcy, D.P., Nicoll, R.A., Huang, Z.J., and Stryker, M.P. (2014). A cortical circuit for gain control by behavioral state. Cell *156*, 1139–1152.

Galarreta, M., and Hestrin, S. (1999). A network of fast-spiking cells in the neocortex connected by electrical synapses. Nature *402*, 72–75.

Gao, E., DeAngelis, G.C., and Burkhalter, A. (2010). Parallel input channels to mouse primary visual cortex. J. Neurosci. *30*, 5912–5926.

Garrett, M.E., Nauhaus, I., Marshel, J.H., and Callaway, X.E.M. (2014). Topography and Areal Organization of Mouse Visual Cortex. J. Neurosci. *34*, 12587–12600.

Ghodrati, M., Khaligh-razavi, S., and Lehky, S.R. (2017). Towards building a more complex view of the lateral geniculate nucleus : Recent advances in understanding its role Progress in Neurobiology Towards building a more complex view of the lateral geniculate nucleus : Recent advances in understanding its role. Prog. Neurobiol.

Gibson, J., Beierlein, M., and Connors, B. (1999). Two networks of electrically coupled inhibitory neurons in neocortex. Nature *402*, 75–79.

Group, P.I.N. (2008). Petilla terminology: nomenclature of features of GABAergic interneurons of the cerebral cortex. Nat. Rev. Neurosci. *9*, 557–568.

Guru, A., Post, R.J., Ho, Y., and Warden, M.R. (2015). Making Sense of Optogenetics. 1–8.

Gutierrez, C., and Cusick, C. (1997). Area V1 in macaque monkeys projects to multiple histochemically defined subdivisions of the inferior pulvinar complex. Brain Res. *765*, 349–356.

Hendry, S.H., and Reid, R.C. (2000). The koniocellular pathway in primate vision. Annu.

Rev. Neurosci. *23*, 127–153.

Hildebrand, G.D., and Fielder, A.R. (2011). Anatomy and physiology of the retina. In Pediatric Retina, pp. 39–65.

Van Hooser, S.D., Heimel, J.A.F., Chung, S., Nelson, S.B., and Toth, L.J. (2005). Orientation selectivity without orientation maps in visual cortex of a highly visual mammal. J. Neurosci. *25*, 19–28.

Howarth, M., Walmsley, L., and Brown, T.M. (2014). Binocular integration in the mouse lateral geniculate nuclei. Curr. Biol. *24*, 1241–1247.

Hubel, D.H., and Wiesel, T.N. (1962). Receptive fields, binocular interaction and functional architecture in the cat's visual cortex. J. Physiol. *160*, 106–154.

Ichida, J.M., and Casagrande, V. (2002). Organization of the feedback pathway from striate cortex (V1) to the lateral geniculate nucleus (LGN) in the owl monkey (Aotus trivirgatus). J. Comp. Neurol. *454*, 272–283.

Ingram, T.G.J., King, J.L., and Crowder, N.A. (2019). Divisive Inhibition Prevails During Simultaneous Optogenetic Activation of All Interneuron Subtypes in Mouse Primary Visual Cortex. Front. Neural Circuits *13*, 1–10.

International Human Genome Sequencing Consortium (2001). Initial sequencing and analysis of the human genome. Nature *409*, 860–921.

Irvin, G.E., Casagrande, V.A., and Norton, T.T. (1993). Center/surround relationships of magnocellular, parvocellular, and koniocellular relay cells in primate lateral geniculate nucleus. Vis. Neurosci. *10*, 363–373.

Jackson, J., Ayzenshtat, I., Karnani, M.M., and Yuste, R. (2016). VIP+ interneurons control neocortical activity across brain states. J. Neurophysiol. 3008–3017.

Jacobs, G.H., and Yolton, R.L. (1970). Center-surround balance in receptive fields of cells in the lateral geniculate nucleus. Vision Res. *10*, 1124–1144.

Jacobs, G.H., Williams, G.A., Cahill, H., and Nathans, J. (2007). Emergence of Novel Color Vision in Mice Engineered to Express a Human Cone Photopigment. Science (80-.). *315*, 1723–1725.

Jeon, C.J., Strettoi, E., and Masland, R.H. (1998). The major cell populations of the mouse retina. J. Neurosci. *18*, 8936–8946.

Jiang, X., Shen, S., Cadwell, C.R., Berens, P., Sinz, F., Ecker, A.S., Patel, S., and Tolias, A.S. (2015). Principles of connectivity among morphologically defined cell types in adult neocortex. Science (80-.). aac9462.

Jones, A.E. (1964). The lateral geniculate nucleus of Ateles ater. J. Comp. Neurol. *123*, 205–210.

Karnani, M.M., Agetsuma, M., and Yuste, R. (2014). A blanket of inhibition: Functional inferences from dense inhibitory connectivity. Curr. Opin. Neurobiol. *26*, 96–102.

Karnani, X.M.M., Jackson, J., Ayzenshtat, I., Sichani, X.A.H., Manoocheri, K., Kim, S., and Yuste, R. (2016). Opening Holes in the Blanket of Inhibition : Localized Lateral Disinhibition by VIP Interneurons. J. Neurosci. *36*, 3471–3480.

Kawaguchi, Y., and Kubota, Y. (1997). GABAergic cell subtypes and their synaptic connections in rat frontal cortex. Cereb. Cortex *7*, 476–486.

King, J.L., and Crowder, N.A. (2018). Adaptation to stimulus orientation in mouse primary visual cortex. Eur. J. Neurosci. *47*, 346–357.

King, J.L., Lowe, M.P., and Crowder, N.A. (2015). Contrast adaptation is spatial frequency specific in mouse primary visual cortex. Neuroscience *310*, 198–205.

King, J.L., Lowe, M.P., Stover, K.R., Wong, A.A., Crowder, N.A., King, J.L., Lowe, M.P., Stover, K.R., Wong, A.A., and Crowder, N.A. (2016). Adaptive Processes in Thalamus and Cortex Revealed by Silencing of Primary Visual Cortex during Contrast Adaptation. Curr. Biol. *26*, 1–6.

Kohn, A. (2007). Visual adaptation: physiology, mechanisms, and functional benefits. J. Neurophysiol. *97*, 3155–3164.

Kubota, Y. (2014). Untangling GABAergic wiring in the cortical microcircuit. Curr. Opin. Neurobiol. *26*, 7–14.

Kuffler, S.W. (1953). Discharge patterns and functional organization of mammalian retina. J. Neurophysiol. *16*, 37–68.

LeDue, E.E., King, J.L., Stover, K.R., and Crowder, N.A. (2013). Spatiotemporal specificity of contrast adaptation in mouse primary visual cortex. Front. Neural Circuits *7*, 154.

Lee, S.-H., Kwan, A.C., Zhang, S., Phoumthipphavong, V., Flannery, J.G., Masmanidis, S.C., Taniguchi, H., Huang, Z.J., Zhang, F., Boyden, E.S., et al. (2012). Activation of specific interneurons improves V1 feature selectivity and visual perception. Nature *488*, 379–383.

Lee, S., Hjerling-Leffler, J., Zagha, E., Fishell, G., and Rudy, B. (2010). The largest group of superficial neocortical GABAergic interneurons expresses ionotropic serotonin

receptors. J. Neurosci. *30*, 16796–16808.

Lee, S.H., Kwan, A.C., and Dan, Y. (2014). Interneuron subtypes and orientation tuning. Nature *508*, E1–E2.

Livingstone, M.S., and Hubel, D.H. (1988). Do the Relative Mapping Densities of the Magno- and Parvocellular Systems Vary with Eccentricity ? J. Neurosci. *8*, 4334–4339.

Lund, J.S., Angelucci, A., and Bressloff, P.C. (2003). Anatomical Substrates for Functional Columns in Macaque Monkey Primary Visual Cortex. Cereb. Cortex *12*, 15–24.

Markram, H., Toledo-Rodriguez, M., Wang, Y., Gupta, A., Silberberg, G., and Wu, C. (2004). Interneurons of the neocortical inhibitory system. Nat. Rev. Neurosci. *5*, 793–807.

Marks, W., Dobelle, W., and MacNichol Jr., E. (1964). Visual Pigments of Single Primate Cones. Science (80-.). *143*, 1181–1182.

Marshel, J.H., Garrett, M.E., Nauhaus, I., and Callaway, E.M. (2011). Functional specialization of seven mouse visual cortical areas. Neuron *72*, 1040–1054.

Maunsell, J.H.R., and Newsome, W.T. (1987). Visual processing in monkey extrastriate cortex. Annu. Rev. Neurosci. *10*, 363–401.

Meyer, H.S., Schwarz, D., Wimmer, V.C., Schmitt, A.C., Kerr, J.N.D., Sakmann, B., and Helmstaedter, M. (2011). Inhibitory interneurons in a cortical column form hot zones of inhibition in layers 2 and 5A. Proc. Natl. Acad. Sci. *108*, 16807–16812.

Milner, A., and Goodale, M. (1995). The visual brain in action. In Oxford:Oxford University Press

Motulsky, H.J., and Ransnas, L.A. (1987). Fitting Curves to Data using Nonlinear Regression: A Practical and Non-Mathematical Review. FASEB J. *1*, 365–374.

Mouse Genome Sequencing Consortium (2002). Initial sequencing and comparative analysis of the mouse genome. Nature *420*, 520–562.

Munoz, W., Tremblay, R., Levenstein, D., and Rudy, B. (2017). Layer-specific modulation of neocortical dendritic inhibition during active wakefulness William. Science (80-.). *355*, 954–959.

Nauhaus, I., Benucci, A., Carandini, M., and Ringach, D.L. (2008). Neuronal selectivity and local map structure in visual cortex. Neuron *57*, 673–679.

Niell, C.M., and Stryker, M.P. (2008). Highly selective receptive fields in mouse visual

cortex. J. Neurosci. *28*, 7520–7536.

Nigro, M.J., Hashikawa-Yamasaki, Y., and Rudy, B. (2018). Diversity and Connectivity of Layer 5 Somatostatin-Expressing Interneurons in the Mouse Barrel Cortex. J. Neurosci. *38*, 1622–1633.

Ohki, K., Chung, S., Ch'ng, Y.H., Kara, P., and Reid, R.C. (2005). Functional imaging with cellular resolution reveals precise micro-architecture in visual cortex. Nature *433*, 597–603.

Packer, A.M., and Yuste, R. (2011). Dense, Unspecific Connectivity of Neocortical Parvalbumin-Positive Interneurons: A Canonical Microcircuit for Inhibition? J. Neurosci. *31*, 13260–13271.

Packer, O., Hendrickson, A.E., and Curcio, C.A. (1989). Photoreceptor topography of the retina in the adult pigtail macaque (Macaca nemestrina). J. Comp. Neurol. *288*, 165–183.

Pelli, D. (1997). The VideoToolbox software for visual psychophysics: transforming numbers into movies. Spat. Vis. *10*, 437–447.

Perkel, D.J., Bullier, J., and Kennedy, H. (1986). Topography of the afferent connectivity of area 17 in the macaque monkey: A double-labelling study. J. Comp. Neurol. *253*, 374–402.

Pfeffer, C.K., Xue, M., He, M., Huang, Z.J., and Scanziani, M. (2013). Inhibition of inhibition in visual cortex: the logic of connections between molecularly distinct interneurons. Nat. Neurosci. *16*, 1068–1076.

Phillips, E.A.K., Hasenstaub, A.R., Francisco, S., Francisco, S., and States, U. (2016). Asymmetric effects of activating and inactivating cortical interneurons. 1–22.

Porter, J.T., Cauli, B., Staiger, J.F., Lambolez, B., Rossier, J., and Audinat, E. (1998). Properties of bipolar VIPergic interneurons and their excitation by pyramidal neurons in the rat neocortex. Eur. J. Neurosci. *10*, 3617–3628.

Prasad, S., and Galetta, S.L. (2011). Anatomy and physiology of the afferent visual system. In Handbook of Clinical Neurology, pp. 3–19.

Pronneke, A., Scheuer, B., Wagener, R.J., Mock, M., Witte, M., and Staiger, J.F. (2015). Characterizing VIP neurons in the barrel cortex of VIPcre/tdTomato mice reveals layer-specific differences. Cereb. Cortex *25*, 4854–4868.

Qazi, R., Kim, C.Y., Byun, S., Jeong, J., and Vittorio, M. De (2018). Microscale Inorganic LED Based Wireless Neural Systems for Chronic in vivo Optogenetics. Front. Neurosci. *12*, Article 764.

Ringach, D.L., Mineault, P.J., Tring, E., Olivas, N.D., Garcia-Junco-Clemente, P., and Trachtenberg, J.T. (2016). Spatial clustering of tuning in mouse primary visual cortex. Nat. Commun. *7*, 1–9.

Rockland, K.S., and Van Hosen, G.W. (1994). Direct temporal-occipital feedback connections to striate cortex (V1) in the macaque monkey. Cereb. Cortex *4*, 300–313.

Sanchez-Vives, M., Nowak, L., and McCormick, D. (2000). Cellular mechanisms of long-lasting adaptation in visual cortical neurons in vitro. J. Neurosci. *20*, 4286–4299.

Scholl, B., Tan, A.Y.Y., Corey, J., and Priebe, N.J. (2013). Emergence of orientation selectivity in the mammalian visual pathway. J. Neurosci. *33*, 10616–10624.

Schubert, R., Trenholm, S., Balint, K., Kosche, G., Cowan, C.S., Mohr, M.A., Martin Munz, D., Martinez-Martin, Fläschner, G., Newton, R., et al. (2017). Virus stamping for targeted single-cell infection in vitro and in vivo. Nat. Biotechnol. *26*, 81–88.

Sclar, G., Lennie, P., and DePriest, D.D. (1989). Contrast adaptation in striate cortex of macaque. Vision Res. *29*, 747–755.

Shipp, S., and Zeki, S. (1989). The organization of connections between areas V5 and V2 in macaque monkey visual cortex. Eur. J. Neurosci. *1*, 333–354.

Snell, R.S., and Lemp, M.A. (1998). Clinical Anatomy of the Eye (Blackwell Science, Inc.).

Somogyi, P., Tamas, G., Lujan, R., and Buhl, E. (1998). Salient features of synaptic organisation in the cerebral cortex. Brain Res. Rev. *26*, 113–135.

Stujenske, J.M., Spellman, T., Gordon, J.A., Stujenske, J.M., Spellman, T., and Gordon, J.A. (2015). Modeling the Spatiotemporal Dynamics of Light and Heat Propagation for In Vivo Optogenetics Resource Modeling the Spatiotemporal Dynamics of Light and Heat Propagation for In Vivo Optogenetics. Cell Rep. *12*, 525–534.

Svoboda, K., and Yasuda, R. (2006). Principles of Two-Photon Excitation Microscopy and Its Applications to Neuroscience. Neuron *50*, 823–839.

Tasic, Bosiljka Menon, Vilas Nguyen, Thuc Nghi Kim, Tae Kyung Jarsky, Tim Yao, Zizhen Levi, Boaz Gray, Lucas T Sorensen, Staci A Dolbeare, Tim Bertagnolli, Darren Goldy, J., Shapovalova, N., Parry, S., Lee, C., Smith, K., Bernard, A., Madisen, L., Sunkin, Susan M Hawrylycz, Michael Koch, C., and Zheng, H. (2016). Adult mouse cortical cell taxonomy revealed by single cell transcriptomics. Nat. Neurosci. *19*, 335–346.

Tootell, R.B., Switkes, E., Silverman, M.S., and Hamilton, S.S. (1988). Functional Anatomy Organization of Macaque Striate Cortex . J. Neurosci. *8*, 1531–1568.
Toth, L.J., Rao, S.C., Kim, D.-S., Somers, D.C., and Sur, M. (1996). Subthreshold facilitation and suppression in primary visual cortex revealed by intrinsic signal imaging. Proc. Natl. Acad. Sci. *93*, 9869–9874.

Tremblay, R., Lee, S., and Rudy, B. (2016). GABAergic Interneurons in the Neocortex : From Cellular Properties to Circuits. Neuron *91*, 260–292.

Ungerleider, L.G., and Desimone, R. (1986). Cortical connections of visual area MT in the macaque. J. Comp. Neurol. *248*, 190–222.

Wagor, E., Mangini, N.J., and Pearlman, A.L. (1980). Retinotopic organization of striate and extrastriate visual cortex in the mouse. J. Comp. Neurol. *193*.

Walls, G.L. (1953). The lateral geniculate nucleus and visual histophysiology. Univ Calif Publ Physiol *9*, 1–100.

Wang, Q., and Burkhalter, A. (2007). Area Map of Mouse Visual Cortex. J. Comp. Neurol. *357*, 339–357.

Wang, Q., Sporns, O., and Burkhalter, A. (2012). Network Analysis of Corticocortical Connections Reveals Ventral and Dorsal Processing Streams in Mouse Visual Cortex. J. Neurosci. *32*, 4386–4399.

Wang, Y., Toledo-Rodriguez, M., Gupta, A., Wu, C., Silberberg, G., Luo, J., and Markram, H. (2004). Anatomical, physiological and molecular properties of Martinotti cells in the somatosensory cortex of the juvenile rat. J. Physiol. *561*, 65–90.

Wikler, K., and Rakic, P. (1990). Distribution of Photoreceptor Nocturnal Primates Subtypes in the Retina of Diurnal and Nocturnal Primates. J. Neurosci. *10*, 3390–3401.

Wilson, N.R., Runyan, C.A., Wang, F.L., and Sur, M. (2012). Division and subtraction by distinct cortical inhibitory networks in vivo. Nature *488*, 343–348.

Wimbauer, S., Wenisch, O.G., Miller, K.D., and van Hemmen, J.L. (1997). Development of spatiotemporal receptive fields of simple cells: I. Model formulation. Biol. Cybern. *77*, 453–461.

Xu, X., and Callaway, E.M. (2009). Laminar Specificity of Functional Input to Distinct Types of Inhibitory Cortical Neurons. J. Neurosci. *29*, 70–85.

Xu, X., Ichida, J., Shostak, Y., Bonds, A., and Casagrande VA (2002). Are primate lateral geniculate nucleus (LGN) cells really sensitive to orientation or direction? Vis.

Neurosci. *19*, 97–108.

Xu, X., Roby, K.D., and Callaway, E.M. (2010). Immunochemical characterization of inhibitory mouse cortical neurons: Three chemically distinct classes of inhibitory cells. J. Comp. Neurol. *518*, 389–404.

Yau, K.-W. (1994). Phototransduction mechanism in rods and cones. Investig. Ophthalmol. Vis. Sci. *35*, 9–32.

Yizhar, O., Fenno, L.E., Davidson, T.J., Mogri, M., and Deisseroth, K. (2011). Optogenetics in Neural Systems. Neuron *71*, 9–34.

Yona, G., Meitav, N., Kahn, I., and Shoham, S. (2016). Realistic Numerical and Analytical Modeling of Light Scattering in Brain Tissue for Optogenetic Applications. ENeuro *3*, ENEURO.0059-15.2015.

Zeisel, A., Muñoz-Manchado, A.B., Codeluppi, S., Lönnerberg, P., La Manno, G., Juréus, A., Marques, S., Munguba, H., He, L., Betsholtz, C., et al. (2015). Cell types in the mouse cortex and hippocampus revealed by single-cell RNA-seq. Science (80-.). *347*, 1138–1142.

Zeki, S. (1983). The distribution of wavelength and orientation selective cells in different areas of monkey visual cortex. Proc. R. Soc. London Biol. *217*, 449–470.

APPENDIX 1

Adaptive Processes in Thalamus and Cortex Revealed by Silencing of Primary Visual Cortex during Contrast Adaptation

Jillian L. King,[1] Matthew P. Lowe,[1] Kurt R. Stover,[1] Aimee A. Wong,[1] and Nathan A. Crowder[1,*]
[1]Department of Psychology and Neuroscience, Dalhousie University, Halifax, NS B3H 4R2, Canada
*Correspondence: nathan.crowder@dal.ca
http://dx.doi.org/10.1016/j.cub.2016.03.018

SUMMARY

Visual adaptation illusions indicate that our perception is influenced not only by the current stimulus but also by what we have seen in the recent past. Adaptation to stimulus contrast (the relative luminance created by edges or contours in a scene) induces the perception of the stimulus fading away and increases the contrast detection threshold in psychophysical tests [1, 2]. Neural correlates of contrast adaptation have been described throughout the visual system including the retina [3], dorsal lateral geniculate nucleus (dLGN) [4, 5], primary visual cortex (V1) [6], and parietal cortex [7]. The apparent ubiquity of adaptation at all stages raises the question of how this process cascades across brain regions [8]. Focusing on V1, adaptation could be inherited from pre-cortical stages, arise from synaptic depression at the thalamo-cortical synapse [9], or develop locally, but what is the weighting of these contributions? Because contrast adaptation in mouse V1 is similar to classical animal models [10, 11], we took advantage of the optogenetic tools available in mice to disentangle the processes contributing to adaptation in V1. We disrupted cortical adaptation by optogenetically silencing V1 and found that adaptation measured in V1 now resembled that observed in dLGN. Thus, the majority of adaptation seen in V1 neurons arises through local activity-dependent processes, with smaller contributions from dLGN inheritance and synaptic depression at the thalamo-cortical synapse. Furthermore, modeling indicates that divisive scaling of the weakly adapted dLGN input can predict some of the emerging features of V1 adaptation.

RESULTS AND DISCUSSION

Adaptation in primary visual cortex (V1) depends somewhat on firing rate [12, 13]. Therefore, we reasoned that optogenetically silencing V1 could help disentangle inherited dorsal lateral geniculate nucleus (dLGN) adaptation and thalamo-cortical synaptic depression, both of which should be unaltered by silencing, from the locally produced adaptation that should be minimized by silencing.
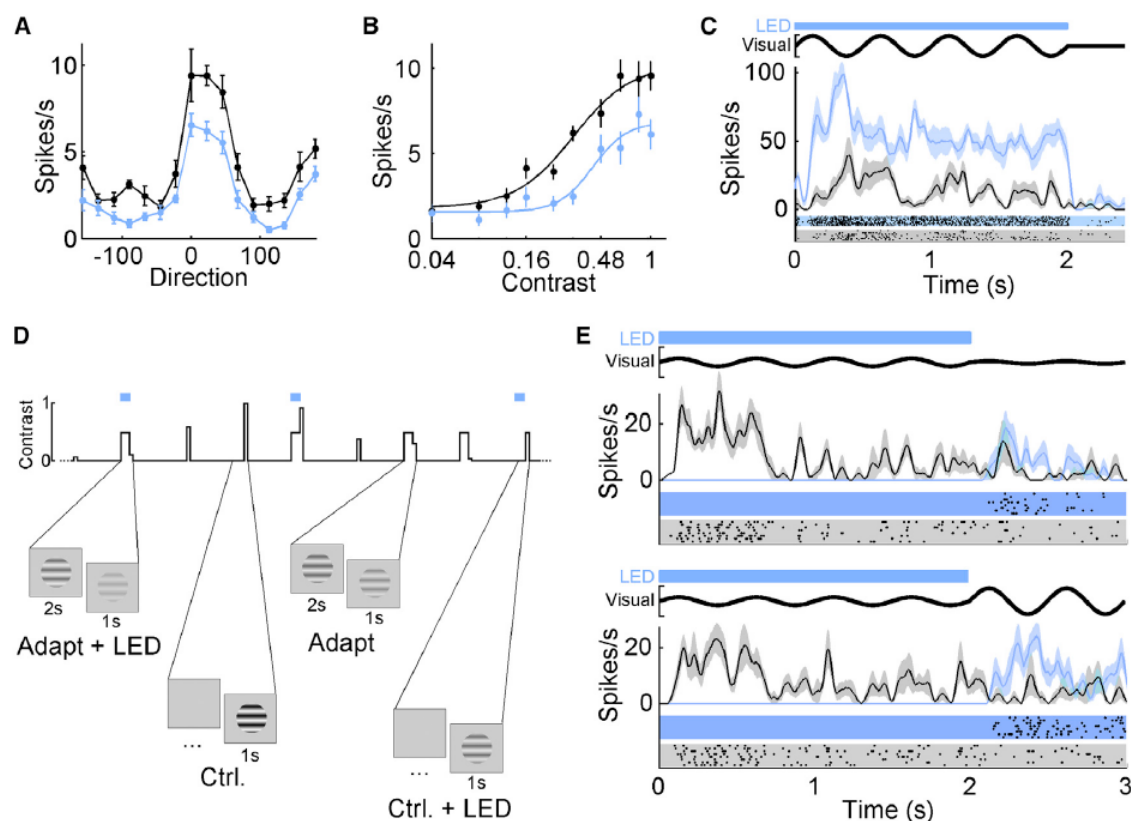
Photostimulation Effects

For cortical silencing, we used VGAT-ChR2(H134R)-YFP (yellow fluorescent protein) transgenic mice that express light-sensitive channelrhodopsin-2 (ChR2(H134R)) in all GABAergic interneurons [14]. Therefore, we first sought to confirm that photostimulation could modulate neural activity in a similar way to previous work that induced cortical silencing with ChR2 expressed via adeno-associated viruses [15, 16]. As expected from the diverse and reciprocal connections among GABAergic and excitatory neurons [17], submaximal photostimulation that modulated interneuron activity over a moderate range produced suppression in some cells (Figures 1A and 1B) and activation in others (Figure 1C). Suppressed cells were selected for, and higher-intensity photostimulation used in the adaptation protocol was sufficient to silence neural activity during the adaptation period, or nearly so, for all neurons tested (Figure 1E). Silencing was observed at all recording depths, similar to the effect of strongly driving parvalbumin-expressing (Pvalb+) interneurons alone [15, 16].

Silencing V1 Neurons Alters Contrast Adaptation

We minimized cortical adaptation with a novel photostimulation protocol that optogenetically silenced V1 neurons during the presentation of the adapting stimulus, but not during the test stimulus (Figures 1D and 1E). Contrast adaptation normally caused the adapted contrast response functions of V1 neurons to shift downward and rightward (Figures 2A, 2C, and 2E, white dots); however, photostimulation during the adapting period markedly dampened these effects and actually increased responses to low contrasts (Figures 2A, 2C, and 2E, blue dots). Regular adapted V1 responses to low contrasts are often unchanged (Figures 2A and 2E), or occasionally decreased slightly (Figure 2C), so this facilitation was surprising. The average of the normalized curves (n = 51) illustrates the consistent changes induced both by adaptation and photostimulation (Figure 3A).

Sigmoid fits to each contrast response function are shown as thin curves in Figure 2 (see Supplemental Experimental Procedures), and the R_{max}, c_{50}, and M fit parameters were used to quantitatively analyze changes in our sample's contrast response functions induced by adaptation and photostimulation. Decreases in R_{max} indicate lower adapted responses to maximal contrast (response gain control), and increases in c_{50} indicate a rightward shift in the curve (contrast gain control) [18]. Increases

Figure 1. Optogenetic Modulation of V1 Responses in VGAT-ChR2(H134R)-YFP Transgenic Mice

(A) Orientation tuning of a sample neuron (black) suppressed by moderate-intensity LED photostimulation (blue).

(B) Contrast response function of a sample neuron (black) suppressed by moderate intensity LED photostimulation (blue).

(C) Spike density functions (SDFs) and rasters for a putative GABAergic neuron's response to high-contrast gratings with (blue) or without (black) LED illumination.

(D) Schematic of the contrast adaptation protocol depicting the stimulus contrast changing over a snippet of time. Photostimulation trials (blue bars) were randomly interleaved with regular adaptation trials. Note the coordination of visual stimuli and photostimulation in the examples of the four trial types.

(E) Contrast adaptation with V1 silencing using high-intensity LED photostimulation. Adapt (black) and adapt+LED (blue) trials with 0.5 adapting contrast and 0.04 (top) or 0.84 (bottom) test contrasts.

In (C) and (E), the timing of visual (thick black lines) and LED (blue bars) stimulation is shown above the SDFs. For visual stimulation, the luminance of a point on the visual stimulus is indicated, such that the amplitude of the sine wave indicates the contrast of the drifting gratings. Error bars in (A) and (B) plus shaded regions in (C) and (E) indicate SEM.

in M coupled with decreases in R_{max} characterized the low-contrast facilitation. R_{max} and M parameters were normalized by each neuron's nonadapted response to full contrast gratings to help compare cells with different firing rates. As expected, normal contrast adaptation produced large and significant reductions in R_{max} (Figure 3D; mean difference $\overline{X}$ = −0.37; 95% confidence interval [CI] [−0.42, −0.31]; p = 1.4 × 10^{-16}), and increases in c_{50} (Figure 3E; $\overline{X}$ = 0.21; 95% CI [0.16, 0.26]; p = 6.5 × 10^{-11}), without affecting baseline firing (Figure 3F; $\overline{X}$ = −0.01; 95% CI [−0.02, 0.01]; p = 0.66). Silencing activity during the adapting period caused significant increases from adapted levels in R_{max} (Figure 3D; $\overline{X}$ = 0.13; 95% CI [0.09, 0.17]; p = 6.2 × 10^{-7}) and M (Figure 3F; $\overline{X}$ = 0.1; 95% CI [0.07, 0.14]; p = 3.9 × 10^{-6}) and c_{50} values to decrease significantly (Figure 3E; $\overline{X}$ = −0.07; 95% CI [−0.11, −0.02]; p = 0.02). Figure S1 contains the same data summarized in Figures 3D–3F but plots individual data points as well. These results contrast with earlier work suggesting adaptation was unaffected by pharmacologically silencing V1 [19], perhaps because the precise temporal

control afforded by optogenetics better matches the rapid pace of adaptive changes. Importantly, C57BL/6J mice used as wild-type controls showed normal contrast adaptation but no photostimulation effect (Figures 3B and 3D–3F). Together, these results reveal that cortical silencing during the adapting period markedly altered adapted V1 responses that were measured after photostimulation had ceased.

The low-contrast facilitation observed following cortical silencing was unexpected, so we performed several control experiments and analyses to test whether it could be a rebound artifact of optogenetic photostimulation. First, for a subset of neurons (n = 25), photostimulation occurred on nonadapted trials for 2 s before the test stimulus was presented (Ctrl.+LED condition in Figure 1D). Photostimulation suppressed spontaneous firing but did not cause any consistent changes to contrast response functions across the population (Figure S2). Rebound effects may be transient in nature, so we took advantage of the fact that our test gratings were presented for 1 s drifting at 2 Hz and separately analyzed responses to the first and second
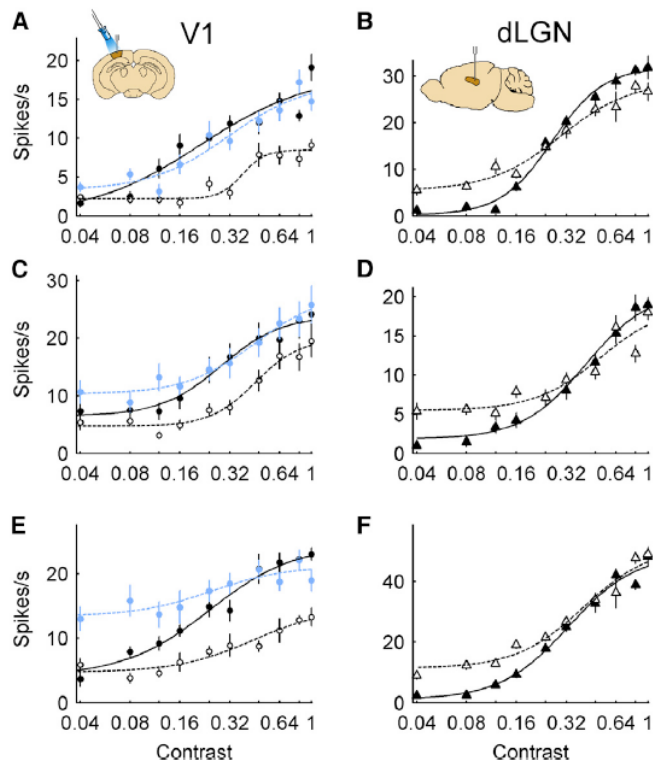
Figure 2. Examples of Contrast Adaptation in V1 and dLGN

Contrast response functions for three sample V1 neurons (A, C, and E, circles) and three sample dLGN neurons (B, D, and F, triangles), with contrast on the abscissa and mean response rate on the ordinate. Non-adapted control, adapt, and adapt+LED conditions are shown as black symbols, empty symbols, and blue dots, respectively. Error bars represent SEM, and thin lines represent best fits to a sigmoid function (see Supplemental Experimental Procedures).

grating cycles of 0.04 contrast. Facilitation was observed in both time bins, but there was no difference in the level of enhancement between the first and second cycles (Figure S3A; p = 0.63). Rebound effects or after-discharges are also not expected to be modulated with the temporal frequency of the stimulus [20], so we also re-analyzed the contrast response functions of neurons that were at least somewhat phase sensitive (F_1/F_0 ratio > 0.5), focusing on the F_1 component of the response (see Supplemental Experimental Procedures). The increase in M with photostimulation remained apparent using this analysis (Figure S3C). Finally, the lowest contrast tested in our main dataset was 0.04, so it was unclear whether there could be facilitation to 0 contrast as well. We performed additional experiments in Pvalb-IRES-Cre;Ai32 mice that showed similar adaptation and photostimulation effects to our main dataset (Figure S3D) and found that cortical silencing during adaptation produced significant facilitation at 0 contrast (Figure S3E; $\overline{X}$ = 0.07; 95% CI [0.04, 0.11]; p = 1.5 × 10^{-3}). Identical photostimulation when not paired with adaptation did not produce facilitation at 0 contrast (Figure S3F; $\overline{X}$ = 0.01; 95% CI [−0.04, 0.02]; p = 0.66). Overall, these additional data indicate that the changes induced by photostimulation, particularly the facilitation at low contrasts, reflect genuine adaptation effects unveiled by cortical silencing.

Contrast Adaptation in dLGN

The dLGN provides major feedforward projections to V1 and shows weak adaptation in cats and primates [4, 5]. Therefore, we examined contrast adaptation in the mouse dLGN as a potential source of adaptation that could be passed on to V1. Characterizing adaptation prior to the thalamo-cortical synapse was also important for parsing inherited adaptation from synaptic depression. We used an identical adaptation protocol to mimic the adaptation that would have been inherited from dLGN in the V1 dataset. Data from wild-type (n = 26) and transgenic mice (n = 8) were pooled for conditions without photostimulation. Comparing both the sample dLGN neurons (Figures 2B, 2D, 2F, and S4A) and the average normalized population curves (Figure 3C) to the photostimulated V1 data, there were several obvious similarities. At high contrasts, the attenuation normally observed in V1 following contrast adaptation was more modest for dLGN. Interestingly, dLGN responses to low contrasts were facilitated following adaptation, which was not observed in V1 following regular adaptation but was often induced when photostimulation was paired with adaptation. Like V1, the low-contrast enhancement in dLGN was unlikely to be a rebound effect or after-discharge because it was present for both the first and second grating cycles (Figure S3B) and remained strong when F_1 was used to measure response amplitude (Figure S3C).

We analyzed parameters extracted from sigmoid fits to measure the adaptation effect across the population in dLGN, as we had done for V1. Contrast adaptation significantly increased c_{50} (Figure 3E; $\overline{X}$ = 0.09; 95% CI [0.04, 0.14]; p = 2 × 10^{-3}) and M (Figure 3F; $\overline{X}$ = 0.11; 95% CI [0.08, 0.15]; p = 3.4 × 10^{-6}) and decreased R_{max} (Figure 3D; $\overline{X}$ = −0.08; 95% CI [−0.12, −0.04]; p = 1.4 × 10^{-3}). Next, we calculated the percent change between nonadapted and adapted parameters to directly compare the magnitude of adaptation in dLGN and V1 with or without photostimulation. For regular adaptation (Figure 3G, compare left and middle columns), V1 neurons showed 29% greater decreases in R_{max} (95% CI [22, 36]; p = 3 × 10^{-10}) and 12% greater increases in c_{50} (95% CI [6, 19]; p = 2 × 10^{-3}) than dLGN neurons. This corroborates earlier findings in cats that adaptation in dLGN was weaker than that observed in cortex [4, 21]. Contrast adaptation elevated M by 12% more in dLGN than in V1 (95% CI [8, 16]; p = 1 × 10^{-7}), which is a novel effect not reported in other studies. The magnitude of adaptation in V1 following cortical silencing was more similar to that observed in dLGN (Figure 3G, compare middle and right columns), with no evidence of a difference for changes in c_{50} ($\overline{X}$ = 6; 95% CI [−1, 12]; p = 0.1) or M ($\overline{X}$ = −1; 95% CI [−7, 4]; p = 0.7) but a 16% larger decrease in R_{max} (95% CI [9, 22]; p = 1.5 × 10^{-4}).

Optogenetic modulation of V1 has altered cortico-thalamic feedback in some studies [22], but not others [15, 16]. To determine whether silencing V1 neurons during the adaptation period could affect adaptation in dLGN (and subsequently the feedforward signal sent to V1), we interleaved photostimulation of V1 with our adaptation stimuli while recording in dLGN. V1 photostimulation did not change dLGN activity significantly (Figures S4B–S4D). Subsequently, V1 photostimulation also had no consistent effects on the adaptation exhibited by dLGN neurons (Figures S4E–S4G). Taken together, these results
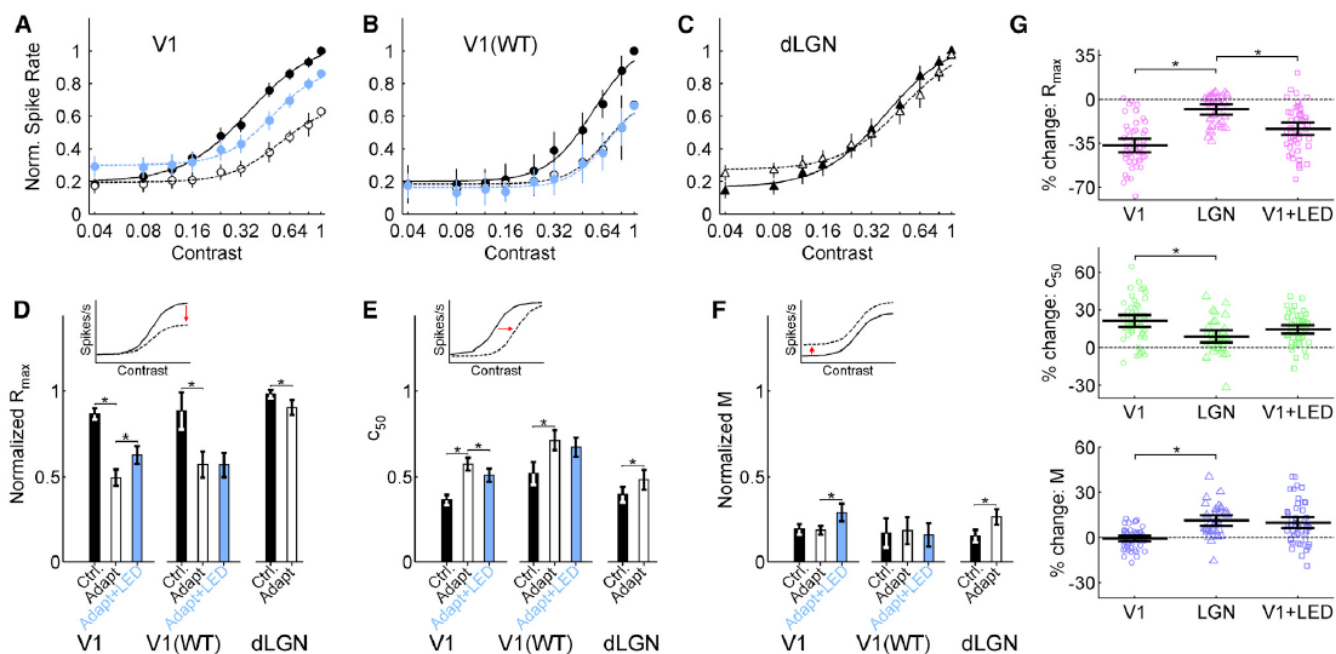
Figure 3. Population Data for Adaptation and Optogenetic Effects on V1 and dLGN

(A–C) Population average of normalized contrast response functions for V1 neurons in transgenic mice (A), V1 neurons in wild-type mice (B), and dLGN neurons (C). Symbols are as in Figure 2.

(D) Bar graph of normalized R_{max} values across three conditions: control (Ctrl; black); adapt (white); and adapt+LED (blue). Data from V1 neurons recorded in transgenic mice, V1 neurons recorded in wild-type mice, and dLGN neurons are shown on the left, middle, and right, respectively. The inset top left depicts the hypothetical alteration of a contrast response function when only the R_{max} parameter is changed.

(E and F) c_{50} and normalized M data with the same format as (D), respectively.

(G) The percent change from control for R_{max} (magenta), c_{50} (green), and M (blue) plotted to compare the magnitude of adaptation between dLGN (middle columns) with regular V1 adaptation (left columns) and V1 adaptation paired with photostimulation (right columns).

Error bars in (A)–(G) indicate 95% confidence intervals, and brackets with asterisks indicate statistically significant comparisons. See also Figures S1–S4.

indicate contrast adaptation is present in dLGN, likely has a pre-cortical origin rather than being induced by feedback, and has features strikingly similar to the adaptation observed in V1 with cortical silencing.

Divisive Scaling Describes the Difference between dLGN and V1

Adaptation normally caused low-contrast facilitation in dLGN, but not V1, which suggests V1 cancels out this facilitation with either divisive scaling or a subtractive shift of the inherited dLGN signal. Therefore, we first created simple divisive and subtractive models that started with the equalized dLGN input (Figure 4A, green triangles) and attempted to fit the average normalized V1 data (see Supplemental Experimental Procedures). For regular V1 adaptation (empty circles), the divisive model fit much better ($r^2 = 0.99$; Figure 4B, magenta line) than the subtractive model ($r^2 = 0.38$; Figure 4C, gold line). Adapted V1 responses following photostimulation (Figure 4D, blue dots) matched the inherited dLGN input fairly closely, so the models were barely distinguishable for these data (divisive model: $r^2 = 0.99$, magenta line; subtractive model: $r^2 = 0.97$, line not shown). Next, for individual V1 neurons, we compared how well divisively scaled or subtractively shifted versions of the "adapt+LED" curve could fit the regular adapted data. Across the population, divisive scaling produced better fits in 70% of cells, and this difference was significant (Figure 4E; $p = 5 \times 10^{-4}$).

Multiple Sources of Adaptation

Our findings refine and extend multi-source models of adaptation. In previous studies, adaptation that could potentially be inherited from antecedent areas has either been measured directly [8, 23, 24] or estimated based on known differences between stages in spatial scale [7] or spatiotemporal tuning [25]. By measuring the thalamic input, and also using optogenetics to essentially "pause" adaptation in V1, we definitively parsed inherited and locally generated adaptation from other processes. The small difference between the adapted dLGN input and the photostimulated V1 curve in Figure 4D may reflect a gain change at the thalamo-cortical synapse induced by synaptic depression [9] or perhaps the divisive effect of distal projections that were outside the reach of our photostimulation [26]. However small their contributions, further work should be done to identify these additional adaptation sources.

The largest contributor to V1 adaptation was the activity-dependent divisive scaling that was minimized by cortical silencing. Several potential cellular or circuit mechanisms could implement this divisive gain control in V1 [27]. Intracellular recordings in cats and ferrets indicate that contrast adaptation produces a slow after-hyperpolarization mediated by a Na^+-dependent K^+ current [4, 28, 29]. If this intrinsic adaptive mechanism exists in mouse V1, optogenetic silencing likely retarded its activation by decreasing Na^+ influx through voltage-gated channels during the adaptation period. At the circuit level,
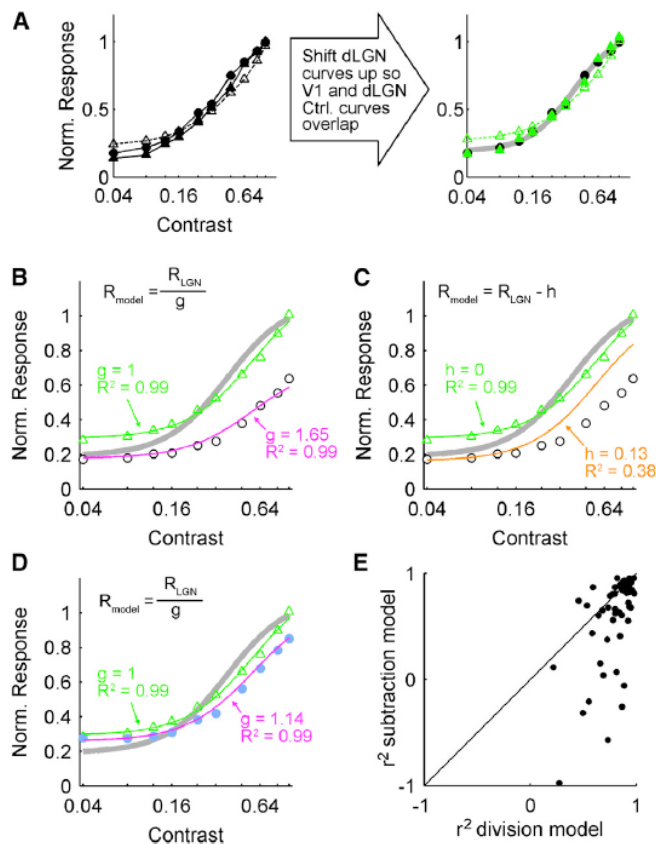
Figure 4. Modeling Divisive Scaling of the dLGN Signal Can Reproduce V1 Responses

(A) To compare average normalized data, we first equalized dLGN and V1 control curves by shifting both the nonadapted (filled triangles) and adapted (empty triangles) dLGN curves slightly upward so the nonadapted dLGN curve matched the nonadapted V1 curve (filled circles). Equalized dLGN data are colored green. The thick gray line indicates the best fit to pooled dLGN and V1 data and is used to summarize nonadapted responses in (B)–(D).

(B) Divisive scaling of adapted dLGN data fit to regular adaptation in V1 (empty dots). The formula for divisive scaling is shown inset top left. The green and magenta curves show the unscaled ($g = 1$) and scaled ($g = 1.65$) fits, respectively.

(C) Subtractive shift of adapted dLGN data fit to regular adaptation in V1. The formula for subtractive shift is shown inset top left. The green and gold curves show the unshifted ($h = 0$) and shifted ($h = 0.13$) fits, respectively.

(D) Divisive scaling to fit adapt+LED V1 data (blue dots) following the same format as (B). The r^2 values to assess the quality of each curve fit are noted in (B)–(D).

(E) Data from individual V1 neurons comparing goodness of fit (r^2) for divisively scaled (abscissa) or subtractively shifted (ordinate) versions of the "adapt+LED" curve fitted to regular adapt data. Solid line denotes equality.

optogenetically stimulating Pvalb+ interneurons induces divisive scaling of V1 orientation tuning and contrast response functions [30, 31], as does activation of layer 6 excitatory neurons [22], but it remains to be determined whether these scaling effects carry forward in time beyond the photostimulation period to contribute to adaptation. Two-photon calcium imaging in cat V1 also suggests a potential role for Pvalb+ cells in adaptation [32]. Synaptic depression of local recurrent excitatory connections is another potential mechanism of V1 adaptation that would also be reduced by cortical silencing [33, 34].

Low-contrast facilitation following contrast adaptation has not been reported for dLGN neurons of cats and primates [4, 5]. Thus, the low-contrast facilitation that served here as a distinctive signature of dLGN adaptation may be particular to mice but more likely resulted from the shorter but higher contrast adapting stimuli we used. The relatively brief yet robust firing produced is consistent with in vitro conditions associated with synaptic enhancement [35]. Synaptic enhancement at one stage combined with depression to higher frequency firing at another could generate the observed pattern of dLGN adaptation; however, further work is required to test this possibility. Furthermore, the disappearance of low-contrast facilitation in V1 illustrates a counterintuitive concept not explicitly considered previously: one stage of processing can undo adaptive changes produced by previous stages. What could be the advantage of this? Under the premise that adaptation serves a useful role in information processing [6], this low-contrast facilitation in dLGN may be beneficial in preserving effective thalamo-cortical drive for low to medium contrasts even when V1 is under the influence of strong divisive scaling. If facilitation is indeed more pronounced with brief adaptation periods, this preservation of low-contrast information is consistent with the psychophysical observation that shorter adaptation times yield smaller elevations in the contrast detection threshold [1].

Conclusions

Adaptation is ubiquitous, occurring in multiple sensory modalities and brain regions along the sensory pathways [36]. Thus, to understand the neural basis for perception, it is not only necessary to understand how receptive fields change from one stage of processing to the next but also how adaptation cascades along these stages to alter neural response properties depending on the temporal context. This work, plus recent findings in somatosensory cortex [37], demonstrates the utility of optogenetic tools for interrogating these dynamic context-dependent signals.

REFERENCES

1. Blakemore, C., and Campbell, F.W. (1969). Adaptation to spatial stimuli. J. Physiol. *200*, 11P–13P.

2. Hammett, S.T., Snowden, R.J., and Smith, A.T. (1994). Perceived contrast as a function of adaptation duration. Vision Res. *34*, 31–40.

3. Demb, J.B. (2008). Functional circuitry of visual adaptation in the retina. J. Physiol. *586*, 4377–4384.

4. Sanchez-Vives, M.V., Nowak, L.G., and McCormick, D.A. (2000). Membrane mechanisms underlying contrast adaptation in cat area 17 in vivo. J. Neurosci. *20*, 4267–4285.

5. Solomon, S.G., Peirce, J.W., Dhruv, N.T., and Lennie, P. (2004). Profound contrast adaptation early in the visual pathway. Neuron *42*, 155–162.

6. Kohn, A. (2007). Visual adaptation: physiology, mechanisms, and functional benefits. J. Neurophysiol. *97*, 3155–3164.

7. Kohn, A., and Movshon, J.A. (2003). Neuronal adaptation to visual motion in area MT of the macaque. Neuron *39*, 681–691.

8. Dhruv, N.T., and Carandini, M. (2014). Cascaded effects of spatial adaptation in the early visual system. Neuron *81*, 529–535.

9. Chung, S., Li, X., and Nelson, S.B. (2002). Short-term depression at thalamocortical synapses contributes to rapid adaptation of cortical sensory responses in vivo. Neuron *34*, 437–446.

10. Stroud, A.C., Ledue, E.E., and Crowder, N.A. (2012). Orientation specificity of contrast adaptation in mouse primary visual cortex. J. Neurophysiol. *108*, 1381–1391.

11. LeDue, E.E., King, J.L., Stover, K.R., and Crowder, N.A. (2013). Spatiotemporal specificity of contrast adaptation in mouse primary visual cortex. Front. Neural Circuits *7*, 154.

12. Vautin, R.G., and Berkley, M.A. (1977). Responses of single cells in cat visual cortex to prolonged stimulus movement: neural correlates of visual aftereffects. J. Neurophysiol. *40*, 1051–1065.

13. Carandini, M. (2000). Visual cortex: fatigue and adaptation. Curr. Biol. *10*, R605–R607.

14. Zhao, S., Ting, J.T., Atallah, H.E., Qiu, L., Tan, J., Gloss, B., Augustine, G.J., Deisseroth, K., Luo, M., Graybiel, A.M., and Feng, G. (2011). Cell type–specific channelrhodopsin-2 transgenic mice for optogenetic dissection of neural circuitry function. Nat. Methods *8*, 745–752.

15. Li, Y.T., Ibrahim, L.A., Liu, B.H., Zhang, L.I., and Tao, H.W. (2013). Linear transformation of thalamocortical input by intracortical excitation. Nat. Neurosci. *16*, 1324–1330.

16. Lien, A.D., and Scanziani, M. (2013). Tuned thalamic excitation is amplified by visual cortical circuits. Nat. Neurosci. *16*, 1315–1323.

17. Pfeffer, C.K., Xue, M., He, M., Huang, Z.J., and Scanziani, M. (2013). Inhibition of inhibition in visual cortex: the logic of connections between molecularly distinct interneurons. Nat. Neurosci. *16*, 1068–1076.

18. Ibbotson, M.R. (2005). Physiological mechanisms of adaptation in the visual system. In Fitting the Mind to the World: Adaptation and Aftereffects in High-Level Vision, C.W.G. Clifford, and G. Rhodes, eds. (Oxford University Press), pp. 17–45.

19. Vidyasagar, T.R. (1990). Pattern adaptation in cat visual cortex is a cooperative phenomenon. Neuroscience *36*, 175–179.

20. McLelland, D., Baker, P.M., Ahmed, B., and Bair, W. (2010). Neuronal responses during and after the presentation of static visual stimuli in macaque primary visual cortex. J. Neurosci. *30*, 12619–12631.

21. Ohzawa, I., Sclar, G., and Freeman, R.D. (1985). Contrast gain control in the cat's visual system. J. Neurophysiol. *54*, 651–667.

22. Olsen, S.R., Bortone, D.S., Adesnik, H., and Scanziani, M. (2012). Gain control by layer six in cortical circuits of vision. Nature *483*, 47–52.

23. Nelson, S.B. (1991). Temporal interactions in the cat visual system. I. Orientation-selective suppression in the visual cortex. J. Neurosci. *11*, 344–356.

24. Nelson, S.B. (1991). Temporal interactions in the cat visual system. II. Suppressive and facilitatory effects in the lateral geniculate nucleus. J. Neurosci. *11*, 357–368.

25. Dhruv, N.T., Tailby, C., Sokol, S.H., and Lennie, P. (2011). Multiple adaptable mechanisms early in the primate visual pathway. J. Neurosci. *31*, 15016–15025.

26. Sato, T.K., Häusser, M., and Carandini, M. (2014). Distal connectivity causes summation and division across mouse visual cortex. Nat. Neurosci. *17*, 30–32.

27. Carandini, M., and Heeger, D.J. (2011). Normalization as a canonical neural computation. Nat. Rev. Neurosci. *13*, 51–62.

28. Sanchez-Vives, M.V., Nowak, L.G., and McCormick, D.A. (2000). Cellular mechanisms of long-lasting adaptation in visual cortical neurons in vitro. J. Neurosci. *20*, 4286–4299.

29. Carandini, M., and Ferster, D. (1997). A tonic hyperpolarization underlying contrast adaptation in cat visual cortex. Science *276*, 949–952.

30. Atallah, B.V., Bruns, W., Carandini, M., and Scanziani, M. (2012). Parvalbumin-expressing interneurons linearly transform cortical responses to visual stimuli. Neuron *73*, 159–170.

31. Wilson, N.R., Runyan, C.A., Wang, F.L., and Sur, M. (2012). Division and subtraction by distinct cortical inhibitory networks in vivo. Nature *488*, 343–348.

32. Keller, A.J., and Martin, K.A. (2015). Local circuits for contrast normalization and adaptation investigated with two-photon imaging in cat primary visual cortex. J. Neurosci. *35*, 10078–10087.

33. Varela, J.A., Sen, K., Gibson, J., Fost, J., Abbott, L.F., and Nelson, S.B. (1997). A quantitative description of short-term plasticity at excitatory synapses in layer 2/3 of rat primary visual cortex. J. Neurosci. *17*, 7926–7940.

34. Galarreta, M., and Hestrin, S. (1998). Frequency-dependent synaptic depression and the balance of excitation and inhibition in the neocortex. Nat. Neurosci. *1*, 587–594.

35. Abbott, L.F., and Regehr, W.G. (2004). Synaptic computation. Nature *431*, 796–803.

36. Wark, B., Lundstrom, B.N., and Fairhall, A. (2007). Sensory adaptation. Curr. Opin. Neurobiol. *17*, 423–429.

37. Musall, S., von der Behrens, W., Mayrhofer, J.M., Weber, B., Helmchen, F., and Haiss, F. (2014). Tactile frequency discrimination is enhanced by circumventing neocortical adaptation. Nat. Neurosci. *17*, 1567–1573.

Thank you for your order!

Dear Jillian King,

Thank you for placing your order through Copyright Clearance Center's RightsLink® service.

Order Summary

Licensee:	Dalhousie University
Order Date:	Nov 30, 2019
Order Number:	4718781462129
Publication:	Neuron
Title:	Neuronal Selectivity and Local Map Structure in Visual Cortex
Type of Use:	reuse in a thesis/dissertation
Order Total:	0.00 CAD

View or print complete details of your order and the publisher's terms and conditions.

Sincerely,

Copyright Clearance Center

August 3, 2019

I am preparing my Doctoral thesis for submission to the Faculty of Graduate Studies at Dalhousie University, Halifax, Nova Scotia, Canada. I am seeking your permission to include Figure 1A from the manuscript version of the following paper(s) as a figure in the thesis:

Divisive Inhibition Prevails During Simultaneous Optogenetic Activation of All Interneuron Subtypes in Mouse Primary Visual Cortex. Ingram TGJ, King JL, Crowder NA. Frontiers in Neural Circuits. 13:40, May 2019.

Canadian graduate theses are reproduced by the Library and Archives of Canada (formerly National Library of Canada) through a non-exclusive, world-wide license to reproduce, loan, distribute, or sell theses. I am also seeking your permission for the material described above to be reproduced and distributed by the LAC(NLC). Further details about the LAC(NLC) thesis program are available on the LAC(NLC) website (www.nlc-bnc.ca).

Full publication details and a copy of this permission letter will be included in the thesis.

Yours sincerely,

Jillian King

Permission is granted for:

a) the inclusion of the material described above in your thesis.

b) for the material described above to be included in the copy of your thesis that is sent to the Library and Archives of Canada (formerly National Library of Canada) for reproduction and distribution.

Name: __Tony Ingram_____ Title: __Graduate Student_____

Signature: ██████████████ Date: __Aug 16, 2019_____

April 29, 2019

I am preparing my Doctoral thesis for submission to the Faculty of Graduate Studies at Dalhousie University, Halifax, Nova Scotia, Canada. I am seeking your permission to include a manuscript version of the following paper(s) as a chapter in the thesis:

Adaptive Processes in Thalamus and Cortex Revealed by Silencing of Primary Visual Cortex during Contrast Adaptation, by Jillian L King, Matthew P Lowe, Kurt R Stover, Aimee A Wong and Nathan A Crowder, Current Biology, 26, 1295-3000, May 23, 2016.

Canadian graduate theses are reproduced by the Library and Archives of Canada (formerly National Library of Canada) through a non-exclusive, world-wide license to reproduce, loan, distribute, or sell theses. I am also seeking your permission for the material described above to be reproduced and distributed by the LAC(NLC). Further details about the LAC(NLC) thesis program are available on the LAC(NLC) website (www.nlc-bnc.ca).

Full publication details and a copy of this permission letter will be included in the thesis.

Yours sincerely,

Jillian King

Permission is granted for:

a) the inclusion of the material described above in your thesis.

b) for the material described above to be included in the copy of your thesis that is sent to the Library and Archives of Canada (formerly National Library of Canada) for reproduction and distribution.

Name:	Matthew Lowe	Title:	Mr.
Signature:	███████████	Date:	2019/04/29

April 29, 2019

I am preparing my Doctoral thesis for submission to the Faculty of Graduate Studies at Dalhousie University, Halifax, Nova Scotia, Canada. I am seeking your permission to include a manuscript version of the following paper(s) as a chapter in the thesis:

Adaptive Processes in Thalamus and Cortex Revealed by Silencing of Primary Visual Cortex during Contrast Adaptation, by Jillian L King, Matthew P Lowe, Kurt R Stover, Aimee A Wong and Nathan A Crowder, Current Biology, 26, 1295-3000, May 23, 2016.

Canadian graduate theses are reproduced by the Library and Archives of Canada (formerly National Library of Canada) through a non-exclusive, world-wide license to reproduce, loan, distribute, or sell theses. I am also seeking your permission for the material described above to be reproduced and distributed by the LAC(NLC). Further details about the LAC(NLC) thesis program are available on the LAC(NLC) website (www.nlc-bnc.ca).

Full publication details and a copy of this permission letter will be included in the thesis.

Yours sincerely,

Jillian King

Permission is granted for:

a) the inclusion of the material described above in your thesis.

b) for the material described above to be included in the copy of your thesis that is sent to the Library and Archives of Canada (formerly National Library of Canada) for reproduction and distribution.

Name: _Kurt Stover_____ Title: _____

Signature: ██████████████ Date: _April 29, 2019_

August 3, 2019

I am preparing my Doctoral thesis for submission to the Faculty of Graduate Studies at Dalhousie University, Halifax, Nova Scotia, Canada. I am seeking your permission to include Figure 1A from the manuscript version of the following paper(s) as a figure in the thesis:

Divisive Inhibition Prevails During Simultaneous Optogenetic Activation of All Interneuron Subtypes in Mouse Primary Visual Cortex. Ingram TGJ, King JL, Crowder NA. Frontiers in Neural Circuits. 13:40, May 2019.

Canadian graduate theses are reproduced by the Library and Archives of Canada (formerly National Library of Canada) through a non-exclusive, world-wide license to reproduce, loan, distribute, or sell theses. I am also seeking your permission for the material described above to be reproduced and distributed by the LAC(NLC). Further details about the LAC(NLC) thesis program are available on the LAC(NLC) website (www.nlc-bnc.ca).

Full publication details and a copy of this permission letter will be included in the thesis.
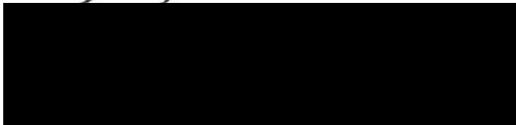
Yours sincerely,

Jillian King

Permission is granted for:

a) the inclusion of the material described above in your thesis.

b) for the material described above to be included in the copy of your thesis that is sent to the Library and Archives of Canada (formerly National Library of Canada) for reproduction and distribution.

Name: Nathan Crowder   Title: Associate Professor

Signature: ████████████████   Date: Aug. 12, 2019

April 29, 2019

I am preparing my Doctoral thesis for submission to the Faculty of Graduate Studies at Dalhousie University, Halifax, Nova Scotia, Canada. I am seeking your permission to include a manuscript version of the following paper(s) as a chapter in the thesis:

Adaptive Processes in Thalamus and Cortex Revealed by Silencing of Primary Visual Cortex during Contrast Adaptation, by Jillian L King, Matthew P Lowe, Kurt R Stover, Aimee A Wong and Nathan A Crowder, Current Biology, 26, 1295-3000, May 23, 2016.

Canadian graduate theses are reproduced by the Library and Archives of Canada (formerly National Library of Canada) through a non-exclusive, world-wide license to reproduce, loan, distribute, or sell theses. I am also seeking your permission for the material described above to be reproduced and distributed by the LAC(NLC). Further details about the LAC(NLC) thesis program are available on the LAC(NLC) website (www.nlc-bnc.ca).

Full publication details and a copy of this permission letter will be included in the thesis.
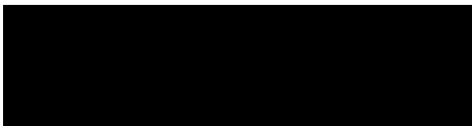
Yours sincerely,

Jillian King

_____

Permission is granted for:

a) the inclusion of the material described above in your thesis.

b) for the material described above to be included in the copy of your thesis that is sent to the Library and Archives of Canada (formerly National Library of Canada) for reproduction and distribution.

Name: ___Aimee A Wong_____   Title: __Dr._____

Signature: ███████████████████   Date: __April 29th, 2019_____

April 29, 2019

I am preparing my Doctoral thesis for submission to the Faculty of Graduate Studies at Dalhousie University, Halifax, Nova Scotia, Canada. I am seeking your permission to include a manuscript version of the following paper(s) as a chapter in the thesis:

Adaptive Processes in Thalamus and Cortex Revealed by Silencing of Primary Visual Cortex during Contrast Adaptation, by Jillian L King, Matthew P Lowe, Kurt R Stover, Aimee A Wong and Nathan A Crowder, Current Biology, 26, 1295-3000, May 23, 2016.

Canadian graduate theses are reproduced by the Library and Archives of Canada (formerly National Library of Canada) through a non-exclusive, world-wide license to reproduce, loan, distribute, or sell theses. I am also seeking your permission for the material described above to be reproduced and distributed by the LAC(NLC). Further details about the LAC(NLC) thesis program are available on the LAC(NLC) website (www.nlc-bnc.ca).

Full publication details and a copy of this permission letter will be included in the thesis.

Yours sincerely,

Jillian King

_____

Permission is granted for:

a) the inclusion of the material described above in your thesis.

b) for the material described above to be included in the copy of your thesis that is sent to the Library and Archives of Canada (formerly National Library of Canada) for reproduction and distribution.

Name: _Nathan Crowder_____ Title: Associate Professor_____

Signature: ███████████████ Date: April 29, 2019_____